Spectroscopy of the Temperature and Current Driven Metal-Insulator Transition in Ca_2RuO_4

Minghao Cheng

Submitted in partial fulfillment of the
requirements for the degree
of Doctor of Philosophy
in the Graduate School of Arts and Sciences

COLUMBIA UNIVERSITY

2020

ABSTRACT

Spectroscopy of the Temperature and Current Driven Metal-Insulator Transition in Ca_2RuO_4

Minghao Cheng

This thesis presents the study for the temperature-driven and current-driven metal-insulator phase transition (MIT) in Ca_2RuO_4 via home-built variable temperature Scanning Tunneling Microscope. Atomically resolved topography images along with temperature dependence of resistivity are taken verifying the quality of the single crystals used in this experiment. Tunneling spectra are measured under various temperatures accross the $T_{\mathrm{MI}} = 357K$, which clearly shows spectra evolution with temperature and the difference between the room-temperature insulator phase and the high-temprature metal phase. Compared with DMFT calculation, the STS indicates lattice structure plays a vital role in the phase transition. Same measurement is conducted on the crystals under a DC current, thanks to a custom designed sample holder. The evolution of the tunneling spectra with source current demonstrates similarity with the one of temperature-driven MIT. The comparison between the spectra taken at high-temperature metalic state and the high-current metalic state highlights the similarity of these 2 phases, with both showing a DOS transfer from $1eV$ to lower energy, when compared with the ground state. Combined with a variety of other studies via transport, scattering technique and infrared thermal imaging, it is found that the local temperature dominates both temperature-driven and current-driven MIT. It is very likely that the current-driven is caused by the inevitable Joule heating generated by the current, indicating the high-current metallic phase might be the same with high-current metallic phase. Finally, surface roughness and autocorrelation length analysis suggests an inhomogeneous surface topography stemmed from the coexistence of the insulating S* phase and conducting L* phase under current.

Table of Contents

List of Figures

List of Tables

Acknowledgments

I first would like to thank Prof. Abhay Pasupathy for being an exceptional mentor. Thank you for your support, guidence, wisdom, and open-mindedness throughout my Ph.D. I am especially grateful for not being fired after me destroying so many experimental equipment (typically they are fixed in the end, one way or another, by me or someone else) during my research. I still remember when I joined this lab, Abhay told me as an experimentalist all I need to know is Ohm's law and how to distinguish the inlet and outlet of a pump. Now with years' academic traning, though I still don't know who is Ohm and what law he wrote, I can safely say the later issue bothers me no more (in most scenarios).

A huge thanks to my parents, who have taken cared of me with all their love and patience. Through my entire life they have been supporting me, for which I can never be grateful enough. My mom is always kind to me while my dad being more strict, often helps me out when I am in trouble. Without their love I will never have the chance to live such a wonderful life. After I entered middle school, I have spent less time with them than with schools. I really wish I could be with them more in the future.

My journey on physics begins when I was a yound kid trying to impress others with bragging on some scientific terminologies. Yet on this journey I was so lucky to meet many brilliant teachers, mentors and guides. I would like to thank them for not only teaching me the 101s I need to pursue more advanced knowledge, but also encouraging me to keep going on this adventure. Especially I would like to thank my PI in Peking University, Prof. Yuan Li, for guiding me into formal academic research. These days working under your guidance is definitely one of the most enjoyable and productive periods in my life.

I want to thank everyone in the Abhay's group. Dr. Ethan Rosenthal, Dr. Chris Gutiérrez (now Prof. Gutiérrez), Dr. Ali Dadgar, Dr. Carlos Arguello, Dr. Erick Andrade, Dr. Ayelet Notis, Dr. Sky Cheung, Dr. Dennis Wang, Dr. Alex Kerelsky, Dc. Lior Embon,

Dr. Leo McGilly, Andrew Wieteska and Simon Turkel. Thank you all for creating a lovely and productive lab to work in.

I would like to also thank my friends in Columbia. I am trully sorry that now the first scenes come to my mind are the days when we skied, played cards or watched sports together. But I am pretty confident that there are plenty of times that you pulled me out of troubles., for which I feel really lucky and grateful. Though I can still see a few of you, many of you have left New York or the States in the past few years. Sincerely I wish you all the good luck and am looking forward to meeting you again somewhere in the future.

As what this thesis is mainly about, phase transition is exactly what I am experiencing now. Propabaly these days when I typed for this thesis will be the last few days I spend in campus (virtually due to the COVID-19 pandemic..). After about 22 years' school life, now it is time for me to enter the next phase in my life. Though what lies in the future always remains as a big question mark, I wish the days I spent here could enable me to start the new adventure with little fear. I wish one day when I had to revisit these memories, I could look back with no regrets. I wish as this chapter closes, it opens the door to many new worlds and success.

Chapter 1

Introduction

Condensed matter physics studies the properties of a wide variety of materials, often driven by their novel properties hence huge potential applications. For example, more than 30 years ago, a series of high-Tc superconductors [17] were found among cuprates compunds. They feature superconductivity well beyond the BCS theoretical temperature limit (30K). More interestingly, these materials exhibit a few exotic properties that were never observed before. For instance, instead of traditional s-wave symmetry, the superconducting gap in these compunds share a d-wave symmetry [18, 19, 20]. Furthermore, at temperature above the Tc, a phase featuring a partial energy gap which now is refered as pseudogap, is also found [21]. Although many of these novel features still remains unclear to us, in years of research it is gradually realized that traditional method of studying electron as single independent particles would not work in these systems, where electrons are stronly correlated. In order to fully understand high-Tc superconductivity, it is crucial to comprehensively study the strongly-correlated systems.

The stronly-correlated systems play a significant role in modern condensed matter physics. It leads to many intriguing phenomena and competing orders, including Mott insulators [22], p-wave superconductivity [23, 24, 25], and colossal magenetoresistance (CMR) [26, 27], etc. Materials featuring strongly-correlated electrons typically partially filled d or f shells. In these spatially localized orbitals, electrons are strongly replused with each other through Columbob interaction, which is comparable or even stronger than their kinetic energies. For instance, in transition metal oxides (TMO), most materials belong to the 3d

group, which shows strong electron-electron correlation [28]. When it comes to 4d group, the correlation tends to get weaker due to the fact the 4d orbitals are more spatially extended. Thougth the electron-electron interaction is weaker, other interactions like crystal fiedl splitting are comparable with electron kinetic energy [29], therefore causing a complicated competition among different energies. This leads to its exotic properties and opens the door to characterize these materials with external probe like magnetic field [30] or strain [12].

These constant competitions among different energies greatly enriches the phase diagram of 4d group, particularly for ruthenates which exihibit a variety of interesting phenomena [2, 31, 10]. Ruthenates belong to Ruddelson-Popper series, which was discovered by Ruddelson and Popper [32] and has the general formula of $A_{n+1}B_nX_{3n+1}$, where A (Ca, Sr...) and B (Ti, Ru, Mn...)are the cations, X is an anion (e.g. oxygen) and n is number of layers of BX layers with bridging X. A diagram of Ruddlesden-Popper structure is shown in Fig 1.1

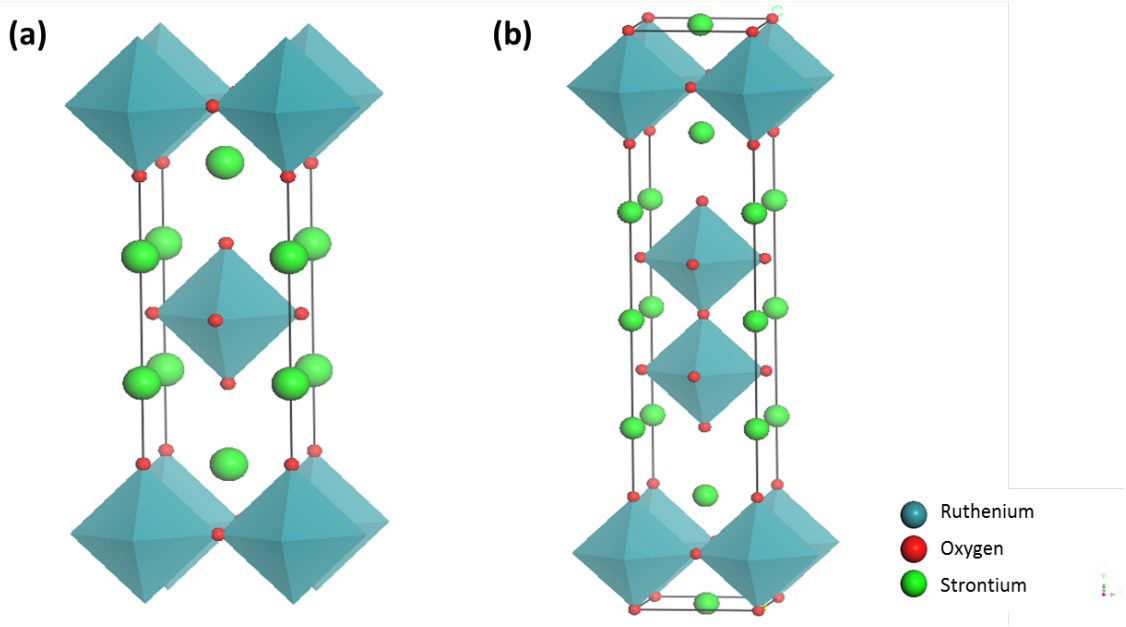

Figure 1.1: The unit cell of Ruddlesden-Popper phase [1] (a)Sr2RuO4 (n = 1) and (b)Sr3Ru2O7 (n = 2)

One of the most common features of these materials is a pronounced lattice distortion.

Due to a smaller ion size , Ca(1.0Å) compounds have a more significant lattice distortion than Sr(1.18Å) compoounds. This somewhat insignificant difference actually give these compounds exceedingly different properties. Most Sr compounds have a ferromagnetic ground states, except Sr_2RuO_4 which has a superconducting ground states [7]. However, most Ca compounds have an antiferromagnetic ground states, except for single-layer compound $CaRuO_3$, which features a paramagnetic ground state [7].

In this thesis our interest mainly focus on the Calsium compound, especially on Ca_2RuO_4. Ca_2RuO_4 has a rich phase diagram as shown in Fig 1.2, featuring an antiferromagnetic ground state and a paramagnetic Mott insulating state at room temperature. With temperature increasing up to about 357K [33], the mott insulating states is destructed and the material experiences a first-order phase transition into a metal, accompanied by a large symmetry-preserving lattice distortion [34, 35]. What is even more interesting is, when applying a dc current/field along the crystal of Ca_2RuO_4, there is another phase transition from insulator to semimetal [31], which can happen in a very wide range of temperatures. This current driven phase transition also features a structural transition similar with that of temperature driven phase transition. [10]. Furthermore, more phases emerge with the presence of current, possibly due to its non-equilibrium nature. For example, an intermediate phase seem to co-exsit with insulating phase during the transition [10]. Though a new dimagnetic semimetal phase was reported to form at a fairly small current density (about 1-1.5 A/cm^2) and low temperature (about 50K), it is recently reported as false due to experimental setup issue[3].

Such abundance of phases is largely thanks to the ruthenium atoms and the structural change in lattice distortion. The unit cell of Ca_2Ru_O4 is shown in Fig. 3.6. The basic structural componet is the octahedra of RuO_6, which are connected by oxygen and seprated by Ca atoms shifted in the z axis. Instead of an ordinary perovskite structure, due to the ditortion and rotation of the octhedra as shown in Fig. 3.7, Ca_2Ru_O4 has a larger unit cell. We will come back to this unique lattice distortion behavior later as it if of vital importance to the property of Ca_2RuO_4.

The native electron configuration of a ruthenium atom is $[Kr]4d^75s^1$. As in Ca_2RuO_4, 4 eletrons are taken to form ionic bonds, therefore the outermost electrons become $4d^4$.

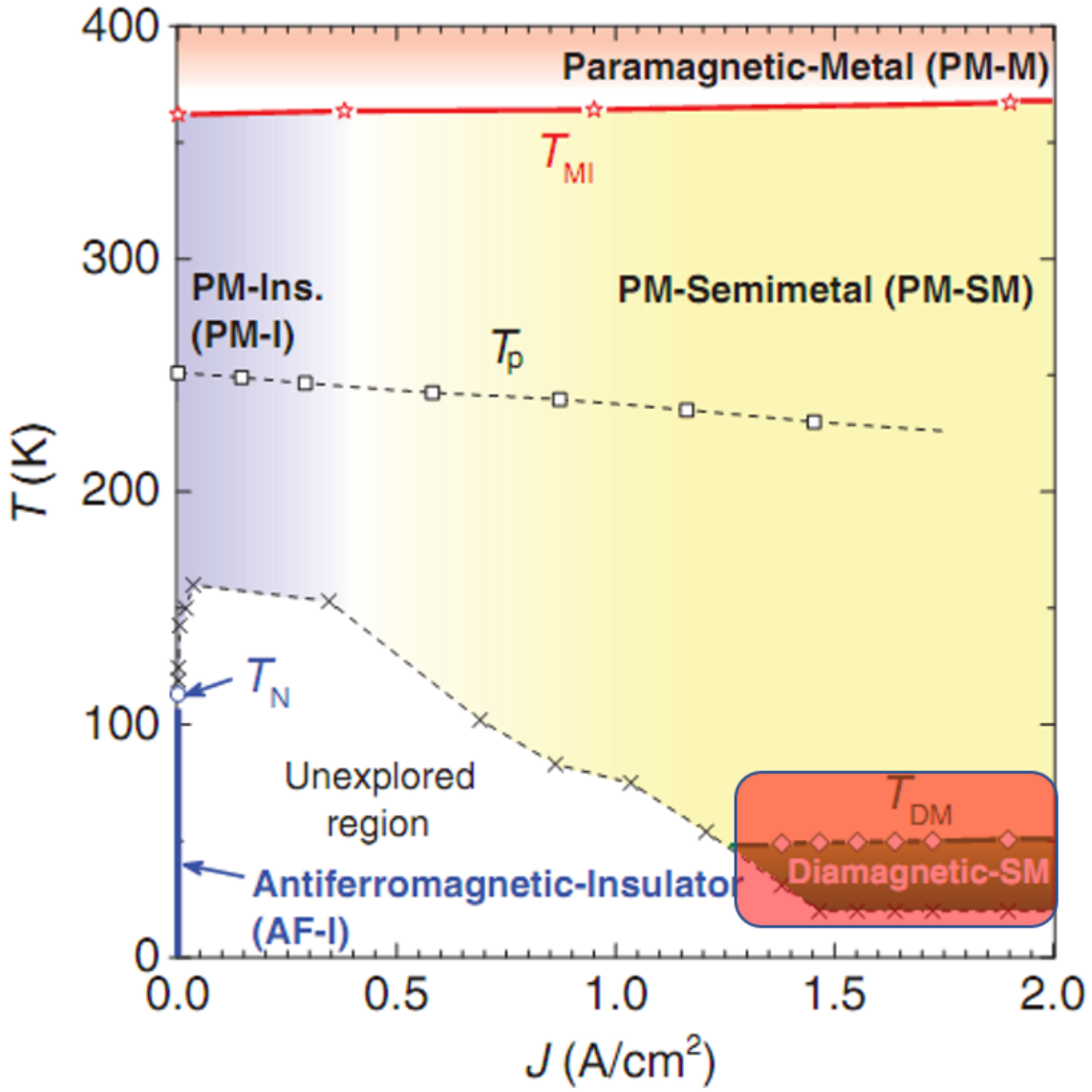

Figure 1.2: Phase diagram of Ca_2RuO_4. Note the diamagnetic semimetal phase (red semi-transparent box) has been found to be false. [2, 3]

These 4 electrons live in the orbitrals of the d shell, of which the original 5-fold degeneracy is lifted by crystal field splitting and Jahn-Teller effect. To see this clearly, the 5 orbitals of d shell are shown in Fig. 1.5. Due to the nature of being more aligned with the principal axes, the d_{z^2} and $d_{x^2-y^2}$ orbitals (t_{2g} orbitals) will have a larger overlap with wave function

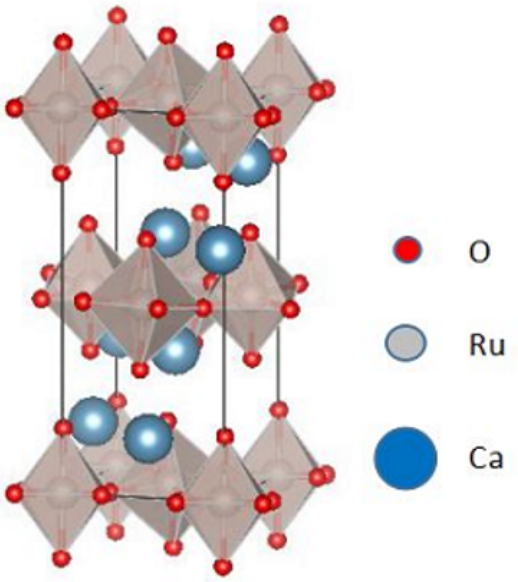

Figure 1.3: Unit Cell of Ca_2RuO_4 [4]

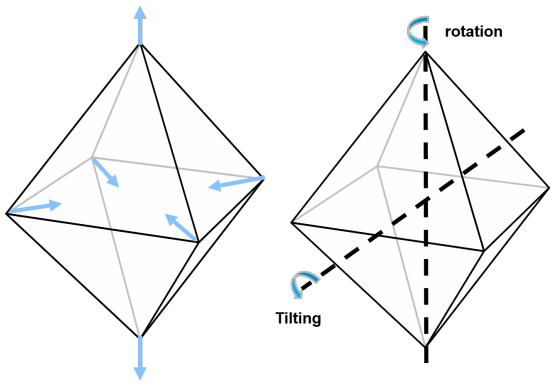

Figure 1.4: Lattice distortion, rotation and tilting of Ca_2RuO_4

with neighbor oxygen electrons hence have higher energy. In contrast, the remaining d_{xy}, d_{xz}, d_{yz} orbitals (e_g orbitals) will have lower energy. This energy split is called crystal field splitting. Furthermore, due to the distortion of the octahedra, the degeneracy of e_g orbitals is also partially lifted. This is due to the nature of the d_{xy} orbital is less extended in the z axis compared with d_{xz} and d_{yz} orbitals. Therefore when the lattice is compressed in z (or c axis in the unit cell coordinates), the energy of the d_{xy} orbital will be lowered and vice versa. This phenomenon is called Jahn-Teller effect. As in this case, Jahn-Teller effect happens with a spontaneous symmetry breaking, thanks to it will lower the total energy of the system. This effect tunes the orbital order and hence the electron configuration, therefore it contributes a lot to exotic properties of Ca_2RuO_4.

The temperature driven phase transition and current driven phase transition have long been puzzling many researchers. Though many great work has been done on this topic, the true transition mechanism still remains unclear. In this thesis we present our characterization of Ca_2RO_4 with STM. In short, we have searched a large area in the phase diagram, which covers the room-temperature Mott insulating states, the high-temperature

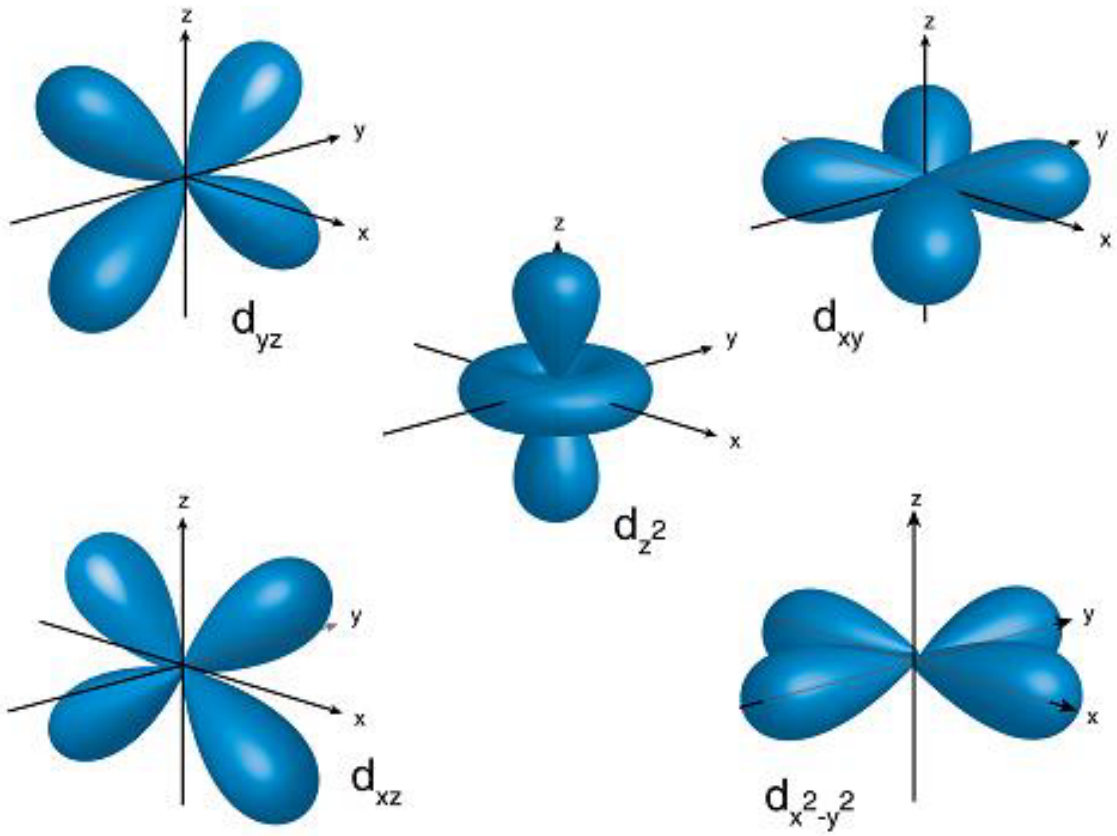

Figure 1.5: 5 orbitals of d shell [5]

metal phase and the current-induced metal phase. We compare the STS taken at different states and (to be continued).

1.1 Outline of Thesis

The work in this thesis is as follows.

Chapter 2 provides an detailed review of scanning tunneling microscopy, including its theoretical background, the setup and maintenance.

Chapter 3 provides an overview of calcium ruthenates.

Chapter 4 describes the experimental setup, including the STM, the temperature control system and the sample preparation.

Chapter 5 presents the results on temperature-driven phase transition.

Chapter 6 presents the results on current-driven phase transition.

Chapter 7 presents comparison between the temperature-driven and current-driven phase transition and the results of surface roughness and auto-correlation analysis.

Chapter 8 compares and summarizes the results from this thesis.

Chapter 2

Background of STM

The main characterization instrument in this thesis is Scanning Tunnling Microscope (STM). Therefore to better understand our work, here we present a brief introduction to STM, including the overview of STM setup and theory, approach of building one and how to fabricate the atomically sharp probe tip.

2.1 Overview of Scanning Tunneling Microscopy

Scanning Tunneling Microscopy (STM) is a technique of micro probe utilizing the quantum property of electrons to image the surface of materials. Since invented in 1981 [36], STM has been widely used in condensed matter physics to both map the surface topography and chacharacterize the electronic property, which unveils many novel physics.

In order to understand how a STM works, one need to first focus on the phenomenon of quantum tunneling, which takes place when two objects with potential differnece are put close enough (typically less than 1 nm). For instance, when 2 metal objects are located very close with each other, seperated by a layer of vaccum, apprently the electrons can move freely within each metal due to their rich density of states (DOS). Classicaly, the electrons are not able to move from one object to another since there is no states in vaccum. However, due to the quantum nature of electrons, their wave functions will overlap if the vaccum barrier is thin enough, which leads to some probability that one electron is able to penetrate the vaccum and move to the other metal hence forming a tunneling current. This phenomenon

is called quantum tunneling and it is highly sensitive to both the distance between the two objects and the density of states.

With the knowledge of quantum tunneling, one is able to understand how a STM works. The basic setup of a STM is a very sharp metal needle (tip) and the surface of the material of interest, all of which is put in the ultra high vaccum (UHV). By carefully setting the distance between the tip and the surface of the material through piezoelectric movers/stacks (the approaching process) and a potential difference (bias), there will be a tunneling current flowing between the tip and the surface. Since this current is very sensitive to the distance from the tip to the surface, through moving the tip on the surface while monitoring and feedbacking on the tunneling current, one is able to measure the surface topography with atomic resolution. Since the current is also sensitive to the density of states in both materials, one could keep the tip fixed and measure the tunneling current while varying the bias voltage between the tip and the surface. This tunneling current – bias voltage curve and its derivative (Scanning Tunneling Spectrum, STS)will shine a light on the electronic structure of the material of interest, therefore it also plays a significant role in STM measurment. The topography and STS form the basic function of a STM and we will discuss them with details in the following parts.

The tunneling current can be modeld by the famous Bardeen formula [37] listed below

$$
\begin{aligned}
&I_{\text{tunnel}} = \frac{4\pi e}{\hbar}\int_0^{eV} \rho_s(E_F - eV + \epsilon)\rho_T(E_F + \epsilon)\|M\|^2 d\epsilon \Rightarrow \\
&I_{\text{tunnel}} \propto \int_0^{eV} \rho_s(E_F - eV + \epsilon)\rho_T(E_F + \epsilon)d\epsilon \quad \text{given } \|M\|^2 \text{ not change in interval of interest} \Rightarrow \\
&\frac{dI_{\text{tunnel}}}{dV} \propto \rho_s(eV) \quad \text{given } \rho_T \text{ is constant}
\end{aligned}
\tag{2.1}
$$

where M is the tunneling matrix, ρ denotes the density of states . In most cases, the tip is made of well studied metal like Tungsten or Platinum/Iridium, of which the density of states remain fairly constant, hence if we treat ρ_T as a constant, the derivate of tunneling current with respect to bias voltage (differential conductance) is proportional to the local density of states (LDOS) of the material. This is the key of the following analysis of STS in this paper.

Fig. 2.1 shows a schematic view of a STM. A sharp metal needle that is electro-chemically etched in advance is installed on a scanning tube, which is small cyclinder formed by 4 quadrants of piezoelectric ceramics. These piezoelectric quadrants will bend towards correponding directions under proper driving voltages (typically 100V), resulting the motion of the tip. With cooperation of all quadrants, fine motion in all 3 axes with subatomic precision can be achieved. Thanks to the scanning tube and coarse piezoelectric stacks/motors, the tip is able to be located at any prefered poistion above the sample surface and the distance between them can be controlled. When they are close enough, by applying a bias voltage, a tunneling current will flow from the sample to the tip, of which the amplitude is about a few pA to nA. Such small current is not easy to detect and can be easily interfered in the following processing, hence it is guided into a pre-amplifer to be enhanced. In constant current mode, a feedback loop is governing and recording the motion of the scanning tube based the tunneling current measured, therefore the topography of the sample surface is obtained. When measuring the STS, the feedback loop is locked and scanning tube is held fixed, then the tunneling current is recorded while the bias voltage varying between the set range. The differential conductance can be obtained by taking numerial derivative on this I-V curve, or by adding a sinuous oscillation to the bias and measurew with the help of a external lock-in amplifier. The following method is often preferred due to better signal to noise ratio.

2.2 Home-made Varible Temperature STM

After 30 years of its invention, STM has already matured to a complicated measurement tool, of which many successful commericial systems can be found in the market. Despite that most commerical STMs could meet ordinary and specific needs of average users, many disadvantages, including being expensive, hard to modify and maintain, still encourage us to build a home-made STM by ourselves.

The main compnents of a STM consist of UHV chambers, pump system (rough pump and ion pump), scanning probe system, data collection and control system, sample transferring system (transfer arm and wobble-stick) and other optional accessaries like cyrostat,

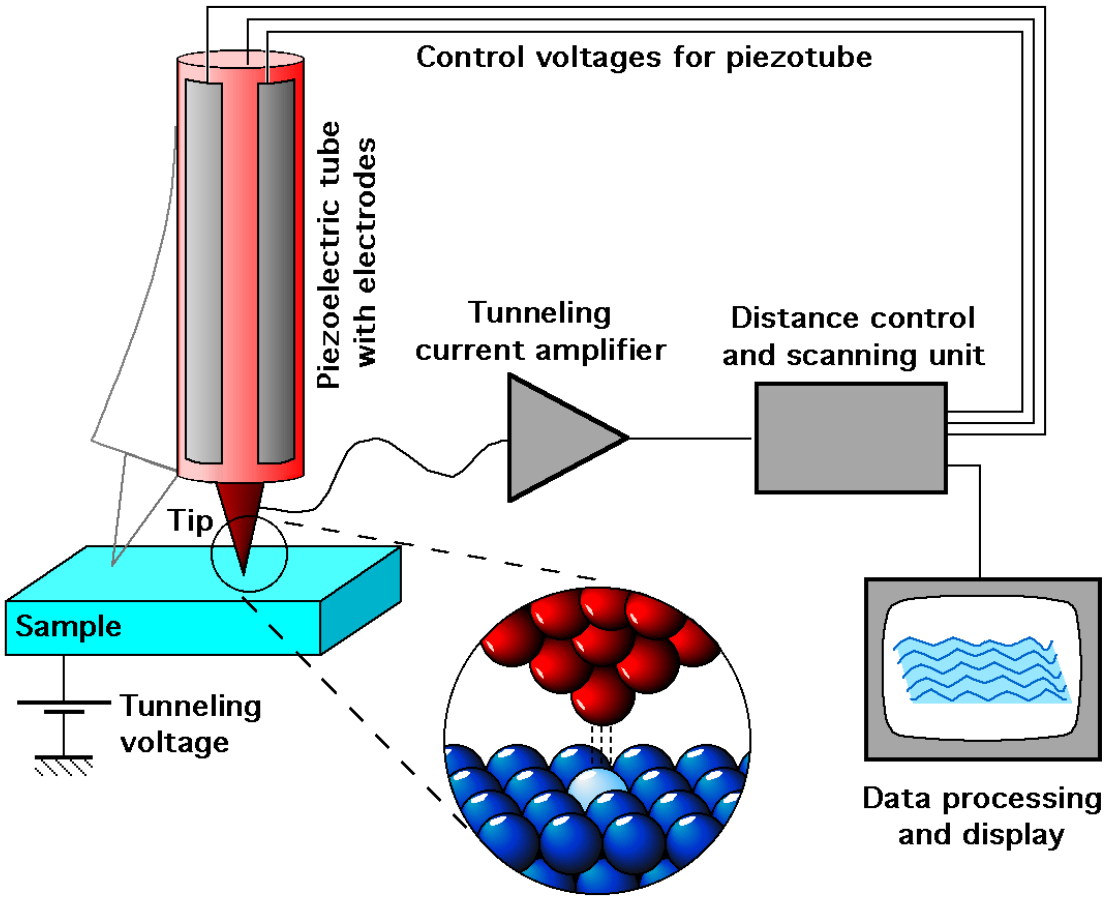

Figure 2.1: Schematic View of a STM

annealers, ion sputter guns and so on. From the introduction above, one could see the core of the STM is the scanning probe system, which controls the position of the tip and distance between the sample surface and the tip. Hence we choose to focus on this core system by ourselves, and leave the design and fabrication of other parts (like the UHV chamber, wobble-sticks, etc.) to external vendors that have rich experience in these areas.

Although there is some minor difference in the design, all scanning probe systems must have a coarse x-y-z motion system and a fine x-y-z motion system. The former one typically is formed by several piezoelectric ceremic stacks, while the later one is a piezoelectric cylinder formed by 4 quardrants (scan tube). The reason why piezoelectric materials are widely used

in STM come from the precision of its motion, which further comes from how it moves under a voltage/electric field. The piezoelectric materials are formed by linked polar molecules, which will distort a little bit in an electric field. This distortion will continue until the material accumulate a sufficient counter field to cancel the external one. Macroscopically these distortions form a contraction or expansion of the crystal hence generating motion. As the amplitude of such distortion is quite small and the nature of such distorsion is quite linear, it can achieve exceedingly fine motion up to sub-atomic precision. With knowledge of piezoelectricity, now we comes back to the fine scan tube. The 4 independent piezoelectric quardrants share a common ground core. When all of the 4 quardrants are under the same voltage, they will have the same amount of distortion. Thus the overall outcome will be a contraction of expansion of the tube, i.e the z motion. If only one of the quardrants are under a certain voltage, it will expand or contract at its own direction, creating a minor bending of the tube. Therefore when properly set voltages on several quardrants (typically 2 next to each other or 2 opposite ones, depending on the geometry of the tube), one can achieve motion in the x-y plane. In conclusion with a tip attched to the fine scan tube, all fine x-y-z motion can be realized. The scan tube used in oiur STM is shown in Fig. 2.2. We bought the tube from commercial vendors as it requires special technique to fabricate. However some custom modification is made on this tube. A small stage with 3 tip slots is attached to the tube, which enables a simultaneous STM and Non-contact Atomic Force Microscope (NC-AFM, tunning fork style) measurement. Such measurement is not relevant in this thesis hence no further introduction is needed.

With fine motion control accomplished, now we focus on the issue of coarse motion control. The purpose of coarse motion control is to position the tip (and the scanning tube) at a desired position above (in our case, below) the surface of the sample. Compared with fine motion control, coarse motion control does not require sub-atomic precision (although with properly designed mover it is feasible and might be helpful. For details check [38]), but requires a far larger motion range (a few mm to cm). Hence the design of this coarse movers is quite different from the fine one. In our STM, we still use piezoelectric materials to build such mover, as the way it moves does not involve any mechanically moving parts (like chain or gear) and hence greatly reduce resonance vibration. The main component to

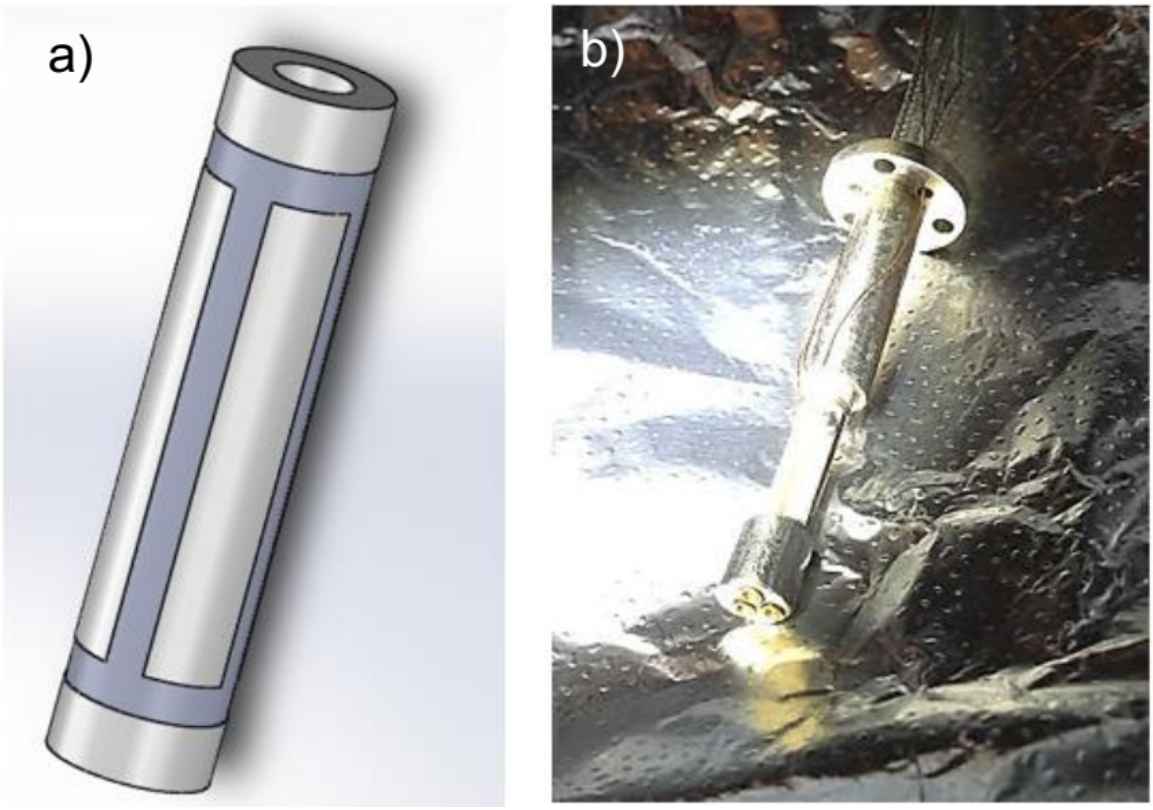

Figure 2.2: Schematic cartoon and a photo of the fine scan tube. (a) the cartoon showing 4 piezoelectric quardrants of the scan tube. (b) A photo of the scan tube in our stm. On the end of the tube a metal stage with 3 tip slots is attached. This allows our STM to peform STM and NC-AFM measurement at the same time.[6]

achieve this coarse motion is the piezoelectric stack, whihc is shown in Fig. 2.3. Fig. 2.3 (a) shows a fully assembled x-y coarse mover, which consists of 2 identical horizontal movers. One of the mover is attached to the scannning stage which has a slot for the sample holder and contacts for bias voltage and other connection if necessary. The other mover holds this mover, with a 90 degree angle. Each mover is able to generate relatively fast and significant motion along its direction. Therefore with 2 indenpent horizontal movers, all position in the x-y plane within the motion range can be reached. The details of the horizontal mover in shown in Fig. 2.3 (b). The 2 big metal parts are the upper and lower half of the mover. When assembled, these 2 parts work like a clamp, tightly holding a metal bar which will be driven by the piezoelectric stacks. The piezoelectric stacks are the white rectangels in the middle of the slots in both parts. Each stack is formed by 2 identical commericial piezoelectric plates. The 2 plates are oriented in the opposite way, where the positive faces are placed back to back and glued by conducting epoxy (EPOTEK H20E) with a metal foil (as the positive electrode), and the ground faces are connected by another metal foil (as the negative electrode) with the top one glued by Torr Seal with a sapphire plate. Same sapphire plates are also put on 2 faces on the metal bar. The purpose of these sapphire plates is to reduce friction. The positive electrode is connected to the wire to feed voltage (the golden pin) and the negative electrode is directly glued with conducting epoxy to the body of the mover, which together with all other metal supporting strcuture in the STM are all grounded. This "piezo-sandwich" will shear towards one direction under voltage, creating a linear motion when combined all stacks together as shown in Fig. 2.3 (c). Notice this motion is still within a tiny range (on the order of μm) and can only be maintained when there is a constant voltage applied. Once the voltage is withdrawn, the piezoelectric stack will shear back and the motion is gone. So we still need to figure out a way to generate a much larger motion that is also much easier to generate. The trick comes to that instaed of apply a constant voltage, one could apply a high frequency triangular voltage as shown in Fig. 2.4. At the increasing edge, the voltage increases linearly with respect to time, generating a linear motion. And at the steep decreasing edge, the piezoelectric stack will shear back fast, while the position of the bar will not move back that much due to limited friction. Hence after one cycle there will be a net displacement and this displcament

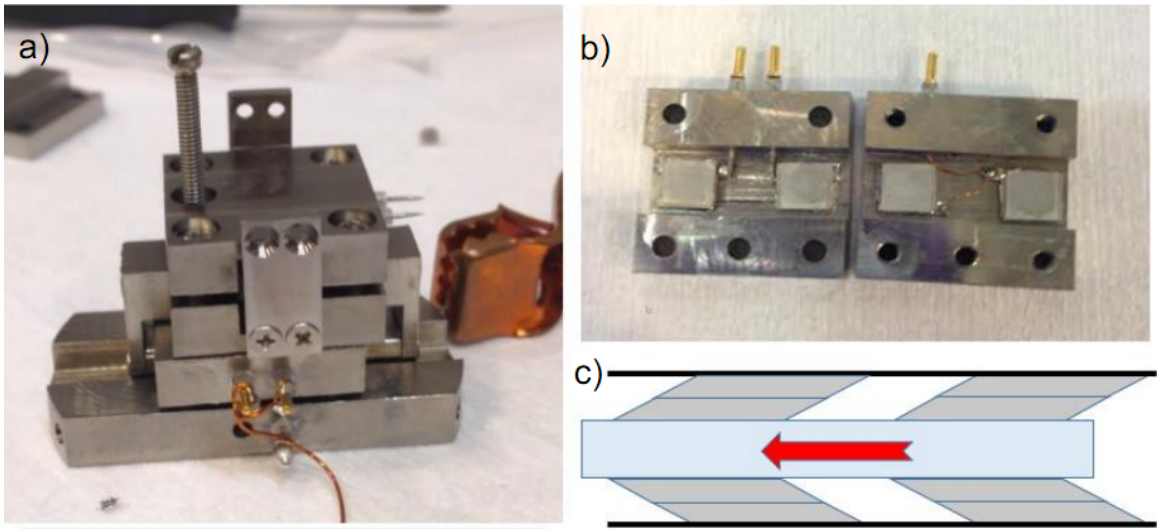

Figure 2.3: The piezostack for coarse x-y motion (a) the fully assembled coarse x-y mover (b) the disaseembled horizontal coarse mover. The white rectangles in the middle are the piezoelectric stacks. (c) cartoon showing how a horizontal motion is generated. [6]

will be accumulated in many cycles, resulting a visible motion. As one could imagine, the amplitude and speed of this motion can be set by adjusting the amplitude and frequency of the triangular wave. In average measurement conditions we choose $V_{\text{peak}} = 180V$ and $f = 1\text{Hz}$ for coarse x-y motion.

The coarse z motion is achieved with similar piezoelectric stacks with slightly different geometry. There are in total 3 synchronized groups of stacks forming a equilateral triangle, holding a prism inside on which the fine scan tube is placed. When fully assembles, the x-y movers will be placed on the top part of the inner container cyclinder, with the sample facing down, and the coarse z mover will be placed on the bottom part of the inner container cyclinder, with the fine scan tube and tip pointing up. Everything is suspended by 3 springs to damp vibration and then surrounded by 2 radiation shields to realize better temperature stability as described in 4. The details of controlling temperature is also included in 4.

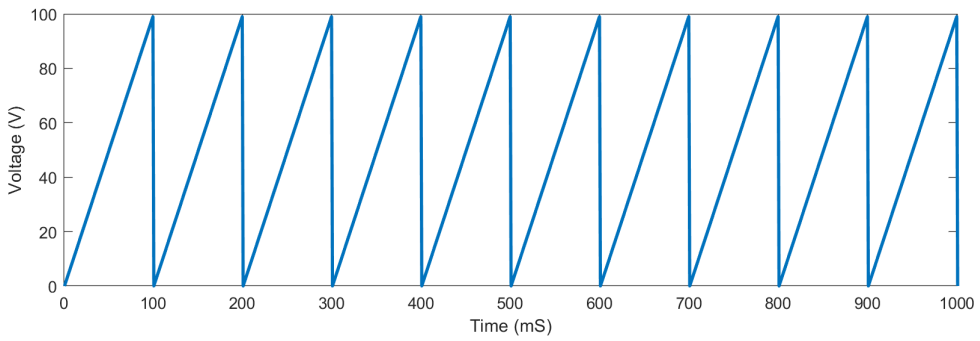

Figure 2.4: The triangular wave drives the coarse mover. The real parameter will be different depending on the temperature

2.3 Tip fabrication and preparation

In order to get atomically resolved topography image, it is apprent that the probe tip also needs to be atomically sharp. Therefore unlike AFM which has matured commercial probe tips, STM in general prefers custom fabricated fresh tips. As a widely studied area, many methods to prepare a STM tip has been posed and verfied[39, 40, 41, 42]. Here we only introduce the electro-chemical etching method we use to prepare STM tips.

The schematic cartoon and the tip ecthing setup is shown in Fig. 2.5. A thin metal wire (typically tungsten or Platinum/Iradium alloy wire, diameter around 0.25 mm) is cut into several pieces with length around 1cm. The wire is hold by a alligator clamp and held above $NaOH$ solution of 6 Mol/L concentration. A small ring made of tungsten is first submerged into the solution and then raised slightly above the liquid level. Due to the surface tension there will still be liquid inside the ring. Then the wire is carefully inserted into the ring, with it being roughly at the center and about 1mm submerged into the solution (the vertical displacement is adjusted by 2 lifting platform and 1 micromanipulator). When everything is setup, a DC voltage of 6V is applied to the setup, where the positvie electrode is connected to the wire and the negative to the ring. Then the following reaction (taking tungsten for example) happens:

$$W + 2OH^- + 2H_2O \rightarrow 3H_2 \uparrow + WO_4^- \tag{2.2}$$

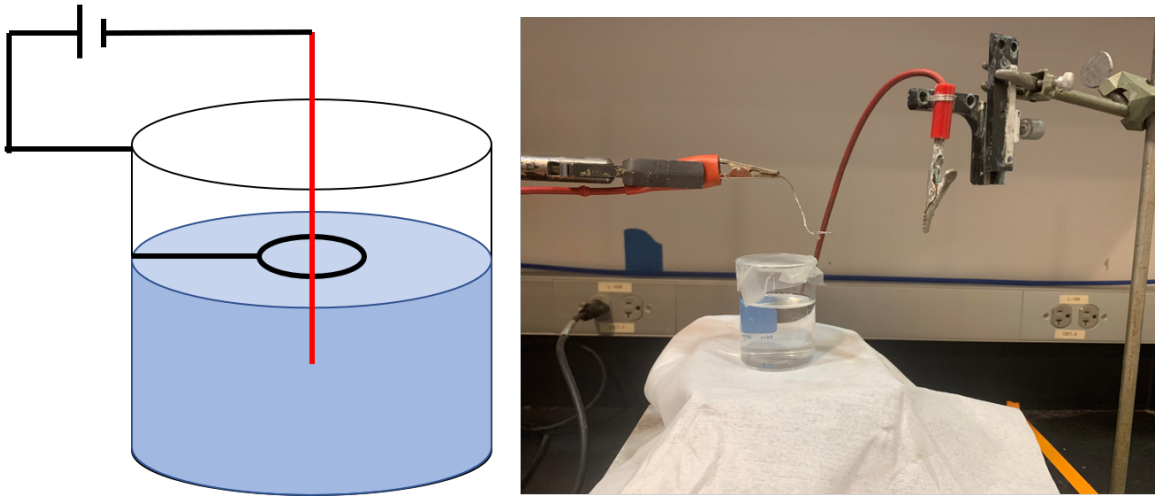

Figure 2.5: Left: the cartoon of tip etching. Right: the tip etching setup

This reaction mostly happens at the position where wire meets the solution, hence it will gradually etch the tungsten at that point. With the etching going, the diameter of the wire gets smaller and smaller, and eventually shrinks to a point and break the wire. Since the wire no longer makes contact with the solution, no further reaction will happen. Typically the break point will be a very sharp apex as showin in Fig. 2.6. This wire is then further cut into about 5mm and installed on the fine scanner as a tip.

Although visually the breakpoint of the wire already looks very sharp, it still needs further in-situ tip conditioning to make the tip ideal for experiments. As a start, in many experiments the freshly etched tip is annealed at high temperature to remove the surface contamination like oxides. This is exceedingly common for tungsten tips as they get oxided very fast when exposed to atomsphere. Although this step is important, in our experiment it is not conducted due to the physical limitation. In our system there is no easy way to install a tip in-situ (meaning when the STM is running in UHV, there is no way to change tips. Unfortunately for our system the tip changing requires venting the chamber to take the STM out), hence there is no carrier for tip to conduct the annealing. Instead, we apply another commonly used tip conditioning technique, field emission, to clean the tip. Field emission was dicovered around 1930s by several scientists [43]. It describes the process that

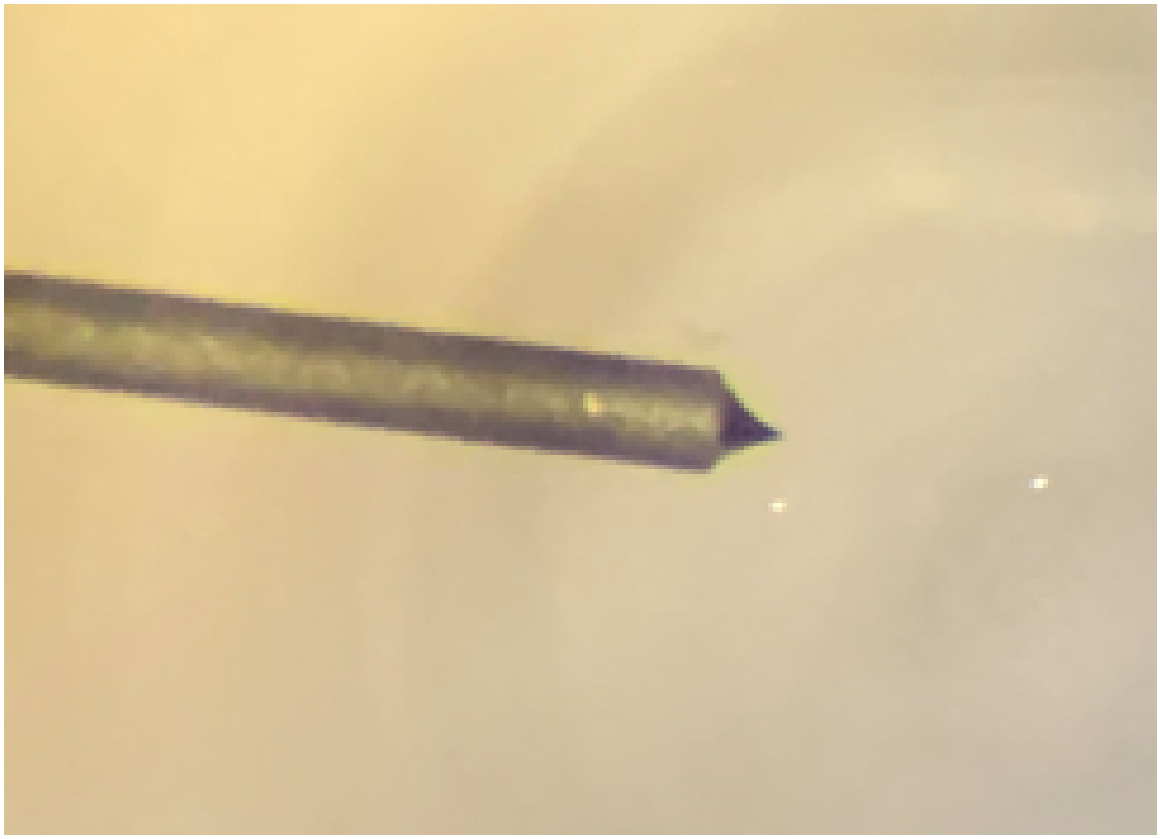

Figure 2.6: The tungsten wire after etching.

electrons (and possibly other particles) leave the material's surface in the presence of a large electric field. Long after its dicovery, it was applied in STM tip conditioning [44] by applying a large bias voltage betwen the tip and a precleaned metal surface (typically gold). Due to the pronounced sharpness of the tip and extremely small distance betwene the tip and the surface, even under a moderate bias (100 - 200V) the induced electric field will be quite large ($10^9 V/M$). In the presence of such large field, loosely attached particles (say the contamination particles) are likely to leave the surface of the tip and are deposited to the surface of gold. In a certain extent this process is like moving the contamination particles to the gold surface, which acts like a garbage can. Hence field emission procedure is also often called when the tip is contaminated, say after crashed onto the sample surface. Also during the field emission process, to accelerate the cleaning we will intentionally crash our tip onto the gold surface (like "dump" all the junk onto the surface). The field emission is done when the tip can comfortably react to the changing of current set point (1nA/S). After field emission, we move the tip to a clean area of gold surface and scan that area. Here a final trick of intentional "poking" is applied. This is done by conducting a I-Z measurment while reducing the distance between the tip and surface, typically in the end with the tip being slighty pushed into the gold. This poking helps the tip to have symmetric shape and further clean its surface. In the end with a ideal tip and gold surface, the following topography shown in Fig. 2.7 should be obtained.

Despite of a step on the top left corner of the image (2.7 (a) (c)) , the most significant feature of the gold (111) is a unique texture pattern called the herringbone [45], which gets its name from the herringbone fish, a fish known for their many parallel and slanted bones. This is a surface reconstruction which happes during the annealing in the gold preparation process (see A) to maximize the contact between gold atoms. This feature has been thoroughly studied that it has a 6.3nm spacing as shown in Fig. 2.7 (b). Before getting image of such quality, all the in-situ tip conditioning approaches are applied in sequence to imporve the tip quality. When topography of such quality is obtained, the tip is in an ideal working condition and is ready for measurement.

Finally as one could see, the gold (111) surface plays a vital role in tip preparation and conditioning. Hence it is significant to have a clean gold surface. Though commonly used

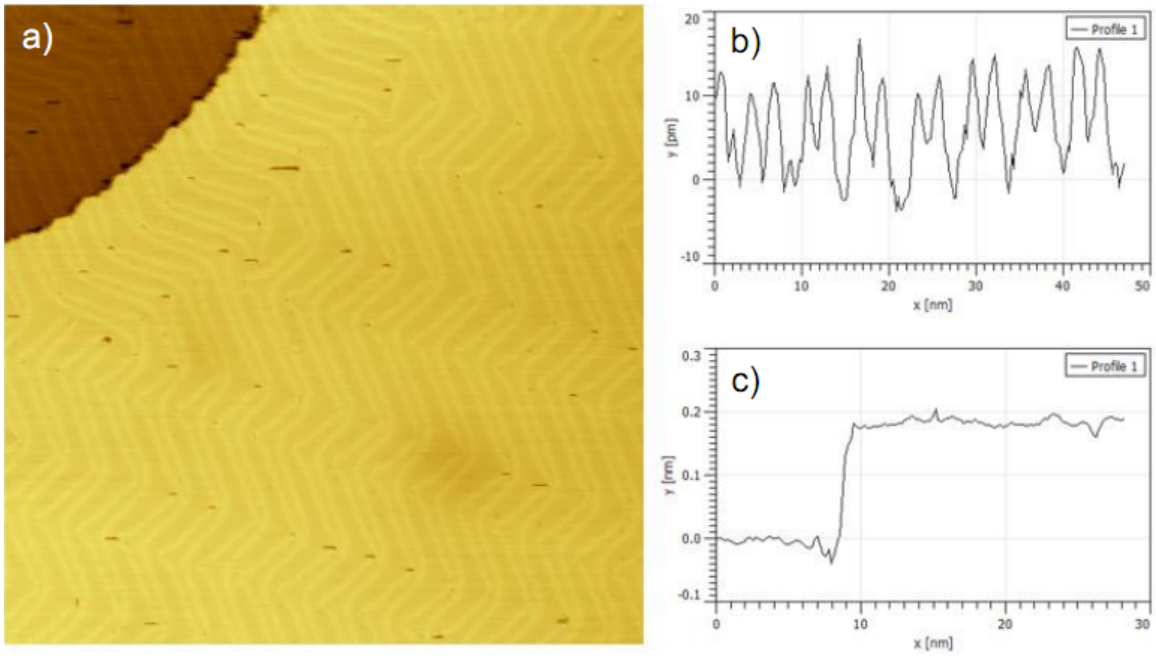

Figure 2.7: (a) the topography of gold surface. (b) the topography profile of the herringbone. (c) the topography profile of the gold steps [6]

in pretty much all STM experiments, the gold preparation is not in the scope of this thesis. We have attched a systemmetic way for gold preparation in the appendix (A)for interested readers.

Chapter 3

Introduction to Calcium Ruthenates

Among all strongly-correlated materials, the layered ruthenates is definitely one of the most unique system. It features a rich phase diagram, covering exotic states like superconductivity, antiferromagnetism, Mott-Hubbard insulator, etc. As a member of ruthenates, while having its unique property, Ca_2RuO_4 shares many similarities with other ruthenates compounds. Hence in order to comprehensively understand the physics inside Ca_2RuO_4, it is important to have a brief overview of the ruthenates family. In this chapter we first present a short summary of the ruthenates properties based on past researches, then we introduce several unique features of Ca_2RuO_4, including the metal-insulator transition, the current induced dimagnetism. At last, although the transition mechanism is still unclear, we introduce some theoretical background that is related with Ca_2RuO_4, which is beneficial for our understanding anyway.

3.1 An overview of layerd ruthenates

As described above, the Ruddlesden-Popper series is one of the most complicated series that exhibits a widely diverse phenomena. Among all Ruddlesden-Popper series, the one most relevant with this thesis is the layered $(Sr, Ca)_{n+1}Ru_nO_{3n+1}$, where n is the number of $Ru-O$ layers. The structure of a few compounds of Ruddlesden-Popper series are shown

in Fig. 3.1. The basic structural component of such structure is the octehedron formed by the metal cation (Ru in our case) and oxygen atoms surrounding it. These octahedra are linked by briding oxygen atoms, forming several $Ru-O$ layers.When the number fo layers is 1 ($n = 1$, i.e Ca_2RuO_4), all layers are identical hence forming a 2D structure. With the number of layers increasing, the crystal gradually turns from 2D to 3D. Finally when $n = \infty$, the crystal turns into $CaRuO_3$, which is a fully 3D perovskite structure with RuO_6 octahedra rotated and tilted.The correponding lattice parameters are listed in Table. 3.1.

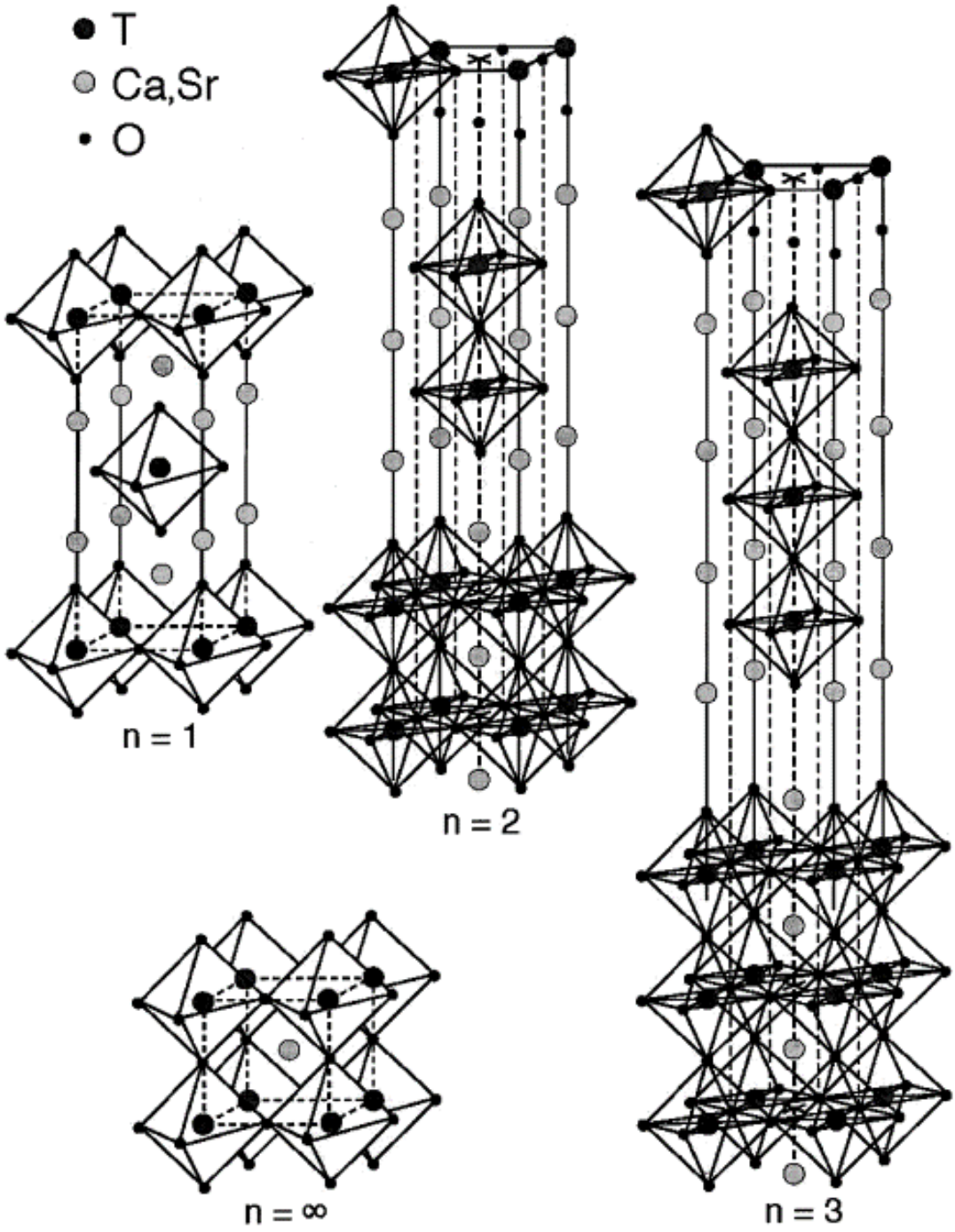

Figure 3.1: Crystal structure of the Ruddelsden-Popper Series $(Sr, Ca)_{n+1}Ru_nO_{3n+1}$. T is the metal cation.[7]

n	Element	a(Å)	b(Å)	c(Å)	Symmetry Group	$Ru0_6$ (rotated/tilted)
1	Sr	3.87	3.87	12.74	I4/mmm	No
	Ca	5.41	5.49	11.96	Pbca	Yes
2	Sr	3.90	3.90	20.70	I4/mmm	No
	Ca	5.54	5.37	19.59	$Cmc2_1$	Yes
∞	Sr	5.53	5.57	7.85	Pbnm	No
	Ca	5.52	5.35	7.65	Pnma	Yes

Table 3.1: Lacttice Parameters for $(Sr, Ca)_{n+1}Ru_nO_{3n+1}$ at T = 295K [7]

Although the sharing same structure, there is a huge difference between the Sr compounds and the Ca compounds, due to octahedron orientation stemming from the different radius of the Ca and Sr ions. This tiny difference in ion radius (1.0Å for Ca and 1.18Å for Sr) leads to a drastic distorstion in the lattice of Ca compounds, including a rotation of the RuO_6 octahedron around the c-axis, the tilt of the octahedron towards the a-b plane, and a lattice compression in the c-axis. This is most pronounced in the n = 1 Ca_2RuO_4 crystal, where the rotation and tilt angle are 11.8° and 12.7°. As shown in later discussion, this unique structure feature greatly affect the Ru atom and creates the exotic properties of Ca_2RuO_4.

The temperature phase diagram is shown in Fig. 3.2. The ground state of all Sr bearing compounds is a ferromagnetic metal state, with a notable exception of Sr_2RuO_4, which has a superconducting ground state. For other Sr ruthenates, the transition temperature (Curie temperature, T_c) increases with number of the $Ru - O$ layers, n. Above the T_c, all Sr ruthenates become a paramagnetic metal. The behavior for Ca bearing compounds are more complicated. For finite n, the Ca ruthenates have a antiferromagnetic insulating ground state. With temperature increasing, most Ca ruthenates will experience a metal-insulator transition, with the exception of $n = \infty$ compound, $CaRuO_3$, which is always a paramagnetic metal. This metal transition temperature as well as the Neel temperature (T_N) both decrease with n (in the end the transition temperature is 0 as $CaRuO_3$ is always metalic). More interestingly, between the low-temperature antiferromagnetic insulating

states and the high-tmeperature paramagnetic metal states, there is a paramagnetic Mott insulating phase for $n = 1$ and a antiferromagnetic metal phase for $n = 2$.

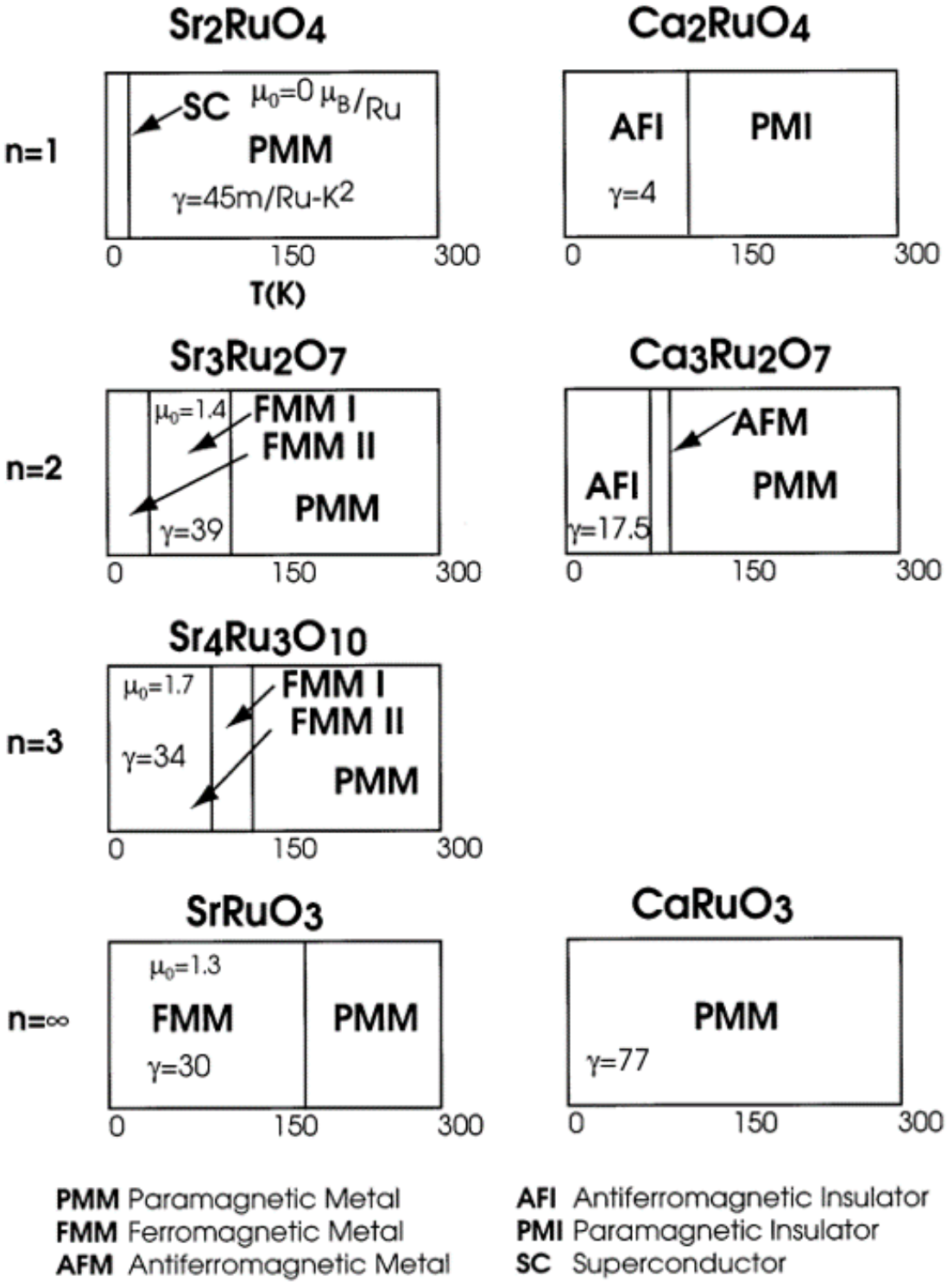

Figure 3.2: The temperature phase diagram of $(Sr, Ca)_{n+1}Ru_nO_{3n+1}$ series..[7]

The comparison between properties of Sr bearing compounds and the ones of Ca bearing compounds highlights the significance of the lattice degree of freedom. Therefore now we move our attention to the specific case of $n = 1$, in which the lattice ditorsion is the most prominent. The phase diagram of $Ca_{2-x}Sr_xRu_2O_4$ is shown in Fig. 3.3. The large area on the right side ($0.5 \leq x \leq 2$) of the figure indicate the case where Sr plays the dominating role. In this region the system is a paramagnetic metal, with the extreme $x = 2$ case entering superconductivity at $T = 1.5K$[46, 47]. In this region the octahedra show a rotation around the c-axis, while the d orbitals still remain degenerate. Moving to the left, as Sr gradually replaced by Ca ($0.2 \leq x \leq 0.5$), the system turns into a magnetic metal. In this region apart from the continued rotation, the octahedra start to tilt a bit, together with a compression in the c lattice parameter wihch lifts the orbital degenracy. Finally with Ca plays the dominate role ($0 \leq x \leq 0.2$), the lattice distortion is maximized and the orbital degenracy is fully lifted, reuslting a orbital ordered state. In room temperature, the d_{xy} orbital has lower energy than the d_{xz}, d_{yz} ones due to Jahn-Teller effect (see section 3.3). The orbital occupation for these 4 cases is shown in Fig.3.4.

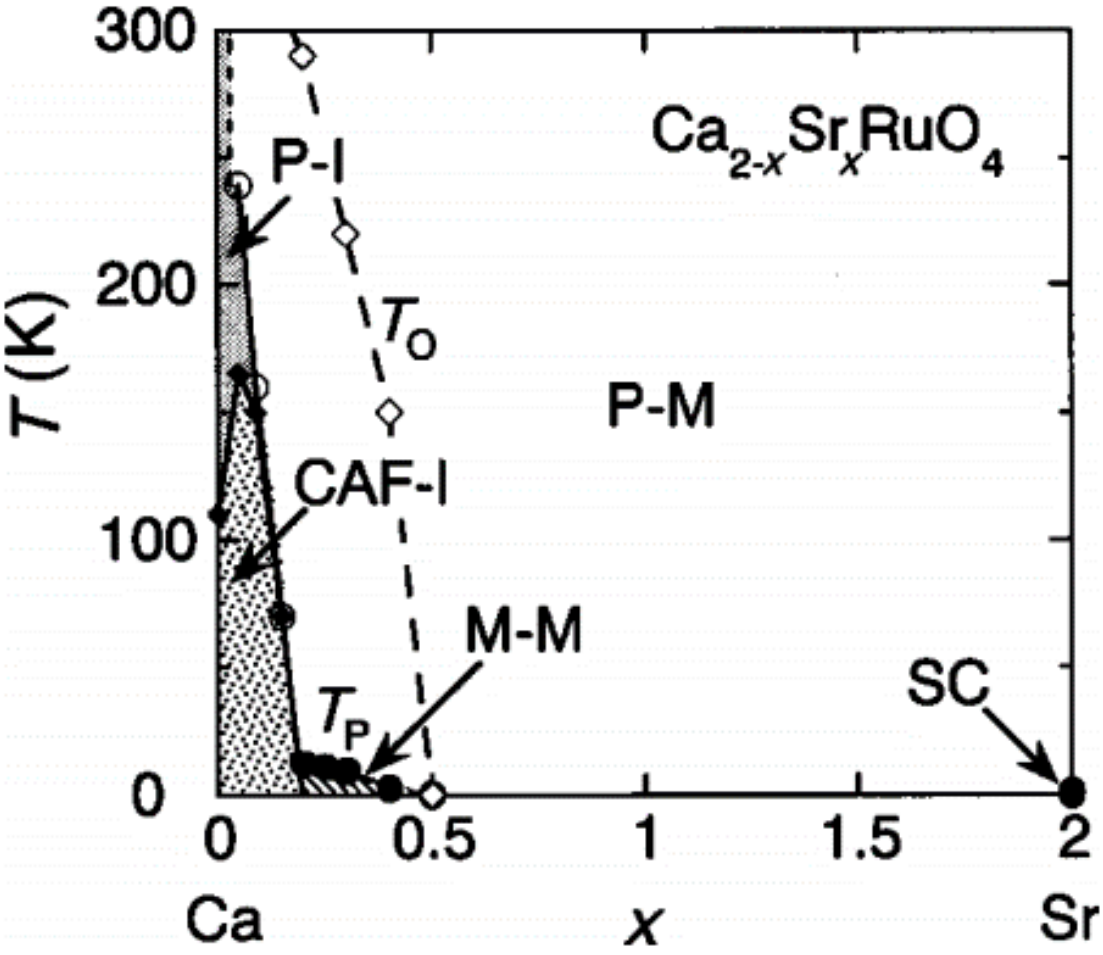

Figure 3.3: The phase diagram of $Ca_{2-x}Sr_xRu_2O_4$ series.[8]

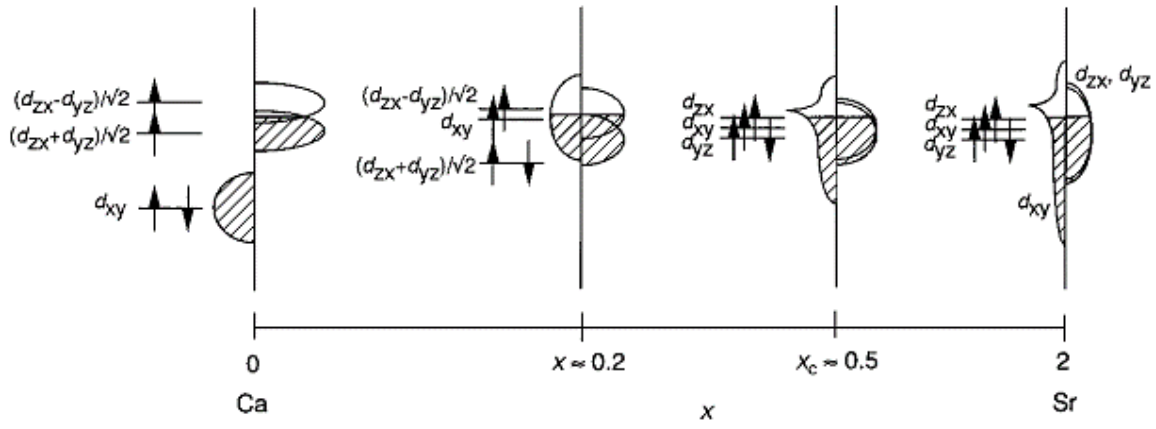

Figure 3.4: The low-energy t_{2g} orbitals of the $Ca_{2-x}Sr_xRu_2O_4$ series.[8]

The metal-insulator transition is specifically addressed in this thesis. The transition can be induced by temperature, pressure/strain[48] or dc current. Here we take the temperature driven transition of the Ca bearing compounds as an example, which is shown in Fig. **??**. For $n = 1$, there is a sharp jump in the resistivity curve at $T = 357K$, indicating a first-order transition into metal phase.The difference between the resistivity of the metal state and the inuslating ground state is more than 10 orders of magnitues. The transition temperature for $n = 2$ is much lower, with a much smaller difference in the resistivity between the metal and insulating phases. This trend continues to the limit of $n = \infty$, where the transition is gone and the material always stats at the metal state. These metal-insulator transition in general is the result of electronic instability, which is highly related with the dimensionality and the lattice distortions[7]. Such transition is not observed in the Sr bearing compounds.

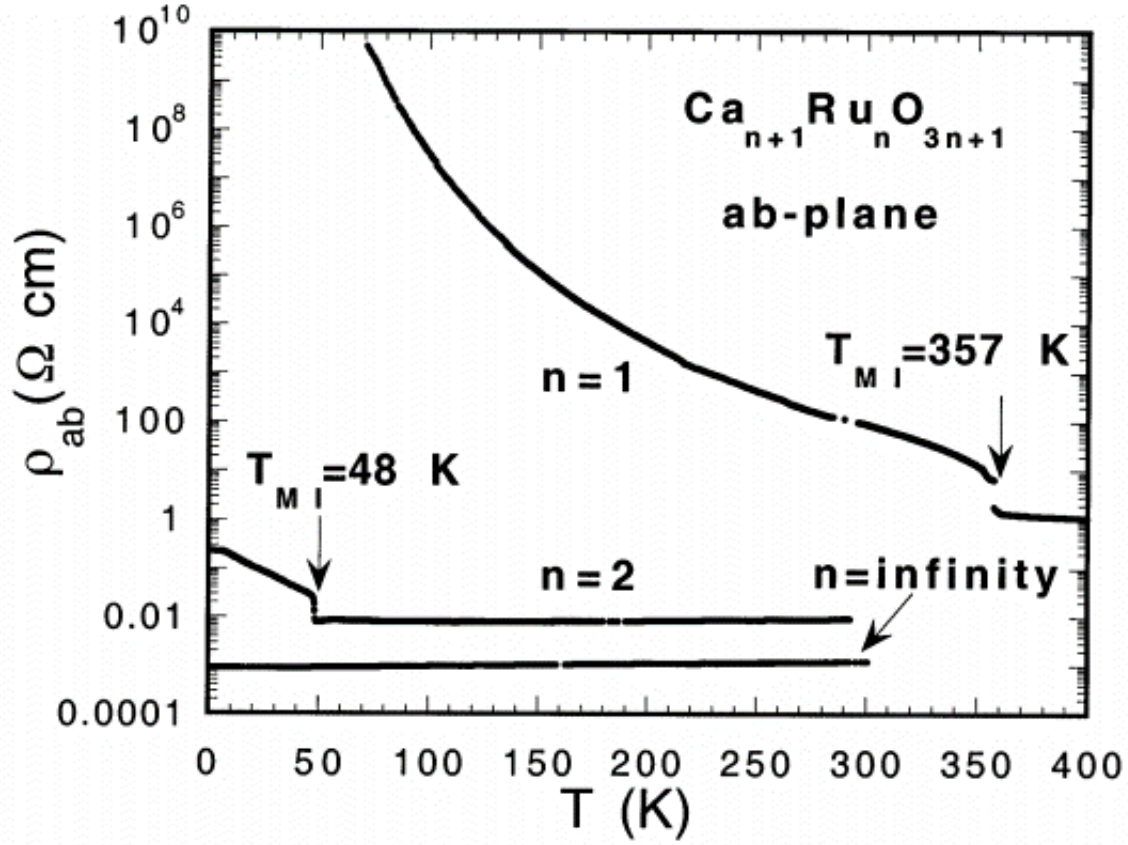

Figure 3.5: The in-plane resitivity versut temperature for $Ca_{n+1}Ru_nO_{3n+1}$[7]

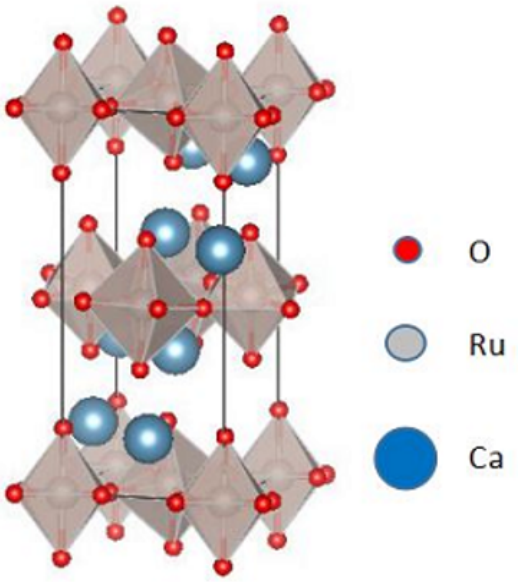

Figure 3.6: Unit Cell of Ca_2RuO_4 [4]

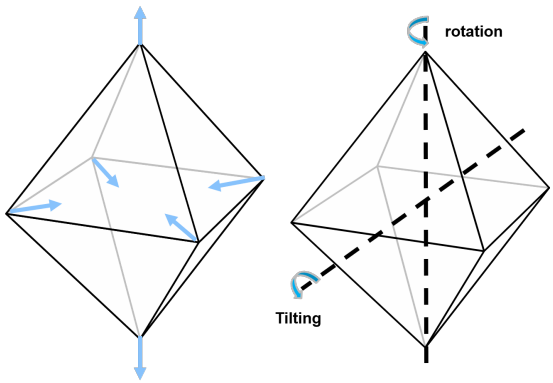

Figure 3.7: Lattice distortion, rotation and tilting of Ca_2RuO_4

3.2 Property of Ca_2RuO_4

Among all Ruddlesden-Popper series, Ca_2RuO_4 is definitely the one of the compounds that draw most academic attentions. Its sensitive response to a wide variety of degrees of freedom (lattice, orbital, temperature, pressure, electric/magnetic field etc) enables researchers to characterize its properties from all aspects. Over years of research, poeple gradually discovered a phase diagram of Ca_2RuO_4 with rich features, as shown in Fig. 3.8. In this phase diagram, 2 types of metal-insulator transitions, a temperature driven one and a current driven one, can be found. To understand the nature of these phase transitions, it is essential to have a thorough overview of the characteristics obtained from past studies. Here we present a brief summary of properties of Ca_2RuO_4.

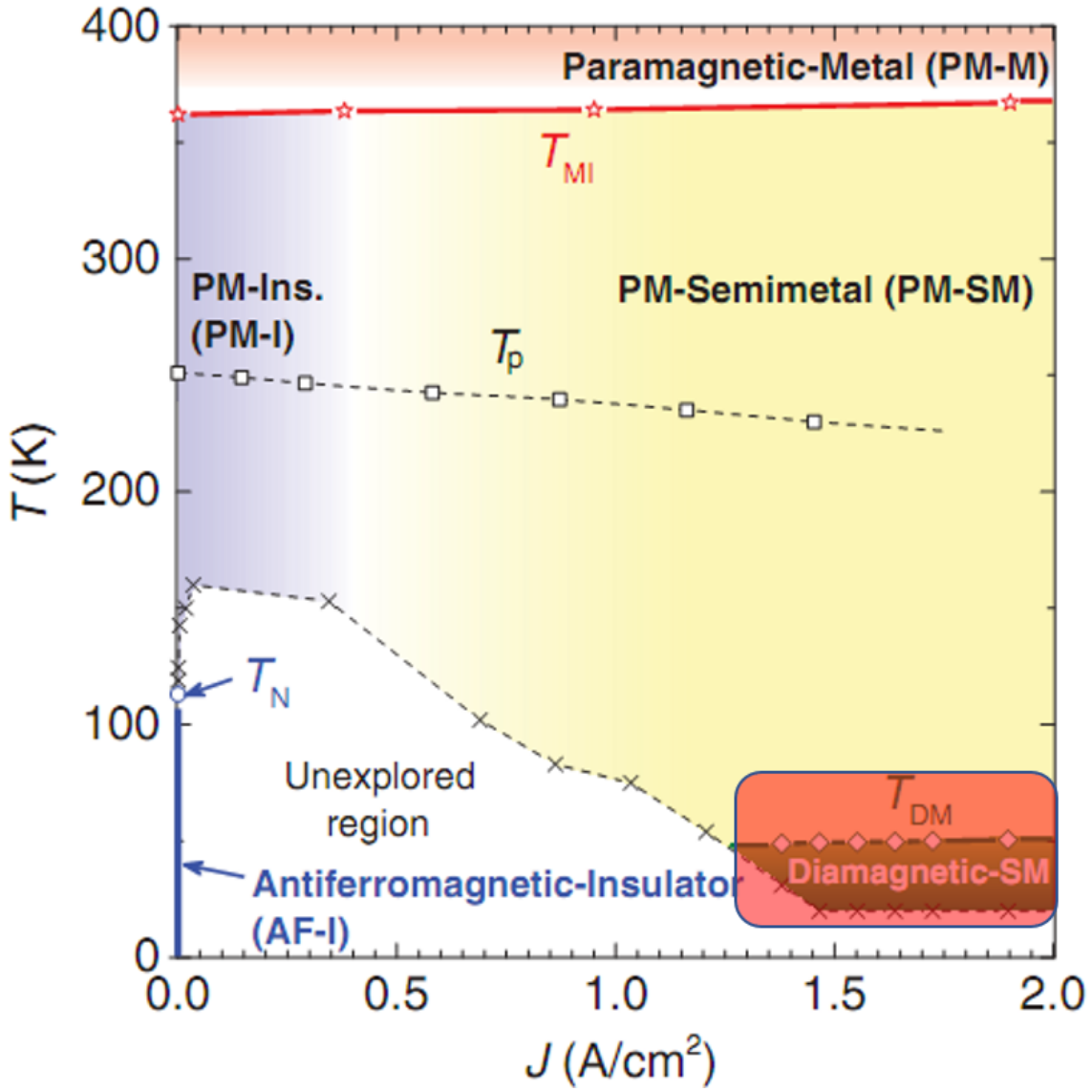

Figure 3.8: Phase diagram of Ca_2RuO_4. Note the diamagnetic semimetal phase (red semi-transparent box) has been found to be false. [2, 3]

3.2.1 Crystal Structure and Temeparure Driven Transition of Ca_2RuO_4.

The crystal cell of Ca_2RuO_4 is shown in Fig. 3.9 (a). The main structural component, the RuO_6 octahedra are linked by briding oxygen atoms, forming a layered quasi-2D structure. The octahedra are further rotated around the c-axis and tilted towards the a-b plane. This

rotation and tilt is closely related with the electronic properties of Ca_2RuO_4. The calcium atoms are mounted between $Ru-O$ layers and mark the position where the crystal cleaves. More interestingly, as shown in Fig. 3.9 (b), when seeing from top of the cleaved surface, the RuO6 octahedra are alternately tilted with respect to the c axis (most pronounced in the ac plane), and rotated in the ab plane as indicated by the straight and curved arrows, respectively. In the line marked by light orange box, the apical oxygen atom of the RuO6 octahedra are pointing towards each other, while in the light green box they are pointing away.

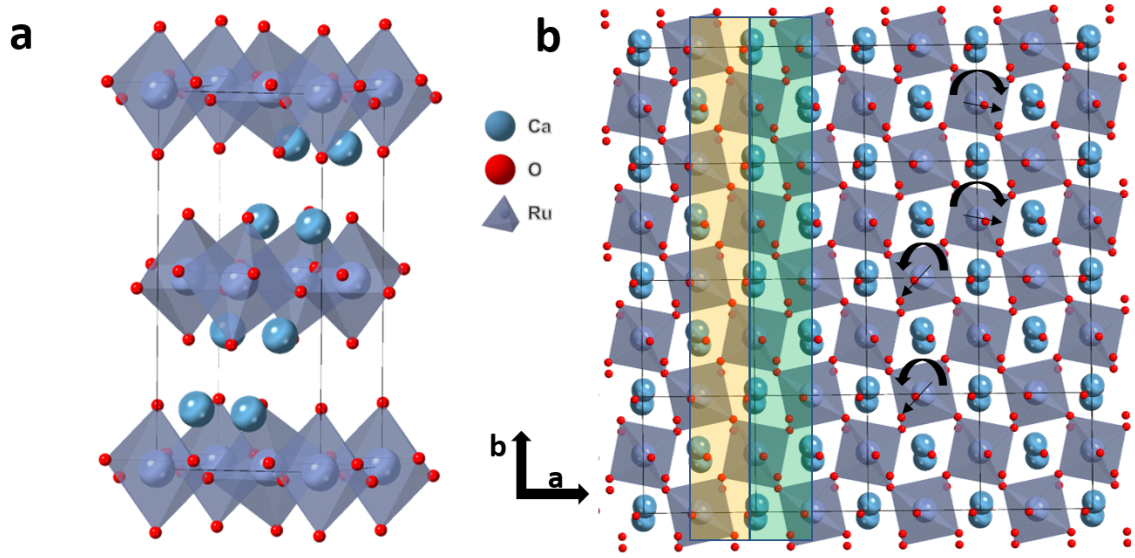

Figure 3.9: The crystal cell and top view of the cleaved surface of Ca_2RuO_4

At room temperature, the Ca_2RuO_4 features a compression in the c-axis. When the temperature goes below $T = 140K$, the crystal begins to show an antiferromagnetic order [49, 50], which is hard to access in our experiment as the resistivity is too large. When the temperature goes above the metal-insulator transition temperature of $T_{MI} = 357K$, the crystal will experience a symmetry preserving structural transition, characterized by a elongation of the c lattice constant. This change in the lattice constant is so drastic (4.3% [50]) that it not only greatly alter the volume of the crystal (it is quite often to observe the crystal cracks during the transition) but also modifies the orbital ordering of the Ru

atoms. As shown in Fig. 3.10. The Ca_2RuO_4 unit cell has a $Pbca$ symmetry. When the temperature is low, it is compressed in the c-aixs, therefore denoted as $S-Pbca$. When the temperature is above the transition, the lattice remains the same symmetry group while elongated in the c axis hence known as the $L-Pbca$. When the unit cell is compressed in c-axis, the energy of the d_{xy} orbital (the red solid line)is lowered and the energy of d_{xz} and d_{yz} orbitals is raised due to the Jahn-Teller effect (see Section. 3.3.2). Hence the 4 electrons in the $4d$ shell fully occupy the d_{xy} orbitals and leave the $d_{xz}-d_{yz}$ complex (the blue solid lines) half filled. As we will see in Section. 3.3.3, with proper electron-electron interaction, a half filled band will leads to a Mott-Hubbard insulator. When the temperature is raised above the transition temperature, the unit cell is elongated, hence the orbital ordering reverses. In this case, the d_{xy} band is half filled and the remaining hole is left in the $d_{xz}-d_{yz}$ complex.

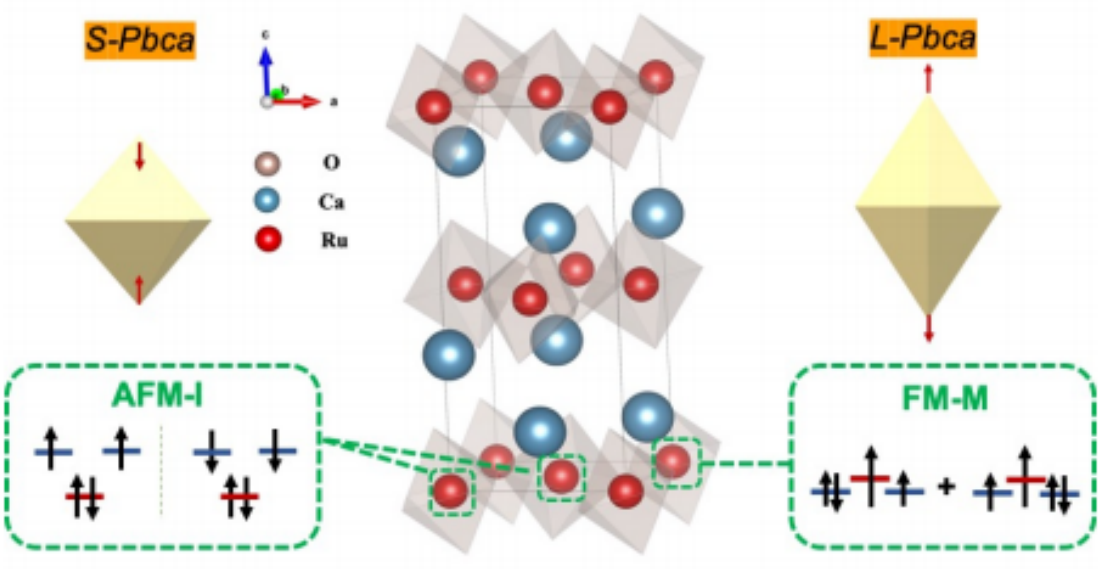

Figure 3.10: The oribtal ordering for the low/high temperature structure of Ca_2RuO_4 [9]

Due to the fact that the electrons in Ca_2RuO_4 are not "free" electrons, tradistional band calculation method like Density Functional Theory (DFT), which fundamentally solves single-particle problems, can hardly explain the electronic behavior in Ca_2RuO_4. Therefore

Dynamic Mean Field Theory (DMFT), a methodology that is designed to determine the electronic structure of strongly correlated materials, is applied in the field of ruthenates. For more information of DMFT please check Section. 3.3.5 as it is beyond the scope of this thesis. Based on the experimentally determined structure of Ca_2RuO_4, DMFT is able to generate the orbital resolved spectral weight of the Ru atom, as shown in Fig. 3.11. The blue dashed line is the result for the $T = 295K$ $S - Pbca$ structure and the black solid line is for the $T = 400K$ $L - Pbca$ structure. Both the d_{xy} orbital and the d_{yz} (which is very similar to d_{xz} orbital) shows a gap for the low temperature structure and a metal spectra for high temperature one[4]. Further calculation considering the occupation of different oribtals give similar result, as shown in Fig. 3.12[9].

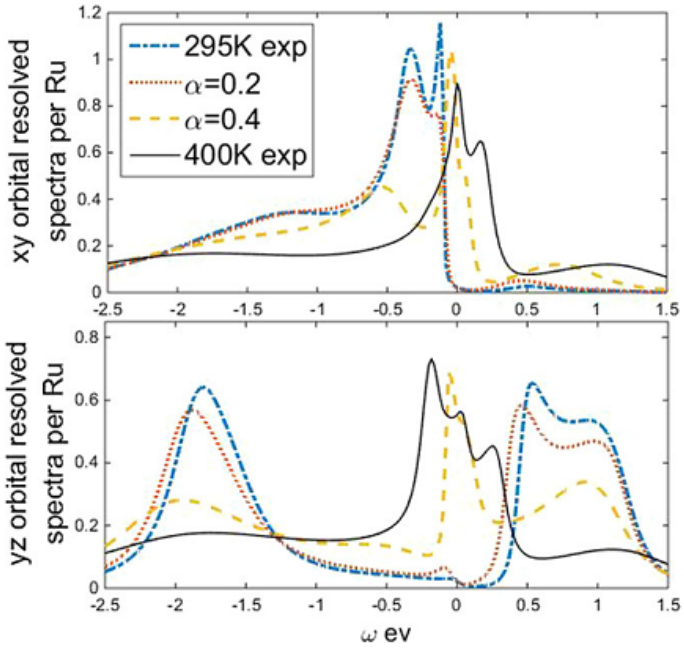

Figure 3.11: The orbital resolved spectra of Ru atom in Ca_2RuO_4 obtained from DMFT calculation. [4]

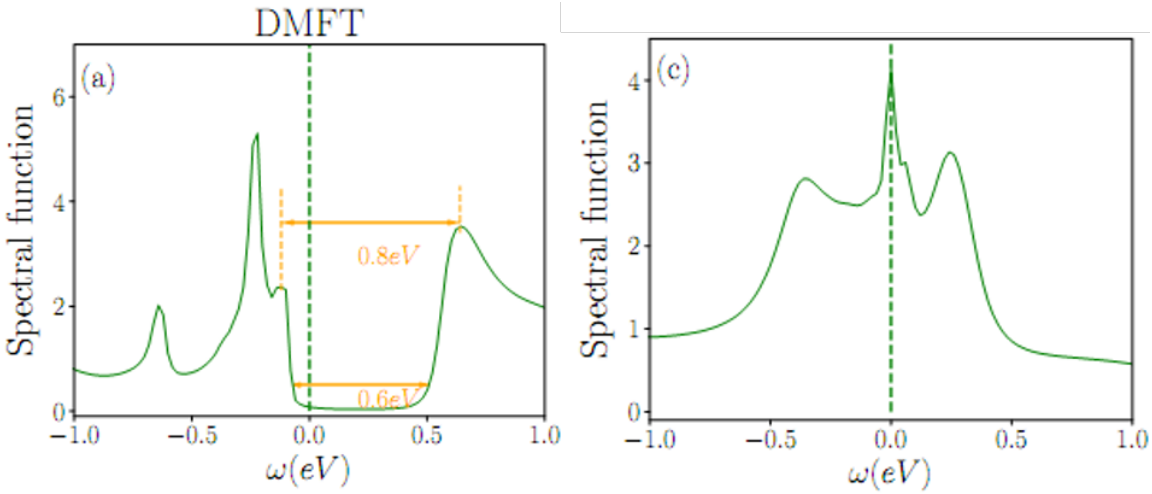

Figure 3.12: The DMFT calculation of spectra weight of Ca_2RuO_4 [9]

This temperature driven metal-insulator transition can be further explained in the scope of Landau-theory free energy[4], which clearly shows the importance of the structural change in the transition since it greatly affects the electron configurations.

3.2.2 Current Driven Transition

Apart from the temperature induced metal phase, Ca_2RuO_4 is found to have similar metal behavior when a dry-battery-level voltage is applied.[31]. Such metal phase is able to be maintained with a DC current. Though it was reported that there was a current-induced dimagnetic phase, it is recently discovered that such phase does not exist[2, 3]. The dimagnetic siganl observed previouly was due to experimental setup issue. Nevertheless, this has no influence on the current-induced metallic stata which was repeatedly observed.

In this thesis we mainly focus on the current driven metal-insulator transition, which has drew vast attention in recent researches. Shortly after the discovery of current induced metal phase in Ca_2RuO_4, scattering experiments show 2 new phases coexisting when the current is applied, as shown in Fig. 3.13[10]. The top left panel shows the neutron diffraction result for single crystal Ca_2RuO_4 at the equilibrium of $T = 130K$, while the bottom left one shows the reuslt of the same measurment done when a current of $J = 10A/\text{cm}^2$ is applied.

Clearly 2 seperate phases that are both different from the equilibrium S phase are observed. On the right panel is the fitted c lattice parameter vesurs temperature, in which the S^* phase has a very similar lattice constant with the equilibrium S phase and the L^* phase has a much longer lattice. This is very similar to the lattice distrotion in the temperature driven phase trasition, where the conducting metal phase has a larger c lattice constant than the room-temperature Mott-insulating phase.

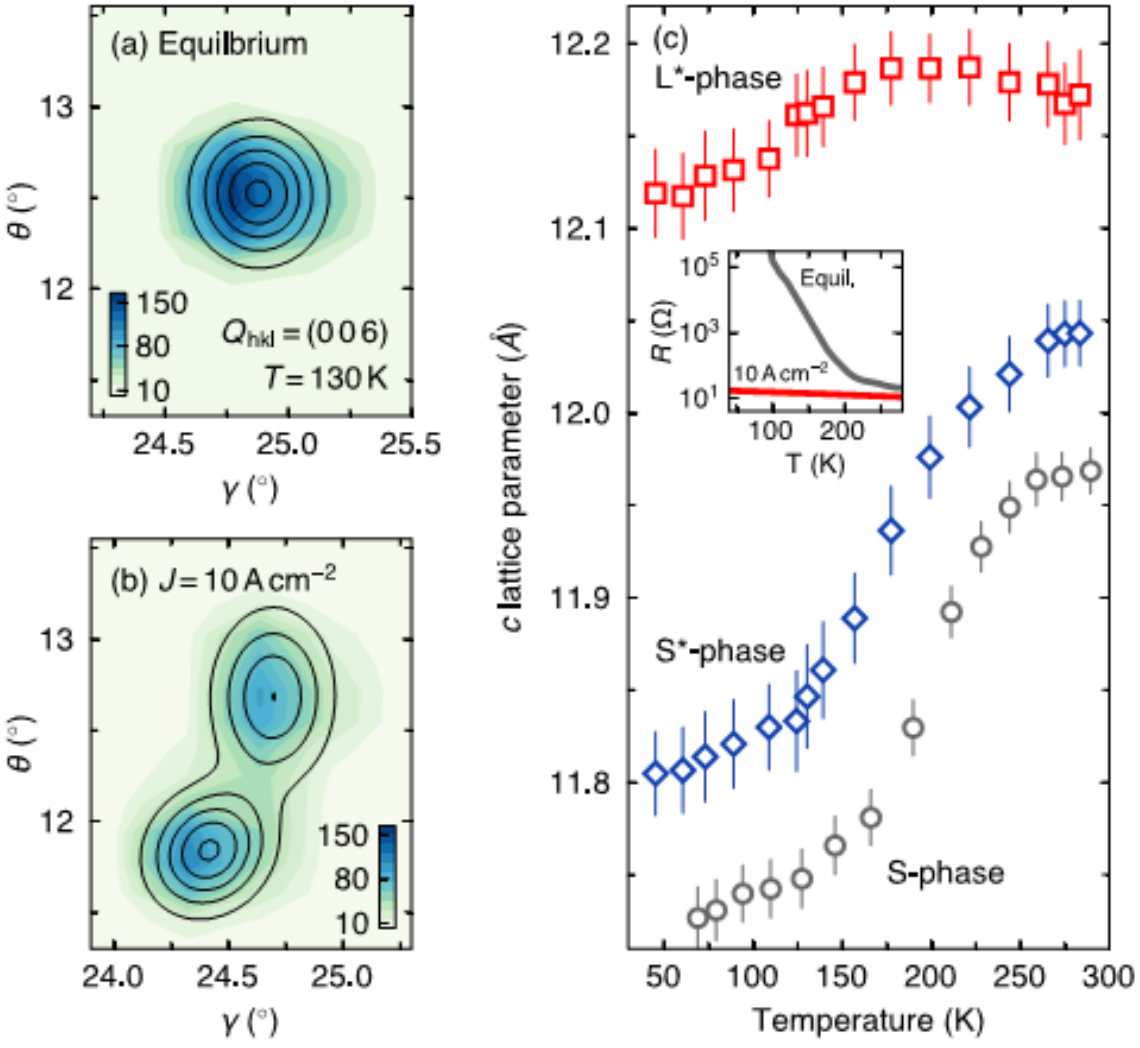

Figure 3.13: The neutron diffraction result of the equilibrium and current-induced metal state of Ca_2RuO_4 [10]

The X-ray diffraction (XRD) experients also show a coexistence of these 2 phases[10], as shown in Fig. 3.14. The top left panel shows the diffraction intensity at different source current, featuring a gradual suppression of the S^* phase and an emergence of the L^* phase. These 2 phases co-exsit when the source current is in $10 - 14$ A/cm^2 range. From this the phase proportion can be extracted, as shown in Fig. 3.14 (b) and (c). The significant hysterisis in (b) and (c) are also reported in other studies and observed in our experiments. This co-existence illustrated by XRD indicate 2 possible scenarios. The first one is there is indeed 2 distinguished phases different from equilibrium phases which obviously will result in 2 seperate peaks in scattering experiments. The second one is more subtle, that there is no such difference between equilibrium phases and current induced non-equilibrium phases. In this hypothetic case, the effect of current is to gradually switch some tiny part of the crystal into the metal phase, of which the proportion is positively related with the current. And the insulating phase is mixed with the metal phase in a nano scale, generating the gradually broadened peaks observed in the diffraction measurment. Both scenarios will have a homogeneous behavior in the perspective of scattering probes, yet can still be distinguished by local probes like STM.

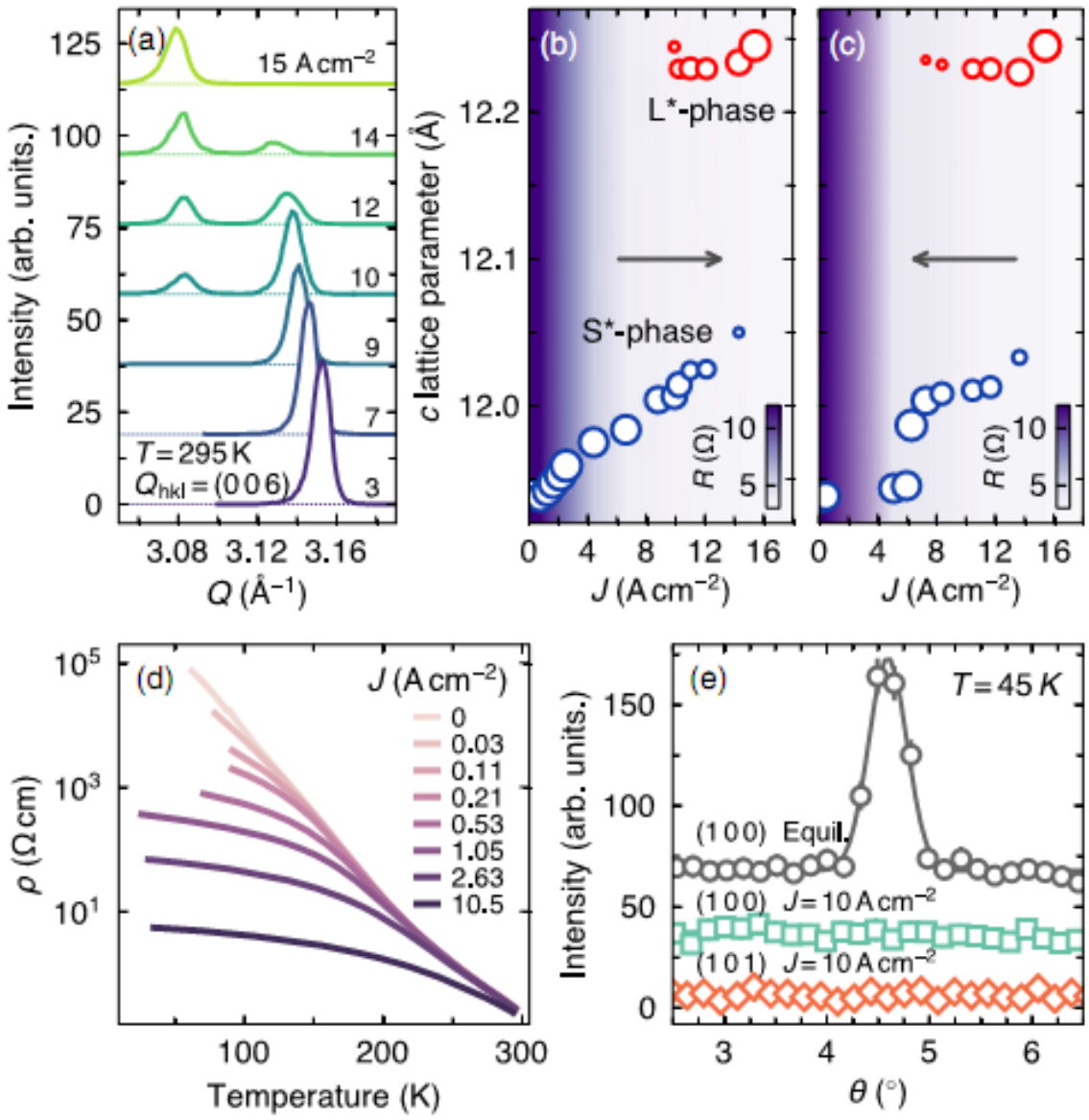

Figure 3.14: The coexistence of the S^* and L^* phase of Ca_2RuO_4 [10]

Unlike other phase transitions, the current driven metal-insulator transition can even be observed by bare eyes[11]. The sample is applied with a DC voltage. Intially when the source voltage is small, the crystal is still in the insulating phase characterized by a large resistivity. Hence the current increases slowly with voltage. Once the voltage reaches $5V$, theres is abrupt jump in the source current, indicating the phase transition to the metal

phase. From this point the crystal switches from voltage bias mode to current bias mode (For experimental details, please check [51]). With the current increasing, the source voltage drops due to more and more portion of the crystal entering the low resistive metal phase. What is even more interesting is, over this process, a dark phase (metallic phase) grdually nucleates from the negative electrode. Although this has been observed in [11], such phase propagation is not observed in our experiment. This might be due to the limited optical access in our experimental setup or the difference in crystals' properties due to different growth batches.

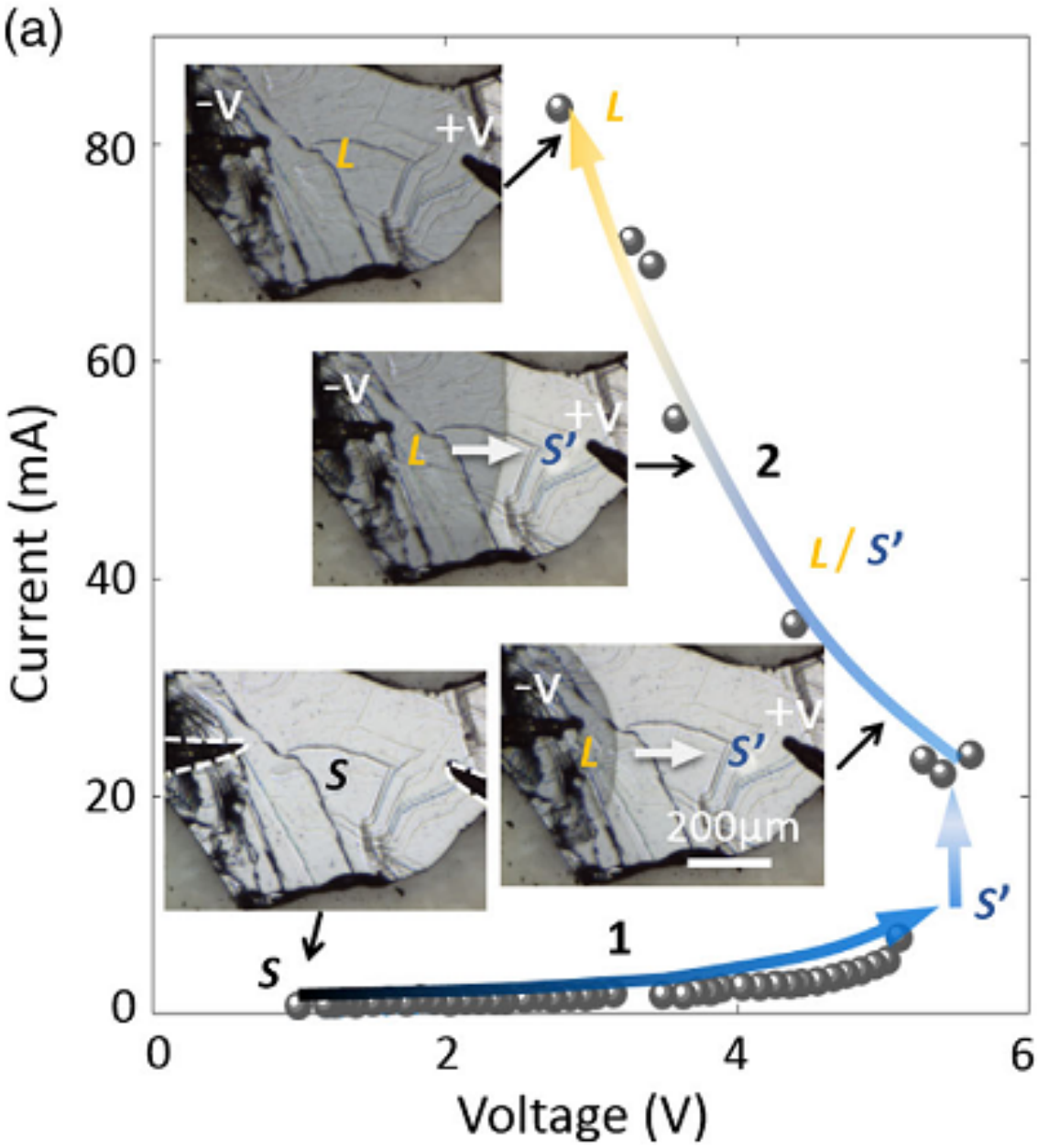

Figure 3.15: The current driven phase transiton of Ca_2RuO_4 observed by optics in visible light range [11]

Many other studies also focus on this current driven metal-insulator transition[52, 16] or the pressure induced phase transition[12] as shown Fig. **??**, which is also quite similar

with the temperature driven transition accopanied with a drastic strcutural change. As we will see in th following section, the strcture plays a vital role in determining the properties of Ca_2RuO_4. To understand this, we briefly introduce relevant theorectical background below.

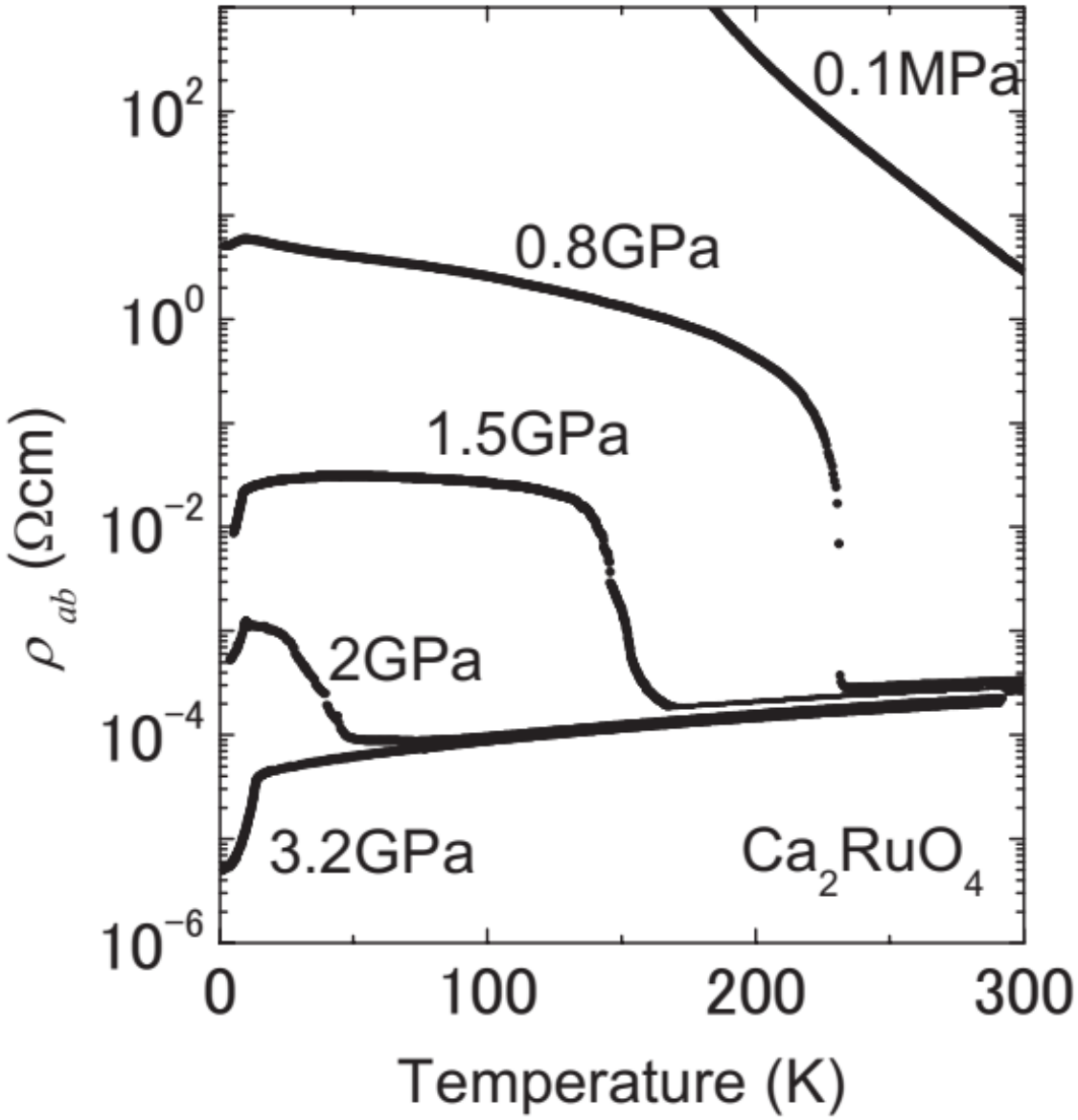

Figure 3.16: The pressure-induced metal-insulator transition of Ca_2RuO_4 [12]

3.3 Brief summary of relevant theoretical background

As an experimental subject, physics requires evidence from experiments to correctly describe the properties of materials, which later is summarized and modeled as theory. With the build-up of theoretical knowledge, more and more often the theorists propose unseen physics that verified by experimentalists later. Hence the experiments and theory are entangled as an organic entity for investigation on novel physics. Here we briefly summarize the relevant theory of Ca_2RuO_4 as they will more or less improve our understanding of mechanism determining its properties.

3.3.1 Crystal Field splitting

The crystal field splitting is definitely one of the most obvious effect happening in Ca_2RuO_4. It describes the process that the orbital degeneracy of one atom is fully/partially lifted when it is put into the lattice of a compound. For instance, in a Transitional Metal Oxide (TMO), there are interactions between the positively charged metal cation and the "free" electrons of the negatively charged ligand. These interactions typically have favored directions due to the lattice of the crystal. Therefore there must be some orbitals of the metal cation that are more close to/far away from the ligand, resulting in ernergy level shifts hence lift the degeneracy[53]. This phenomenon happens under the "crystal field" hence is named as crystal field splitting.

Take Ca_2RuO_4 as an example. The d-orbitals of the Ru atom are five-fold degenerate as shown in Fig. 3.17. It is clear that the $d_{x^2-y^2}$ and d_{z^2} orbitals are more aligned with principle axes than the rest d_{xz}, d_{yz} and d_{xy} orbitals, hence have a larger overlap with the electron clouds of the ligands. Therefore the electrons in these 2 orbitals will sense a stronger Coulomb repulsion and have a higher energy. In the end, under the crystal field the five-fold degeneracy is split into 2 groups: the lower-energy t_{2g} orbitals and the higher-energy e_g orbitals.

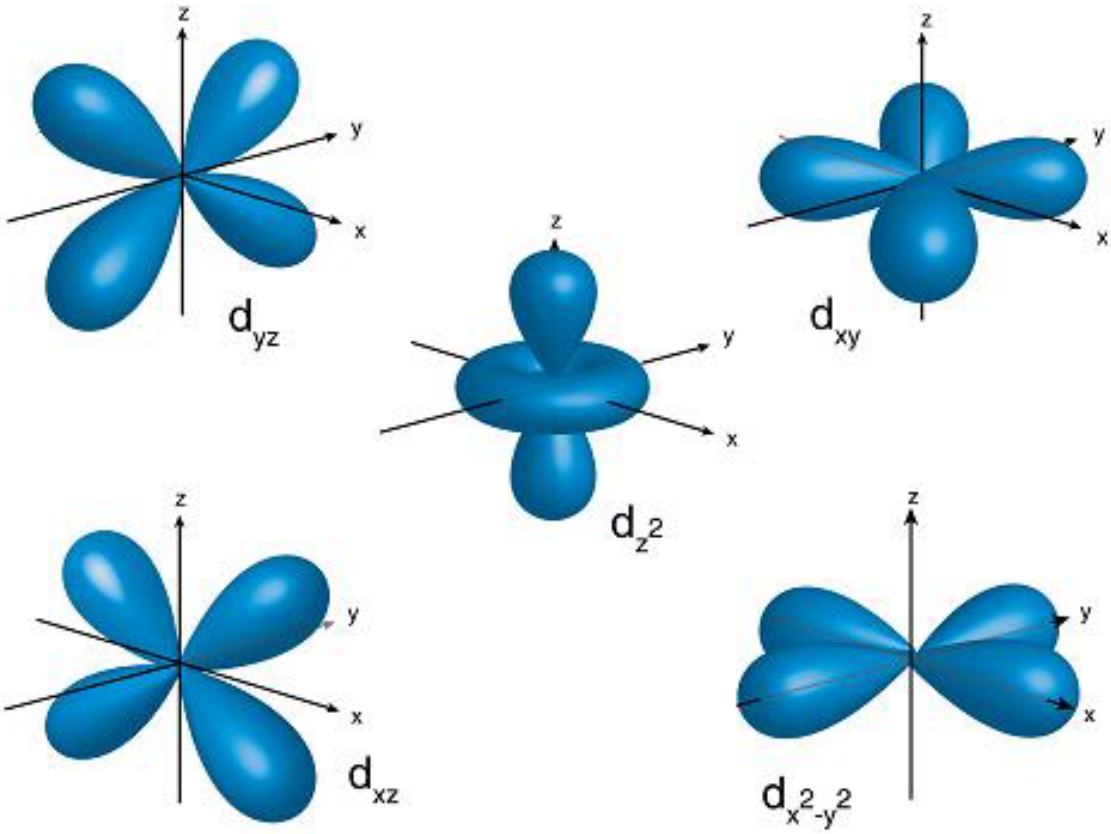

Figure 3.17: 5 orbitals of d shell [5]

After the splitting, the electron occupancy is dependent on both the splitting energy Δ_{cf} and the Coulomb interaction U. If the splitting is large enough, the electron will fill the t_{2g} orbitals before occupy the e_g orbitals. Otherwise due to large Coulomb repulsion, after the t_{2g} orbitals are singly occupied, the electron will singly fill the e_g orbitals before doubly occupying any t_{2g} ones. For the 4 $4d$ electrons of Ru atom, this theory will result in the 2 possible configuration as shown in Fig. 3.18. When the splitting is relatively small, the last electron is put in one of the e_g orbitals (the left panel). If the splitting is large, 2 electrons will doulby occupy one of the t_{2g} orbitals (the right panel). In Ca_2RuO4 split is roughly a few eV that it is large enough to force the electrons just occupy t_{2g} orbitals, as in the right panel of Fig. 3.18.

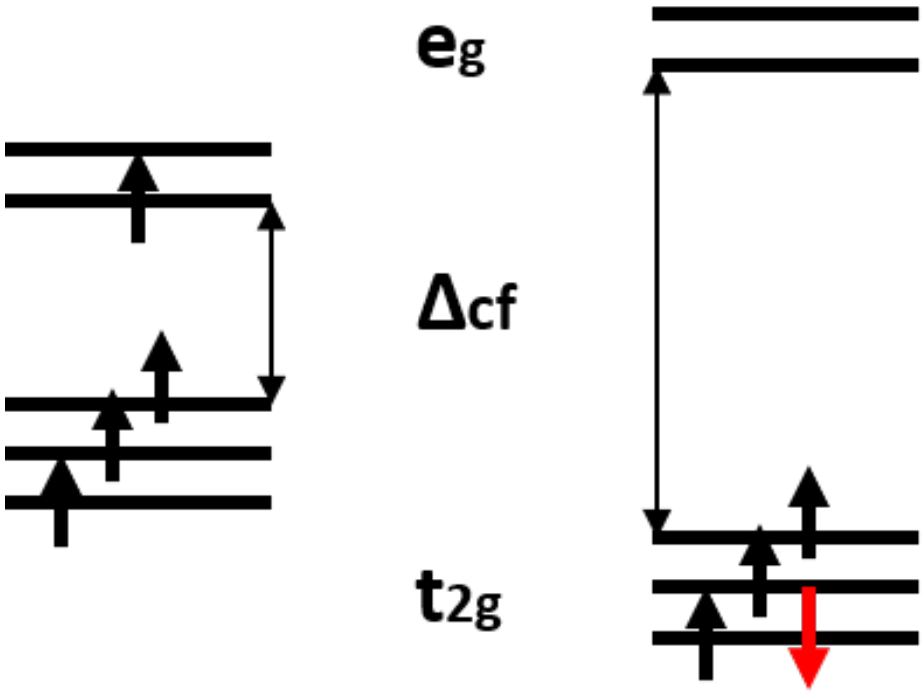

Figure 3.18: 2 possible cases for electron occupancy of the $4d$ electrons of the Ru atom after the crystal field splitting.

It is worth to mention that under different symmetry (lattice), the same atom can experience different crystal fiedl splitting.

Finally the crystal field spliitting can be easily taken into qunatitative consideration by the means of second quantization[54]:

$$H_{\text{cf}} = E_0 \sum_{i\sigma} (n_{ixy\sigma} - n_{ixz\sigma} - n_{iyz\sigma}) \tag{3.1}$$

where n is the number operator of the electrons and the σ denotes spin and the xy, yz, xz denotes corresponding orbitals of the 4d shell and the E_0 controls the crystal splitting amplitude.

3.3.2 Jahn-Teller Effect

Since the system always favors the lower energy state, it is possible for a lattice to distort if it lowers the total energy enough. In details, the energy spent on the lattice distortion

must be smaller than the energy saved from changing to the new electronic configuration from the old one. Typically this will happen in a systemd with a dengerate ground states, of which the degeneracy is removed after the lattice distortion. Such phenomenon is called Jahn-Teller effect and it has been observed in most transition metal oxides (TMO). Several studies point out the Jahn-Teller effect drives the CMR in some manganites[55, 56, 57, 58] and potentially explain the physics in ruthenates[56, 59].

Most TMO have an orthorhombic structure, meaning the metal cation is surrounded by six ligands forming an octahedron centered at the metal cation. The distrotion in such lattices are usually complicated, including rotation, tilting and compression/elongation of the octahedron. The overall outcome of such complex distortion is hard to interpret, therefore for simplicity here we focus on the compression and elongation along the c-axis of the octahedron (Strictly speaking it is not fully along the c-axis). When the octahedron is compressed, the ligands will come closer to the metal cation, causing the energy of orbitals with z component to raise. In the other case when the octahedron is elongated, the ligands will move further from the cation hence the energy of orbitals with z component will drop. In both cases the energy of the orbitals without z component is not affected. In summary this Jahn-Teller effect will fine tune the energy of each orbital and further lift the degeneracy in the e_g and t_{2g} orbitals.

In Ca_2RuO_4, the Jahn-Teller effect is shown in Fig. 3.19. As mentioned above, due to a large crystal field splitting, the e_g orbitals are not occupied. Hence we focus our analysis on the t_{2g} orbitals. When the lattice is elongated (left panel of Fig. 3.19), the energy of the d_{xz}/d_{yz} complex is lowered. And when the lattice is compressed, the energy of the d_{xz}/d_{yz} complex is raised, leaving the d_{xy} orbital fully occupied by 2 electrons and the d_{xz}/d_{yz} complex half-filled. As we will see later, this half-filled band together with strong electron-electron correlation stemmed from orbital localities pave the way to a Mott insulator.

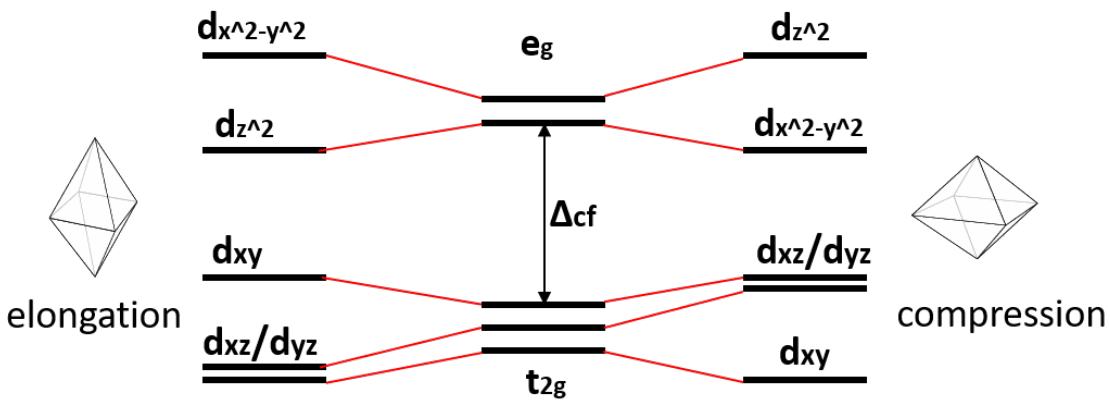

Figure 3.19: The Jahn-Teller effect on Ca_2RuO_4

Finnaly in order to quantitatively describe the effect of lattice distortions, one needs to find all the distortion modes. For Ca_2RuO_4, the relevant modes are $x^2 - y^2$ and $3z^2 - r^2$[56, 59] and the Hamiltonian for the distortion is:

$$H_{\text{lattice}} = k \sum_i (Q_{2i}^2 + Q_{3i}^2) \tag{3.2}$$

where the Q_{2i} and Q_{3i} denote the $x^2 - y^2$ and $3z^2 - r^2$ modes. In summary the Jahn-Teller effect highlights the significance of the lattice degree of freedom in the ruthenates. It and the coupling between other degrees of freedom and itself might be the main driving force behind the complicated physics in Ca_2RuO_4.

3.3.3 Mott-Hubbard Insulator

In a system where the electron-electron interaction must be considered, the simplest model is the Hamitonian below:

$$H = \sum_i \frac{h^2 \Delta_i}{2m_e} - \sum_l \frac{e^2}{4\pi\epsilon_0} \frac{Z_l}{|r_i - R_l|} + \frac{1}{2} \sum_{ij} \frac{e^2}{4\pi\epsilon_0} \frac{1}{|r_i - r_j|} \tag{3.3}$$

where the first and second terms are just kinetic and potential energy of the electrons and the thrid term is the interaction among electrons. This model assumes the lattice (ions) does not move and only consider the electron motion. Though it seems simple at the

first glance, the thrid interaction term makes this model in general unsolvable. Hence in order to calculate any experimentally measurable physical quantities, approximations that simplify the last term must be made. One of the most successful method is to replace the interaction term with a time averaged local electron density[60], which is called the Local Density Approximation (LDA). This method reduces the original many-body problem into a single-body solvable one that works pretty well for non/weakly-correlated systems like metal, semiconductor. However this method still fails when it comes to strong-correlated materials. An improvment of this method is to treat the lattice as slowly moving instead of totally static, which yields the Born-Oppenheimer Approximation [61]. Yet this method continues to perform poorly when dealing with strong-correlated materials.

One of the reason that these approaches not working on materials with strong correlation is no matter what they do to simplify the interaction, they still treat each electron as free electron that is independent of others. When the electron-electron interaction is strong as it is in the case of Mott-insulators, these methods are bound to fail and a new model is in need. One of the most simple yet successful model proposed by Hubbard in 1963 [62] is the single-band Hubbard model as listed below:

$$H_{\text{Hubbard}} = \sum_{\langle i \neq j \rangle \sigma} t_{ij} c^{\dagger}_{i\sigma} c_{j\sigma} + U \sum_{i} n_{i\uparrow} n_{i\downarrow} \tag{3.4}$$

where ij denotes sites, σ denotes spin and $c^{\dagger}$ and c denote the creation and annihilation operators, and $n_i = c^{\dagger}_i c_i$ is the number operator. The first term describes the process of one electron "hopping" from one site to another, characterized by the energy cost t_{ij} known as the hopping integral. In the most simple model only hopping between nearest neighbors is allowed so the t_{ij} reduces to t. The second term describes the case where 2 electrons occupy the same lattice site, with the energy cost of U due to Coulomb repulsion. And as one could see in this model only one band is taken into consideration. (in another word, the hopping between different bands are not considered). In principal this single-band model only works for the materials of which the outermost obrbital is s orbital. In reality since many materials only have one band or multiple bands hyperdized as one near the Fermi surface, this simple model still works very well on explaining the underlying physics.

Solving this model with different parameters yield a variety of distinguished states[13],

which are mainly determined by the comparison between the on-site energy U and the bandwith W. As shown in Fig. 3.20, we start with a normal metal that has a half-filled band and the Fermi Surface sits in the middle of the non-interacting band (Fig. 3.20 (a)). As the inteaction between electrons goes slightly stronger (Fig. 3.20 (b)), the electrons can be described as quasiparticles whose DOS still resembles free electrons. The Fermi liquid model accounts for the narrowing of the peak. When the interaction goes even stronger (Fig. 3.20 (c)), the electrons show a mixed behavior of the Hubbard bands (2 peaks away from the Fermi surface) and a quasiparticle peak pinched at the Fermi level. Finally when the interaction is strong enough (Fig.3.20 (d)), the Mott-insulator emerges as the band fully splits into 2 Hubbard bands and the Fermi surface is left between these 2 bands. This process describes a family of insulators that are believed to be metal by traditional band theory. These materials were first discovered by Jan Hendrik de Boer and Evert Johannes Willem Verwey in 1937[63] and later explained by Nevill Mott, who the material is named after, and Rudolf Peierls in the same year[64].

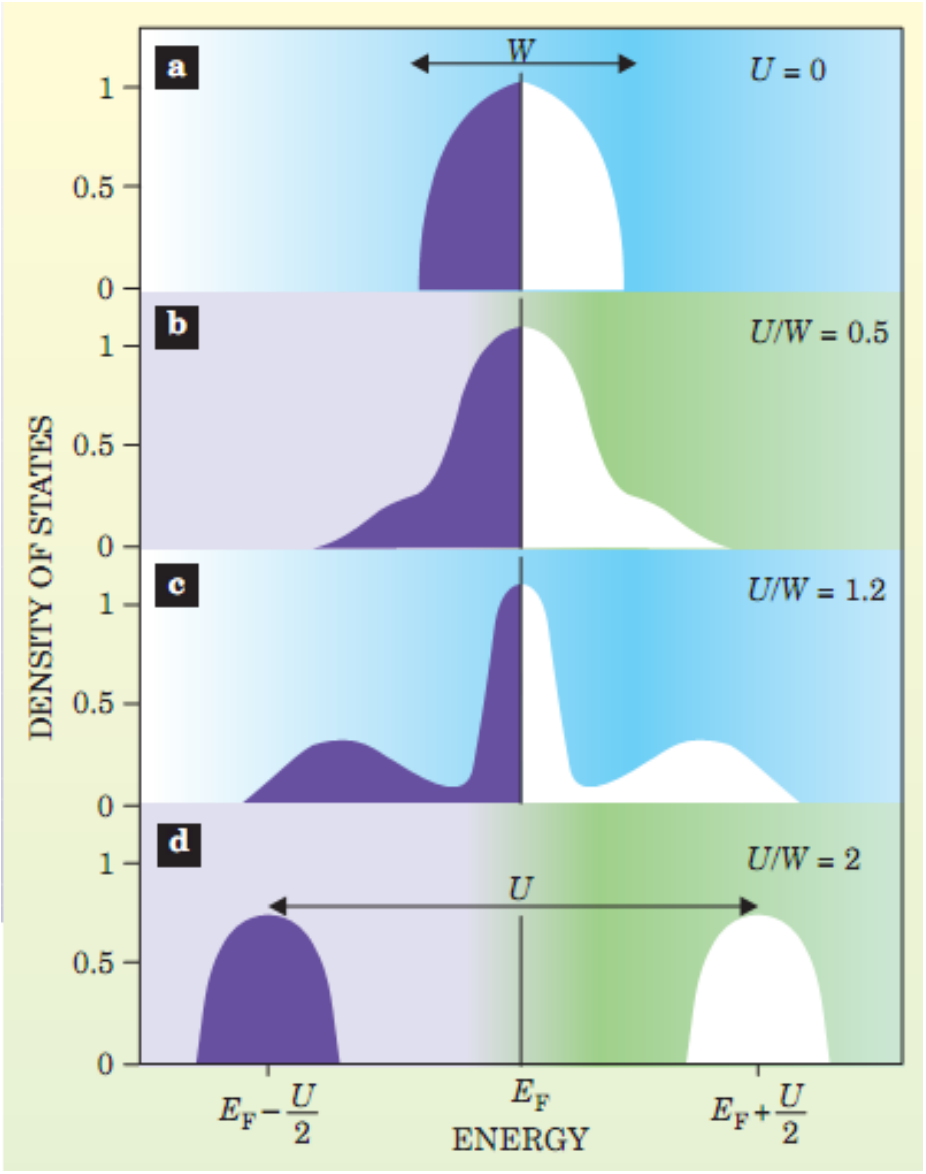

Figure 3.20: The Density of States of the single-band Hubbard Model at different scenarios [13]

Now we moves back to the case of Ca_2RuO_4. As we explained before, the outermost electrons of the Ru atom is 4 $4d$ electrons. Due to the crystal field splitting (Section. 3.3.1) and Jahn-Teller effect (Section. 3.3.2), the degeneracy of the orbitals in the $4d$ shells are lifted. At room temperature, the 4 electrons all sit in the lower-energy t_{2g} orbitals, forming a fully occupied d_{xy} band and a half occupied $d_{xz} - d_{yz}$ complex. Due to the locality of the

$4d$ orbitals, there is sufficient enough interaction among these electrons, hence results in a Mott-insulator in room temperature. Since originated from the crystal structure, this Mott physics plays a significant role in the phase transition of Ca_2RuO_4 as it is accompanied by a first-order lattice distortion.

In summary, this simple but quite effective model captures most of the essential factors in strongly correlated materials. Not only does it explains the transition between metal and insulator, but also it can interpret the long range magnetic orders observed in some systems.[65] Still as most of theoretical models, it is not perfect as in reality generally there are way more different phases competing simultaneously in strong-correlation materials, which are not taken into consideration in the single-band Hubbard Model.

3.3.4 Orbital Degree of Freedom

The single-band Hubbard Model does not take different orbitals into consideration, which in the case of Ca_2RuO_4 might barely be true. At room temperature, though highly degenerate, the electron still has the freedom to occupy any of the d_{xz} and d_{yz} orbitals. Hence this degree of freedom and the interaction between the 2 orbitals need to be taken into consideration. Here we present a short summary of theory dealing with these orbital degrees of freedom, which when cooupling with each other and other degrees of freedom makes the ruthenates and even TMO exceedingly intriguing.

As introduced above, the d_{xz}/d_{yz} complex is normally doubly degenerate. The electrons are free to choose any orbitals to stay or some linear combination of the two. One could see that this is very similar to the spin degree of freedom. Therefore one straightforward way to deal with these orbitals is to introduce a pseudo-spin operator T[66**?**]. The formalism of this pseudo-spin operator/states is just the same with a normal spin operator/states, with one orbital being the "spin-up" state and the other being "spin-down".

Now we move to the interaction between these orbitals. Although energy-wise the d_{xz} and d_{yz} orbitals are the same hence considered as degenerate, spatially they are still different. Therefore the intra-orbital and inter-orbital electron-electron interaction will also be different. Also this allows the electron hopping from one orbtial to another. Thus the

new hopping (kinetic) and interaction term of the 2 bands Mott-Hubbard model is:

$$\begin{aligned} H_{\text{hopping}} &= \sum_{ij\gamma\gamma'\sigma} t_{ij} c^{\dagger}_{i\gamma\sigma} c_{j\gamma'\sigma} \\ H_{\text{interaction}} &= \sum_{i\gamma\gamma'} U_{\gamma\gamma'} n_{i\gamma} n_{i\gamma'} \end{aligned} \tag{3.5}$$

where the i, j denotes the sites (hopping between i and j is allowed by the model), γ denotes the orbitals and σ is the spin as usual. The rest terms shares the same meaing with the single-band Mott-Hubbard model introduced before. At a glacne this seems to already take everything into consideration. However another type of interaction between orbitals also contribute a lot to the electron behavior. This is the inter-orbital exchange interation shown as below:

$$H_{\text{exchange}} = \sum_{i\gamma\gamma'\sigma} J c^{\dagger}_{i\gamma\sigma} c^{\dagger}_{i\gamma'\sigma'} c_{i\gamma\sigma'} c_{i\gamma'\sigma} \tag{3.6}$$

where the meaning of the terms are the same with before. This interaction indicates a pair of electrons sitting at different orbitals exchanging their spins. Similarly it is also possible that the same pair of electrons switch the orbitals, i.e, a pair-hopping. This is described by the Hamiltonian below:

$$H_{\text{pair-hopping}} = \sum_{i\gamma\gamma'\sigma} J' c^{\dagger}_{i\gamma\sigma} c^{\dagger}_{i\gamma\sigma'} c_{i\gamma'\sigma'} c_{i\gamma'\sigma} \tag{3.7}$$

In reality all these orbital degrees of freedom are all present and coupling with each other and other degrees of freedom (for instance, lattice or spin), giving birth of a variety of novel phenomena. The overall coupling could be very complicated and hard to understang. Here we just introduce 2 types of coupling that are relatively easy to explain.

The first coupling is between orbitals and the lattcie degree of freedom. This has been observed in ruthenates and is believed by some to be the source of the CMR[67, 26, 68]. Such coupling can be easily represented by introducing the pseudo-spin operators for orbitals[57]:

$$H_{\text{orbital-lattice}} = \sum_{i\gamma l} g_{\gamma l} T_{i\gamma} Q_{il} \tag{3.8}$$

where the T is the pseudo-spin operator and the Q is the lattice distortion. The γ is for orbitals and the l is for lattice distortion modes. Another type of coupling is between the

orbitals and spins, i.e. the famoust Spin-Orbit coupling (SO coupling). The SO coupling is of highly importance in many areas in physics and chemistry, leading to a wide variety of phenomena including the Zeeman splitting[69], the Larmor precession[70] and spin-Hall effect[71]. Such effect has also been observed in ruthenates, which greatly affect the orbital ordreing and magnetic properties[72]. This interaction has the general form:

$$H_{\mathrm{SO}} = \sum_{i,j} [J_s S_i \cdot S_j + f(T_i, T_j) + g(T_i, T_j) S_i \cdot S_j] \tag{3.9}$$

where the J_s is the spin constant, the $f(T_i, T_j)$ is the orbital constant and the $g(T_i, T_j)$ is the spin-orbital constant controlling the interaction amplitude. As one could see, these 2 coupling are the just 2 of the most straightforward ones and more complex coupling among all these degrees of freedom can exsit.

Before we end this seciton, it is worthy to mention another orbital related effect, the orbital hybridization. The orbital hybridization was discovered by Linus Pauling in 1931[**?**]. It is the process of mixing several orbitals into a new hybrid one that is more suitable for the pairing electrons to form chemical bonds. The fundamental reason behind this mixture of orbitals is the new one has lower energy than the separated old ones.

In order to see how orbital hybridization affect the property of Ca_2RuO4, we need to understand how orbitals affect the bandwidth. In most TMO, the bandwidth is largely determined by the overlap of d-orbitals of adjacent metal cations. Besides, the direct overlap, the indirect exchange of electrons through the briding oxygen p-orbitals also makes an impact. Therefore in total the bandwith is determined by the hyperdized orbital of the transition metal d-orbitals and p-orbitals. This is very evident in heavy transition metal bearing materials, because of the smaller distance between the d-orbitals and the oxygen p_σ orbitals[73]. In light TMO, the hybridization can also be found. For example, in cuprates the copper $3d_{x^2-y^2}$ orbital is very close to the oxygen $2p_sigma$ orbital, therefore can be hybridized. Another example is ruthenates, in which the related oxygen orbital is the p_π orbital. These 2 scenarios are shown in Fig. 3.21.

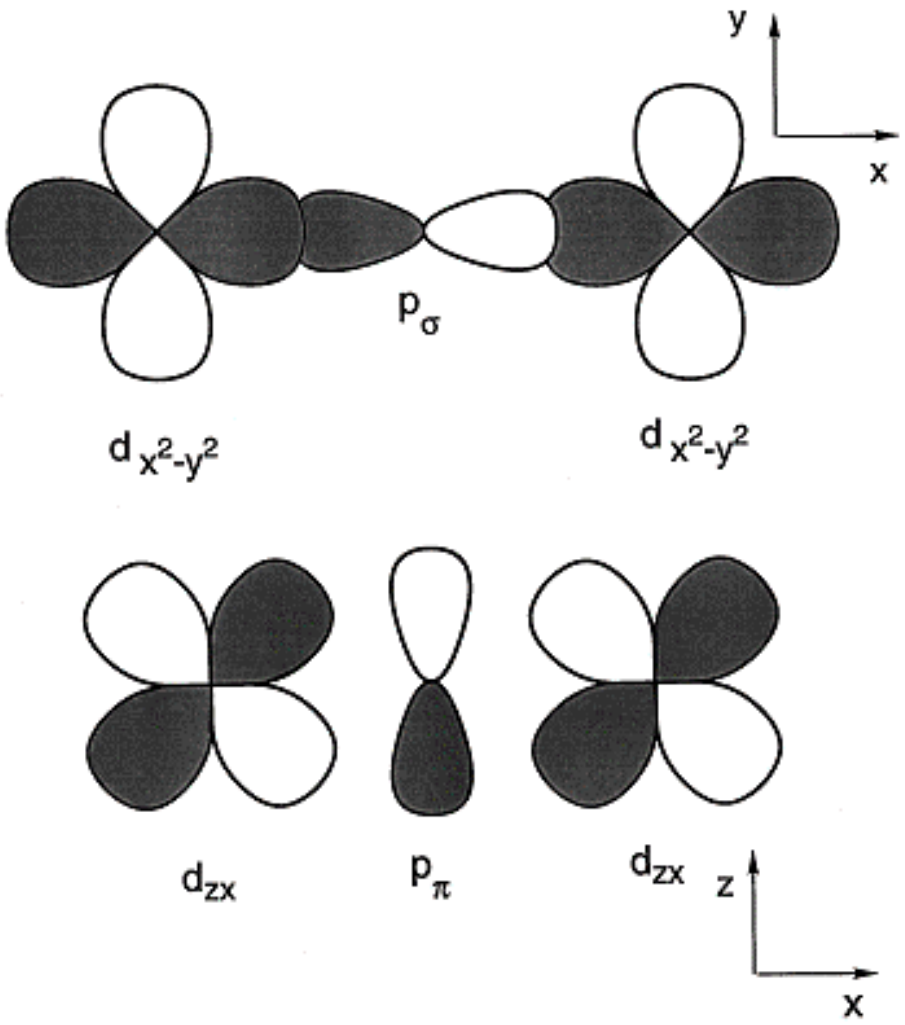

Figure 3.21: The 2 cases of $p-d$ hybridization [14]

When taking the electron-electron interaction U into consideratoin, this hybridizaiton can result in a more intriguing phenomenon. The energy difference between the d and p orbitals is refered as the charge transfer energy Δ. If this energy is larger than the interaction U, then after the Mott transition, the lower Hubbard band still has higher energy than the band of the other orbital. Hence in this case the material is just a normal Mott-insulator. In the other case where the interaction U is stronger, the lower Hubbard band will be even lower than the band of the other orbital. Hence the charge gap is determined by the upper Hubbard band the the band of the orbital with higher energy, forming a charge transfer

insulator. These 2 cases are shown in Fig. 3.22.

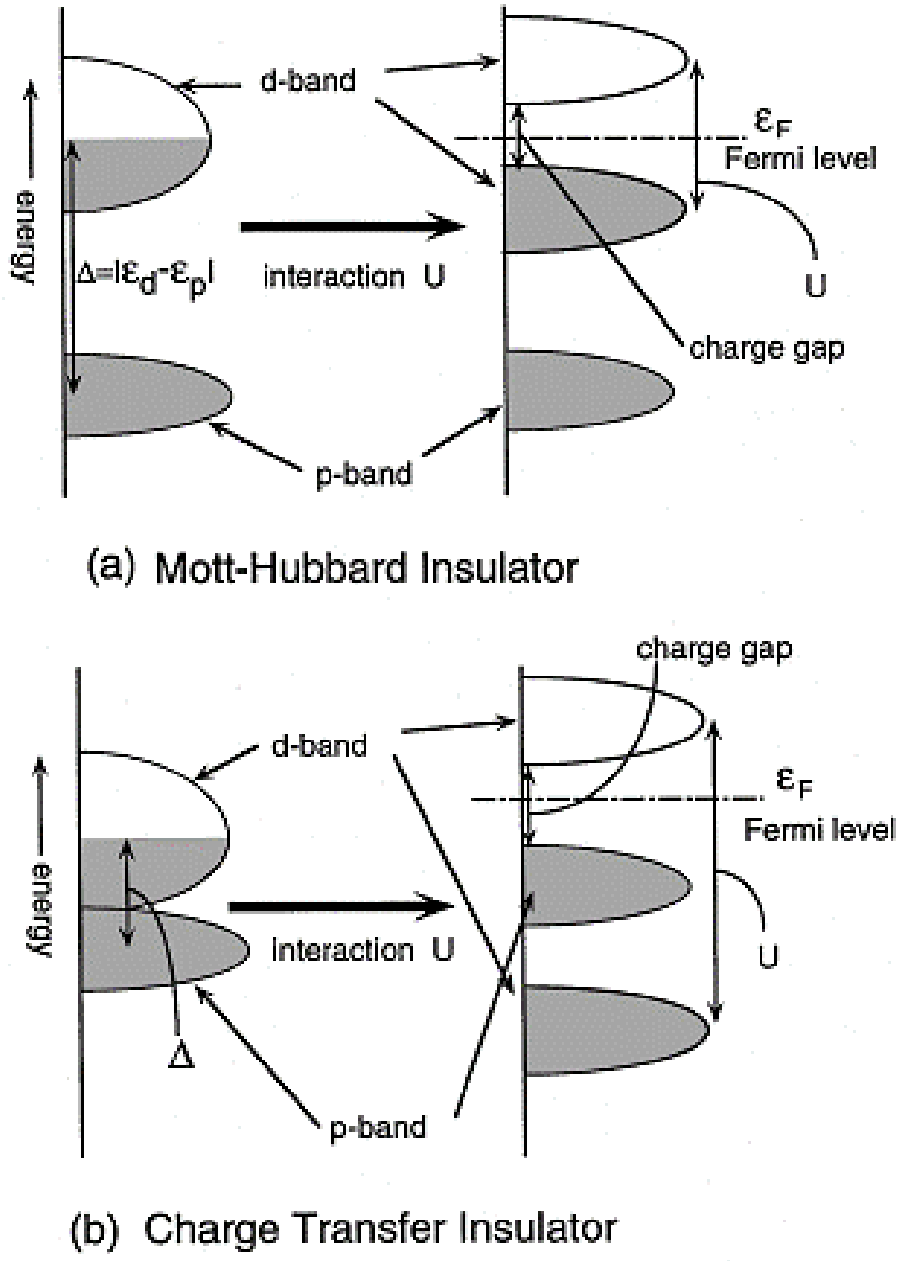

Figure 3.22: The 2 cases of insulators involving the charge transfer energy Δ and the Coulomb interaction U [14]

In the case of Ca_2RuO_4, the interaction is not too strong so it is an ordinary Mott-insulator in room temperature[74, 75]. Besides the orbital hybridization, there are several

other orbital-related effects like superexchange interaction which are also present in ruthenates. Due to the limited space these effects are not introduced in this thesis.

3.3.5 Introduction to DMFT

The traditional band theory methods like DFT[76, 77], LDA[60] work pretty well on free electron systems, in which essentially the problem is a single-particle one. As mentioned above, these methods in general will break down when strong particle-particle interaction is introduced. This becomes extremely evident when many degrees of freedom are entangled in a system causing different phases competing with each other. The first such case is the High-Tc superconductor, which opens the door of study over strong-correlated systems. In order to properly handle the complex Hamiltonian representing these strongly correlated materials, a new method later known as Dynamic Mean Field Theory (DMFT) was developed by Vollhart and Metzner[78] and Gerorge and Kotliar[79].

The method gets its name from its similarity with Mean Field Theory (MFT) and difference from tradtional static MFT that it allows local fluctuation of the field in time (i.e. dynamic). It is ideal for the study of strongly correlated systems as it does not distinguish teh particle-like excitations and the wave-like excitations. Also unlike previous methods like DFT, which to some extent are just twisted forms of perturbation theory, from the very beginning DMFT does not make assumptions that the interaction needs to be weak. In short, the fundamental idea of DMFT is to covert a many-body problem with many degrees of freedom into a effective single site problem. In this conversion, the degrees of freedom is reduced hence the Hamiltonian becomes more easy to solve. For instance, the single-band Hubbard Model has the following Hamiltonian:

$$H_{\text{Hubbard}} = t \sum_{\langle ij \rangle \sigma} c^{\dagger}_{i\sigma} c_{j\sigma} + U \sum_{i} n_{i\uparrow} n_{i\downarrow} \tag{3.10}$$

where ij denotes sites, σ denotes spin and $c^{\dagger}$ and c denote the creation and annihilation operators, and $n_i = c^{\dagger}_i c_i$ is the number operator. Such model is in general intractable using pertubation-based methods. Instead, DMFT maps this model to the Anderson Impurity Model (AIM)[79, 80], which describes the interaction of the impurity (one site) with a

"bath" of energy levels:

$$H_{\mathrm{AIM}} = \underbrace{\sum_{p} \epsilon_p a_p^\dagger a_p}_{H_{\mathrm{bath}}} + \underbrace{\sum_{p\sigma} V_p^\sigma c_\sigma^\dagger a_{p\sigma} + h.c.}_{H_{\mathrm{mix}}} + \underbrace{U n_\uparrow n_\downarrow - \mu(n_\uparrow + n_\downarrow)}_{H_{\mathrm{loc}}} \tag{3.11}$$

where H_{bath} is the non-correlated electronic levels of the bath, H_{mix} is the coupling between the impurity and the bath through the hybridization $V_p^\dagger$, and the H_{loc} is the impurity characterized by onsite energy U. Once this mapping is done, the AIM model can be solved by several well-studied methods including Wilson's renormalization group[81] and the Quantum Monte Carlo method[82]. The detailed solving process involves a self-consistency DMFT loop, in which the these solvers output the impurity Green's Function and self-energy Σ_{imp}, which is agian used as the input for the next iteration of the loop. The details of the DMFT loop is listed in Fig. 3.23:

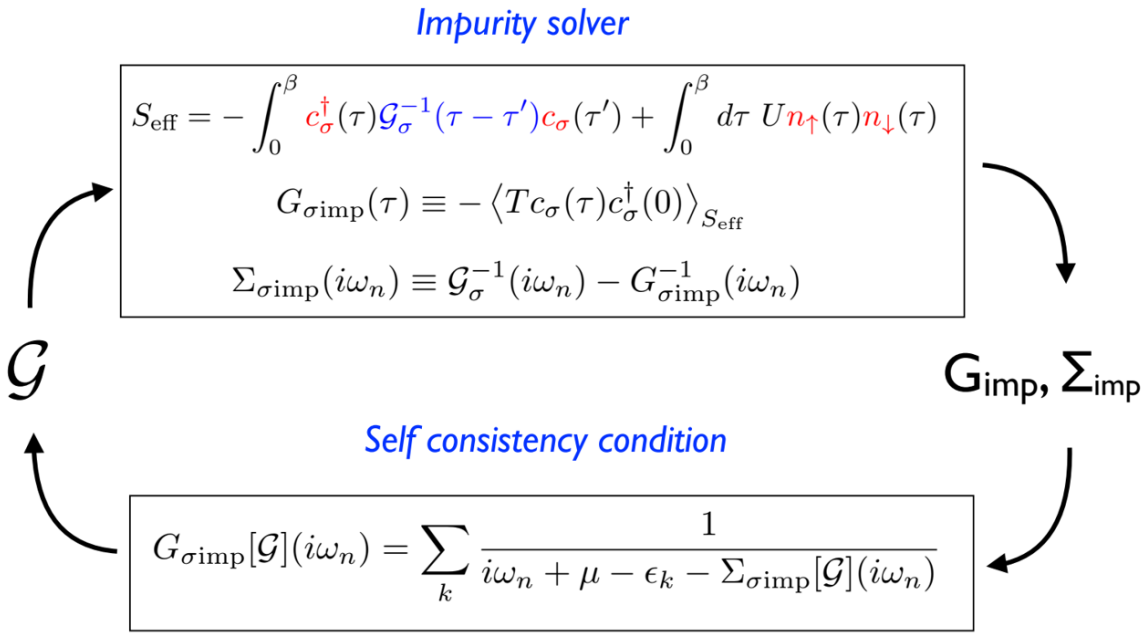

Figure 3.23: The sefl-consistent dmft loop [15]

As an advanced theory, a detailed understanding of DMFT is not in the scope of this thesis since it requires a comprehensive study that takes years. For more information about DMFT, please check [83, 84].

Chapter 4

Experimental setup

A good experimental setup is of apparent significance of successful experiments. In this chapter we present how we setup the core equipment (STM), the temperature control system (LH cooling with close loop recovery system) and the necessary prepartion to make a measurable sample.

4.1 STM Setup

As discussed in previous chapter, since it measures extremely small values, the STM is very sensitive to all kinds of external influence, including both mechanical noise (vibration) and electronic noise. In reality these noise will always affect the measurement to a certain extent, no matter what procedures taken. Still in order to eliminate the effect of these noise, we applied the following procedures.

The most common noise in STM experiments is the mechanical one steming from vibration. For the intrinsic vibrations, there is typically very lillte one could do as they are simply intrinsic propterties of the material/structure. Still we can try to supress such motion with an efficient damping system. On the bottom of the STM scanning stage is a magnets, which will act like a damper since once there is relative motion, it will create an Ampere force that fights with this motion. The vibration comes from both the instrinsic modes of the STM structure and external sources like moving objects (pumps, human and even wind, etc.). To isolate most external vibrations, our STM is located at an acoustic anechoic chamber. The

wall of the chamber is made of sound-absorbing materials that greatly reduces vibration in and out of the room. Inside this anechoic chamer is only the STM and necessary accessories (optical table, LH dewar and transfer/recovery line). The control system of the STM sits outside the room, so there will be very little vibration translated from normal operations. Furthermore, the whoe STM is put on top of an optical table, which is heavy and supported by 4 piston legs. Each leg is supported by compressed air, hence levitated from the ground. This also highly suppress the external vibration. All wires are also anchored with this table so that they will not carry much vibration, either.Lastly, as discussed before, the STM scanning stage is suspended by 3 springs that form a low-pass filter (typicall the cut-off frequency is only a few Hz) for all vibrations. All of the 3 vibration-isolation system plus the magnets mentioned above form a exceedingly well-performed barrier that protects the system from mechanical noise.

With vibration isolated and damped, now it comes to the electric noise. The tunneling current under ordianary working condition is about a few pA to 1 nA, which is extremely small compared to other signals typically obtained in experimenrts. Therefore it is also crucial to properly deal with electric noise. For a start, all cables outside the STM UHV chamber are coaxial cables that by design screen external signals. Inside the STM chamber, due to the requirement of UHV, it is feasible to keep using coaxial cables. However, since all the radiation shields are grounded, we put most of the wires inside the shields, which act like a screening layer, too. Only very minimal amount of the wires (the part connecting the plug and the wire-feedthrough on the outer radiation shield) are exposed to external electromagnetic interference. Also special attention is paid on the grounding quality. Multiple thick copper plates are carefully connected to ground, so that the total resistance from ground to the grounding point on the STM is negligible.

4.2 Temperature Control System

Temperature countrol is a very important aspect of our experiment, as we need to both vary to the temperature to put the material at different phases, and to stablize the temperature while taking measurements. In our setup, we use a resisitive heater and liquid helium to

establish temperature equilibrium. Both the heater and the LH flow are firmly attached with the cold finger, which thermally anchors the rest of the STM, including the inner and outer radition shield.

As described in the previous section, our variable temperature STM ulitizes liquid helium as coolant. A typical setup of low-temperature STM conprises a stationary cyrostat that sits on top of the STM. Such configuration has been widely used in many commercial and custom STM, as shown in Fig. 4.1. With a LH dewar (and typically a LN jacket surrounding it to minimize boil-off lost), it is very easy to reach the base temperature around 4.2K and maintain the system stable at such temperature. And with various mechanical connection system to control the cooling power, the base temperature can vary within a small range, which enables a limited temperature varying ability. One of the drawbacks of such system is due to the large volume of the cryostat, the system is typically quite heavy and big, thus difficult for hardware update or maintenance. Furthermore, even with a heater, its temperature varying range is still very limited at relatively low temperature range, which makes such system not ideal on inverstigation that covers a wide temeperature range (as in Ca_2RuO_4). Last but not least, such system in general is a stand-alone system, which does not recover the valuable helium used. Therefore special design and fabrication is needed for such cyrostat to minimize the helium comsumption rate, which further increases its weight and volume.

To deal with these disadvantages, here we introduce another type of system that does not have a stationary cryostat but uses constant liquid helium flow to cool down the system. The basic setup is shown in Fig. 4.2. The LH is stored in a movable ultra-low-loss dewar, and is transferred through a transfer line into the STM. Due to the boil-off and the heat transfered while inserting the transfer line, the LH dewar is pressurized hence powers the LH flow. After cooling the STM, the liquid helium is vaporized. In traditional systems, here is the part where the used helium goes to the atomsphere wasted. In our system, in order to further reduce helium loss, we attach a recovery system to the exhaust of the STM. Additionally, although the boil-off loss of the dewar is pretty low, still there will be some amout of helium vaporized due to intrinsic heating. Thus we collect those helium as well. All the helium gas is then pushed into a liquefier (Fig. 4.3) that liuquefy helium gas back

Figure 4.1: A commercial STM from Omicron. The giant cylinder on top is the liquid nitrogen and liquid helium cryostat.

to the liquid. Apparently the compressor of the liquefier creates lots of vibration, so the liquefier is located at another room one floor up the STM room. Once the heliqum level in the movable dewar is low, we move it to the room of the liquefier and transfers the LH back into the dewar. This forms a close-loop recycle of the helium and greatly redcues the exprimental cost.

As one could imagine, a constant flow rate of the LH is vital to the temperature control, so here we discuss how the LH flor rate is controlled. In Fig. 4.2, it is clear that the pressure difference between the dewar and the exhaust end of the STM controls the LH feeding speed. Given everything else stays unchanged, if the pressure difference is constant, so will the LH flow rate. Therefore we need to carefully control the pressure on both ends. In our setup, we applied 2 commercial pressure controllers (Alicat PC-15PSIG-D/5P, 5IN , Fig. 4.4).

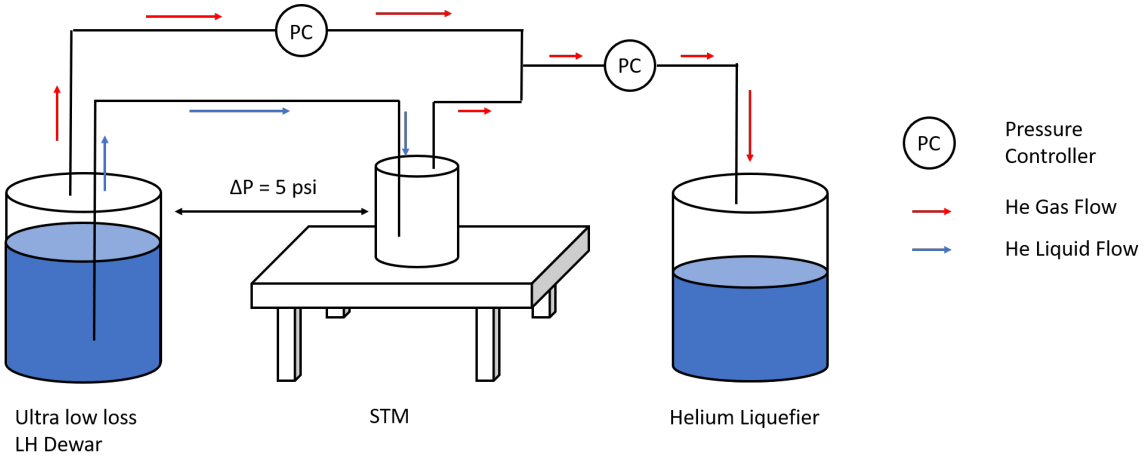

Figure 4.2: The demonstration of the liquid helium feed and recovery loop

The pressure controller we used essentially is an automatic valve that opearates based on the real pressure (w.r.t atompsphere) it measures and it can be configured to control either the front or the back pressure. For instance, if one needs to control the back pressure, the vavle by default is closed, and will open once the back pressure is higher than the set point. In our system, one pressure controller is used to controll the pressure inside the dewar, and another one is used to controll the pressure insdie the recovery line. With these 2 device, we can achieve a constant differential pressure between the dewar and the STM (typically 5psi), and a constant pressure inside the transfer line (typically 0 psi). The reason that the pressure inside the line also needs to be controlled is the liquefier will act like a pump and lower the pressure inside the line, hence create unstable differential pressure. Also it is good to keep the pressure inside the line equal to atomsphere to prevent potential leakage. Beside the pressure control, a needle valve on the transfer line also contribues to the flow rate control.

With the LH flow properlly controlled, a constant cooling power is obtained. So the rest of the temperature control comes to the heating power. In our system, we use a commercial temperature controller (Cryocon 32B Temperature Controller) which applies PID control approach to control the heating power. PID stands for proportional–integral–derivative, which is a widely used control technique in a variety of areas. This algorithm take all

three factors into consideration: the difference between current value and the target value (proportional), the past history (integral), and the speed of value changing (derivative). With paramters properly set, PID controller is exceedingly capable of keeping the value stable at the target. For more details about PID please check referrence[85].

With everything attached, the system is shown in Fig. 4.5. The blue dewar on the left is the movable ultra-low-loss dewar. The helium inside is transferred through the transfer line into the stm, which sits on a air-table to damp vibration. The helium gas is collected by the copper lines on the wall, then goes to the liquefier that locates in another room one floor up.

4.3 Sample Preparation

As we will see in the following section, unlike ordinary STM measurements, our investigation on the current driven behavior of Ca_2RuO_4 that involves both the source current and the tunneling current takes special preparation. Therefore here we present how to properly set up the sample as well as the STM and other necessary equipment to perform such experiment.

A typical STM sample is shown in Fig. 4.6. A crystal is glued by conducting paste on a metal (Ti/Fe) sample holer. The sample holder is placed in the slot of the scanning stage (as shown in Fig.4.7), which has spring contacts for bias voltage and other purposes like gate or source current. In our STM, there are 1 bias contact (the central big one) and 4 stage contacts (the top 4 small ones). For a normal sample holder, it will make contact with all the contacts (hence shorting all of them) as it only needs to recieve the bias voltage. Such setup is used in the measuremnt purely related with temperature driven phase transition in our experiment. However as discussed above, when it comes to current driven measurement, there willl be more than one current involved hence we will need more than one contact. This reqiurement is met with a multi-contact sample holer, which has 4 independent contacts designed to work with the 4 stage contacts on the scanning stage. In our experiment, we use 2 of these contacts to run current through the crystal.

To fabricate a scannable sample, we first glue a silcon chip with a UHV-safe expoxy called

Torr Seal (Loctite EA 1C) on the mullti-contact sample holder as it helps to approach the crystal due to the fact that it is very reflective. Then 2 small sapphire plates are guled next to each other with Torr Seal on the silicon chip, to prevent possible shorting with the chip (Normally the chip itself is covered with an insulating SiO_2 layer. But this layer can get damged over time of use.). After this step, a Ca_2RuO_4 crystal is carefully selected and glued on the middle of the 2 sapphire plates. This is to make sure each end of the crystal will be solely laid on one sapphire plate, so that when contacts are put on there will be no shorts. After curing at about 70°C for 30 minutes, the crystal is firmly mounted and contacts can be put on. A fast-curing silver expoxy is used at this step, as they are really easy to apply and cure. 2 droplets of such epoxy is carefully placed at the 2 ends of the crystal, covering a tiny part on each end and extending out a small distance. After curing at room termperature for 5 minutes, these contacts are ready to be used. Hence we put a wire on each contact and apply the same silver epoxy to secure the connections. The other end of the wire is firmly attached to the contact on the sample holder with a metal nut. In the end, a post made from metal wires is glued with Torr Seal on top of the crystal. This is for the in-situ cleaving later inside the STM chamber, which creates a clean flat surface that is ideal for STM to investigate. After all the steps, a finished sample is shown in Fig. 4.8.

When conducting current driven measurement, the current is sourced by a YOKOGAWA GS200 DC VOLTAGE/CURRENT SOURCE or a KEITHLEY 2400 SourceMeter. Typically the YOKOGAWA meter features less noise, so it is used when taking STM measurements. While the KEITHLEY one is more noisy, it is able to measure both current and voltage at the same time. So it is used to take the initial transport chracterization of a crystal before taking STM measurement. The details of how to perform current driven measurment is discussed in Chapter. 6.

Figure 4.3: The liquefier built by Cryo Industry used in our LH recovery loop. The blue part is the dewar holding liquid helium. The silver part on the top is the cold-head made by Sumitomo Hevay Industries. The cold head is connected by 2 helium lines to the compressor, which cools down the cold head and hence the helium gas. The helium recovery line is connected to the dewar through a pressure control valve (green one). The whole liquefier and the compresso is located at another room to isolate the vibrations.

Figure 4.4: The pressure controller used in our system. The current configuration is to control the front pressure. The black cylinder on the left is the vavle unit. The silver part with the word "flow" is the pressure gauge unit.

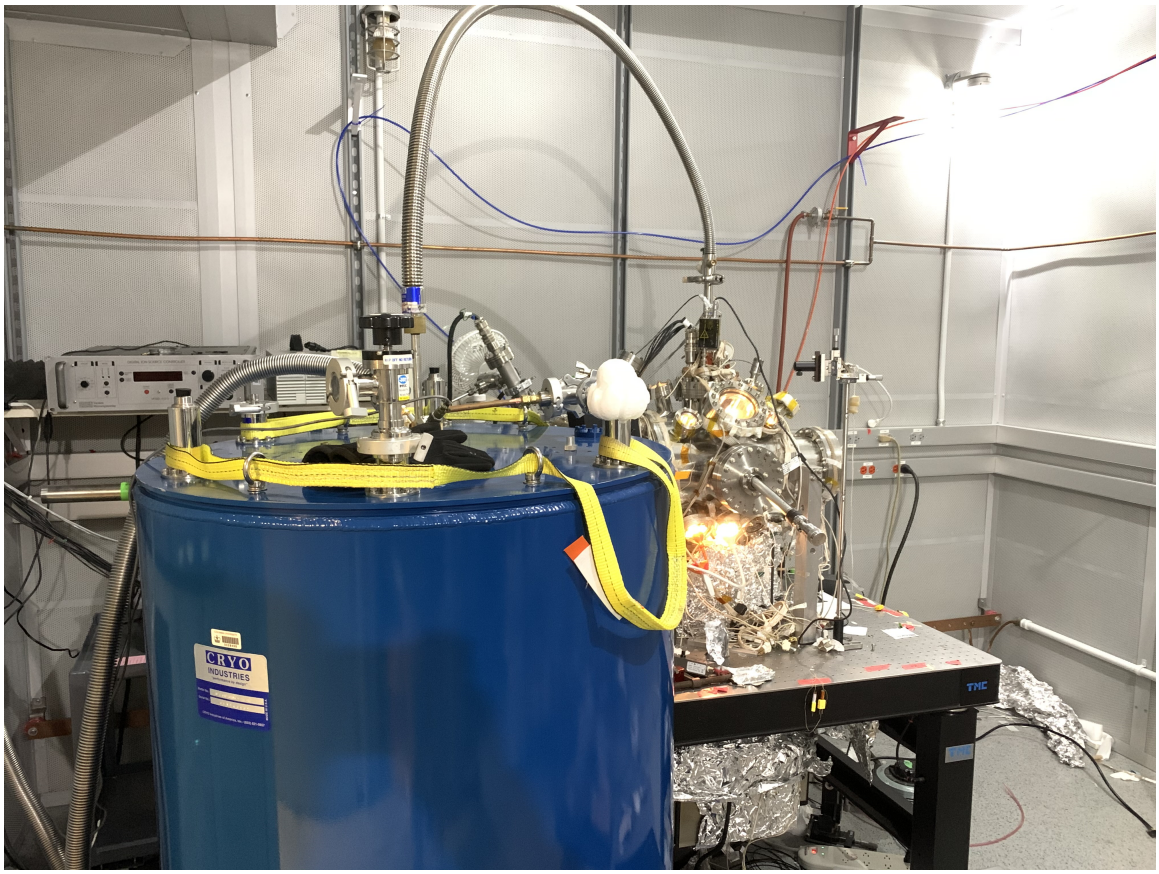

Figure 4.5: The VT-STM. The blue dewar on the left is the ultra-low-loss dewar. It is connected to the STM through the transfer line. The helium gas is collected by the copper line on the wall, which connects to the liquefier one floor up.

Figure 4.6: A typical STM sample. The black crystal in the middle is glued by conducting silver expoy (EPO-TEK H20E) on the sample holder.

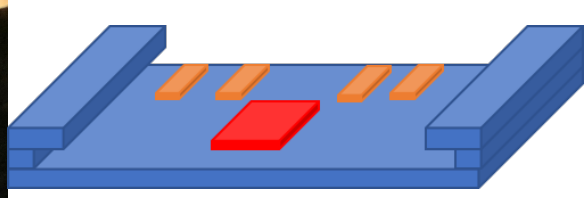

Figure 4.7: Schematic cartoon of the STM scanning stage. The central big red contact is for STM bias voltage. The rest 4 orange ones are for contacts connected to multi-contact sample holder.

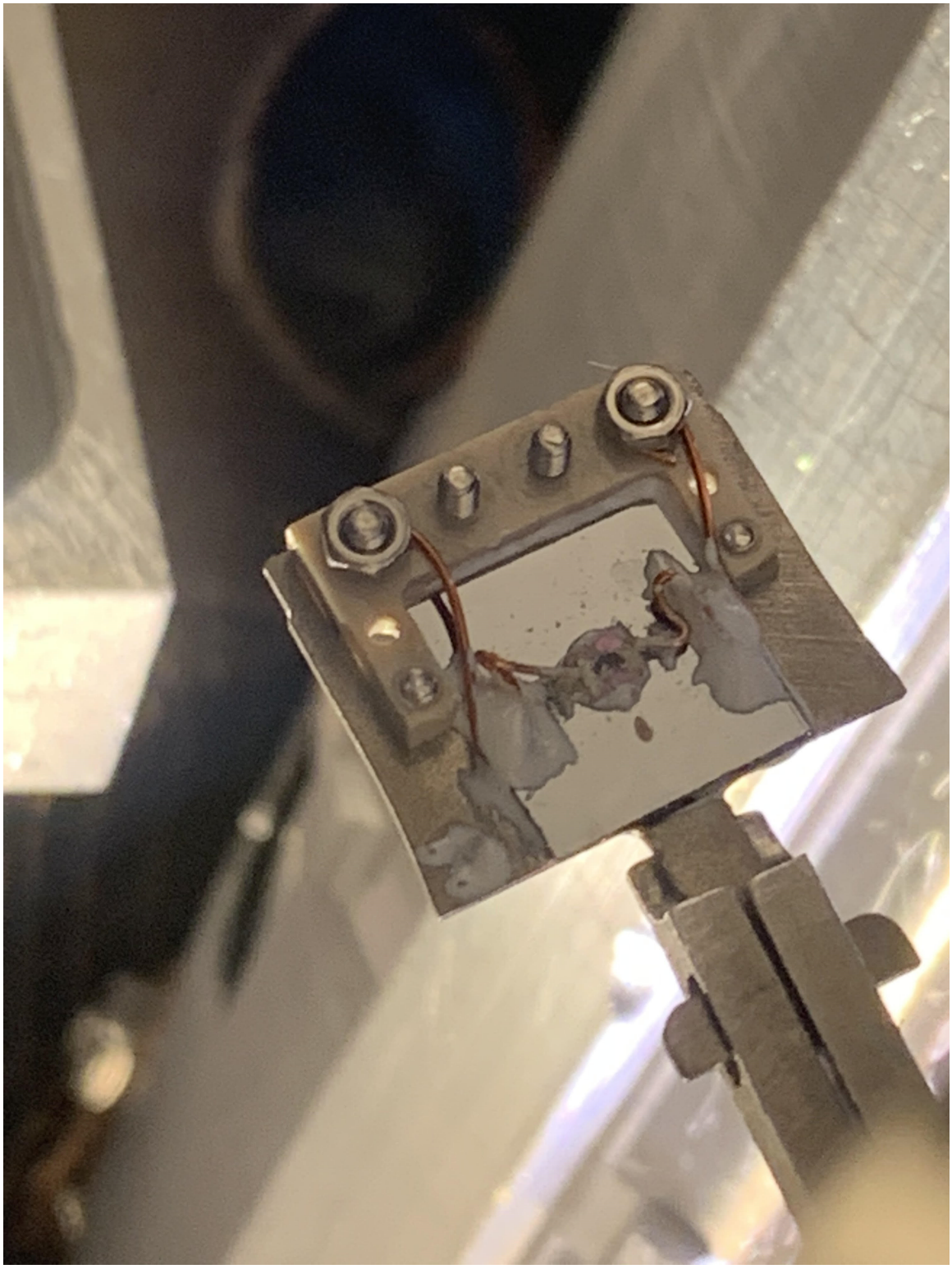

Figure 4.8: A Ca_2RuO_4 sample for current driven measurement in the STM chamber. The crystal is the black part in the middle, which is connected by the silver expoxy to the wires. The wires are connected to the contacts on left and right, secured by 2 nuts pressing down.

Chapter 5

Temperature Driven Phase Transition

The high-temperature metal phase and the high-current metal phase in Ca_2RuO_4 long has been puzzling researchers. The key question that needs to be answered is whether they are fundamentally different. In order to answer this, one needs to characterize both phases properly. Here we summarize our results on STM measurement taken at different temperatures without applying sourcing current. This not only verify the quality of the crystals used in the experiment, but also sets a solid fundation of studying current driven phase transition and the comparison between these 2 transitions.

5.1 Topography of Ca_2RuO_4

The sample used in STM measurements are described in Chapter 4. The starting point of pretty much every STM study is the surface topography with atomic resolution. The topography image shows both the structure of the material and the electronic property as essentially STM probes the local electron density of states. Hence here we present our topography images of the cleaved suface of Ca_2RuO_4 crystals.

The unit cell of Ca_2RuO_4 is shown in Fig. 5.1. As mentioned before, the unit cell is characterized by the rotation and tilting of the RuO_6 octahedra. In order to get a atomically resolved topography image, the surface of the crystal must be exceedingly flat and clean.

The raw surfaces do not meet such criteria as both the flatness and the cleanliness can not be guaranteed. Thus typically the crystal needs to be cleaved in-situ before STM measurement. The position of the cleave is indicated by the blue arrows in Fig. 5.1.

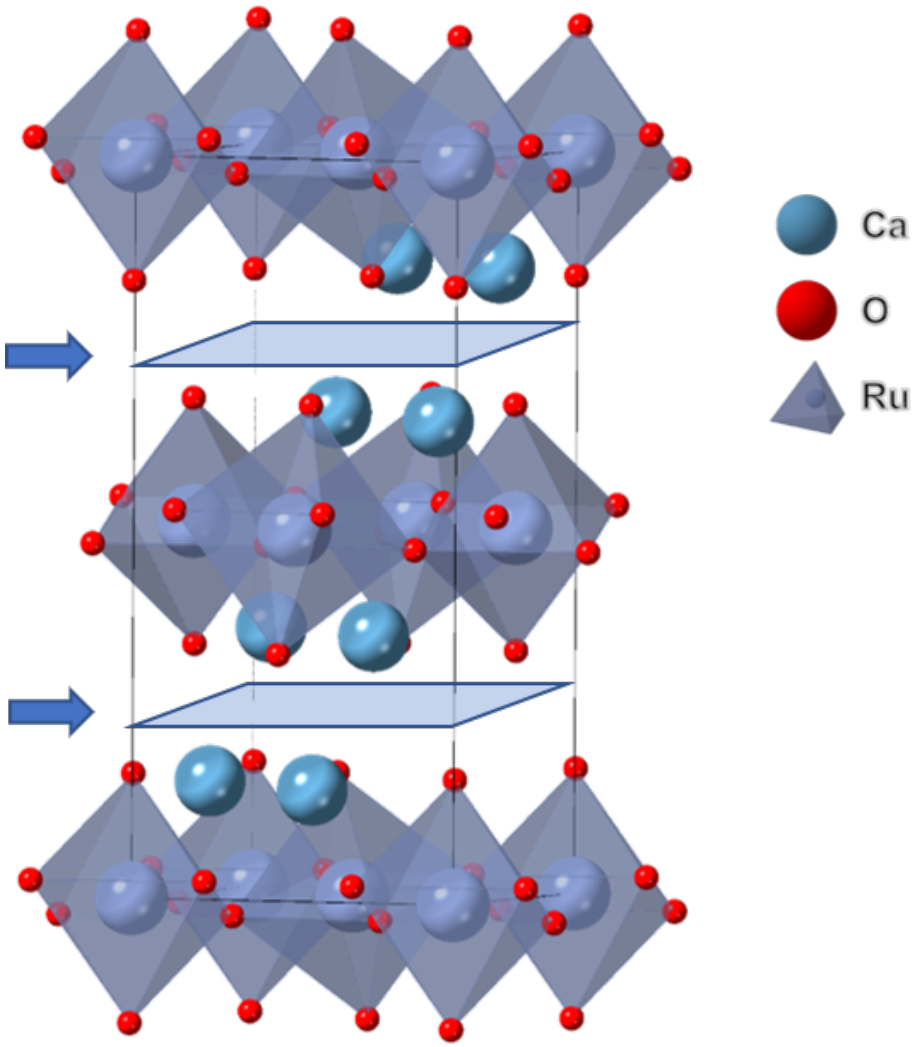

Figure 5.1: The unit cell of Ca_2RuO_4. The crystal will cleave at the plane between the calcium atoms indicated by the blue arrows.

After cleaving, the topography for large scan window is shown in Fig. 5.2. It is clear that on the surface there are several well-defined steps (better shown in the 3D reconstruction image in Fig.5.3). These steps are very common as the cleaving happens at the weakly-bonded position which varies over the crystal surface, though macroscopically the cleaved

surface still looks smooth and reflective.

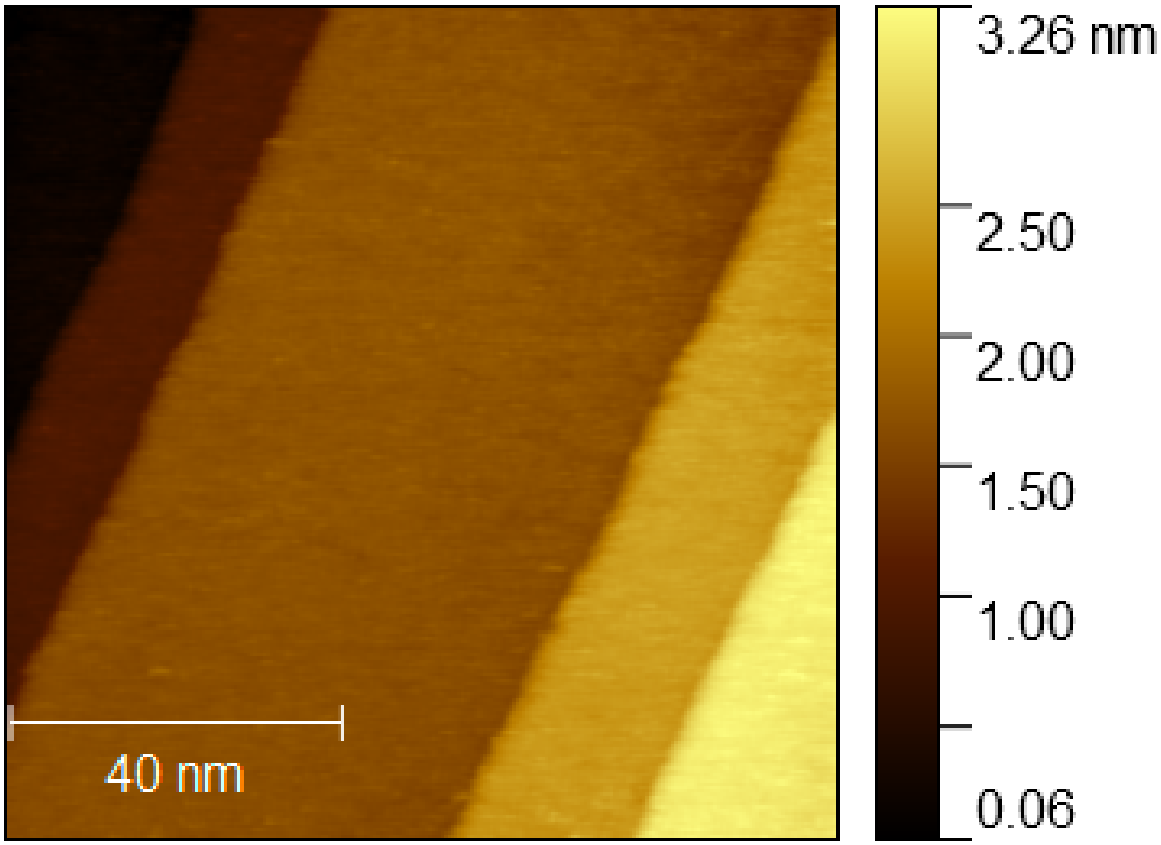

Figure 5.2: The topography of freshly cleaved surface of Ca_2RuO_4.

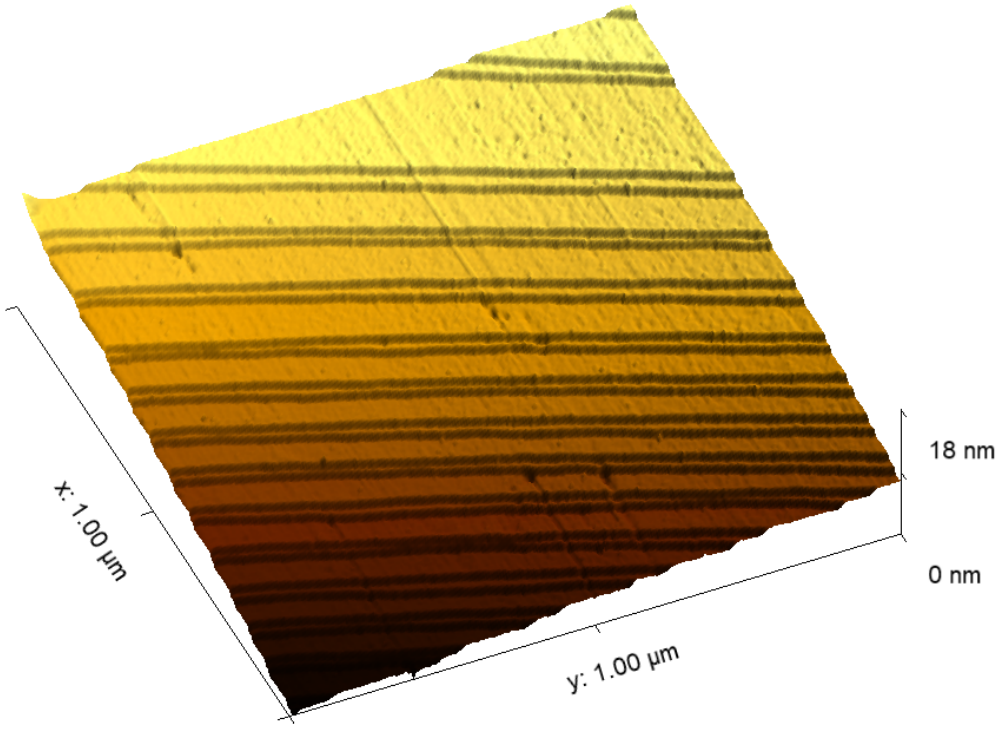

Figure 5.3: The 3d reconstruction image of the topography in Fig. 5.2

When zoomed in on such steps, the STM topography image is shown in Fig. 6.1. The STM bias is $1.5V$, tunneling current is 50 pA, temperature is $T = 302K$. The diamond lattices marked by the blue squares are the Calcium atoms. The stripes are correponding to overlapping Calcium atoms in Fig. 5.5. This topography clearly shows the signature of the Ca_2RuO_4 structure and proves the quality of the crystal and the tip.

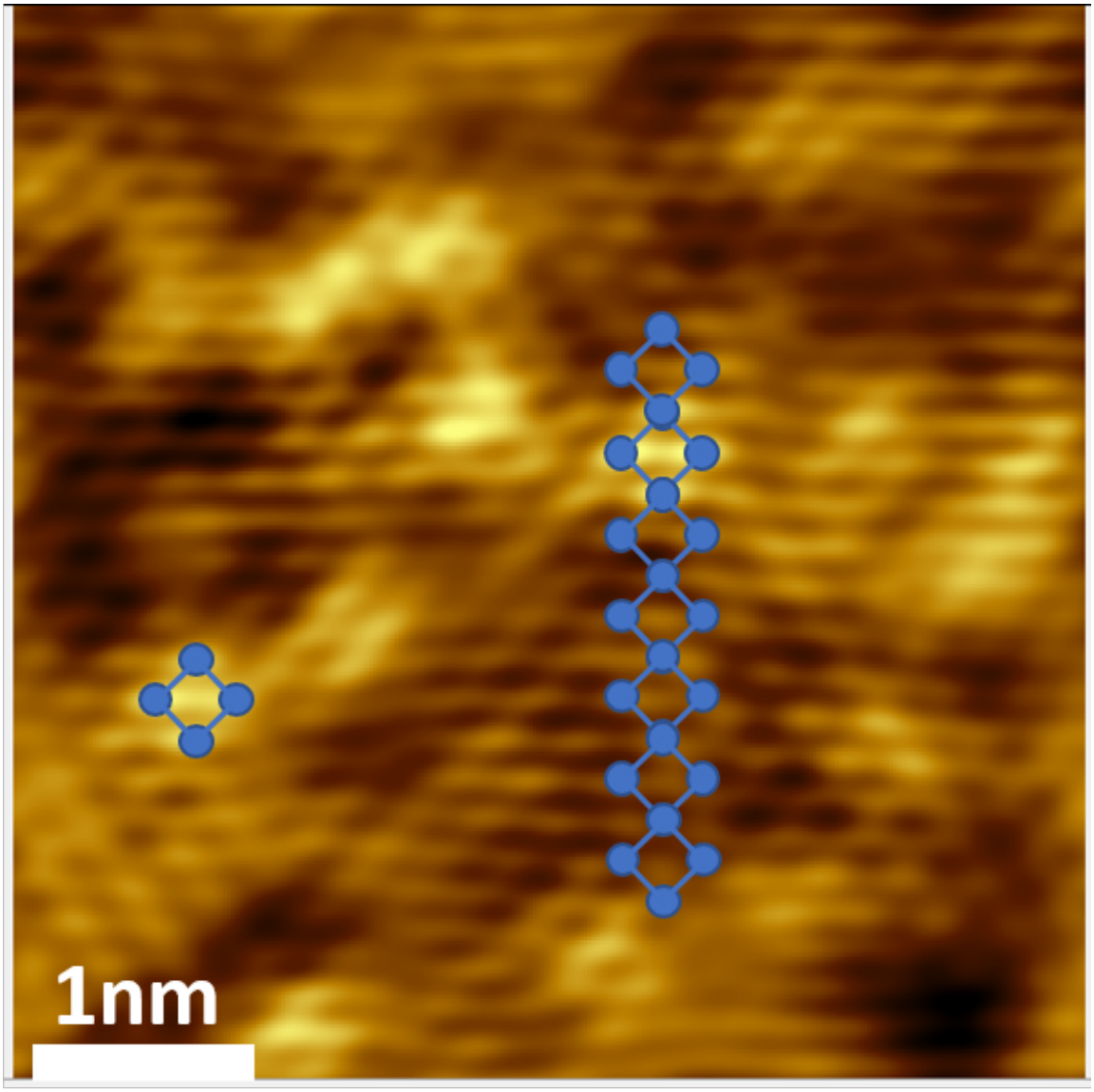

Figure 5.4: The topography of the cleaved surface of Ca_2RuO_4. The white scale bar is 1nm.

After the cleaving, the surface seen from the top is shown in Fig. 5.5.Unit celles are marked by the black boxes. The main feature here is the diamond lattices formed by the Ca atoms. Moreover, the Ca atoms of the top layer and the layer beneath overlap along the b-axis. This leads to the stripe pattern shown in Fig. 6.1.

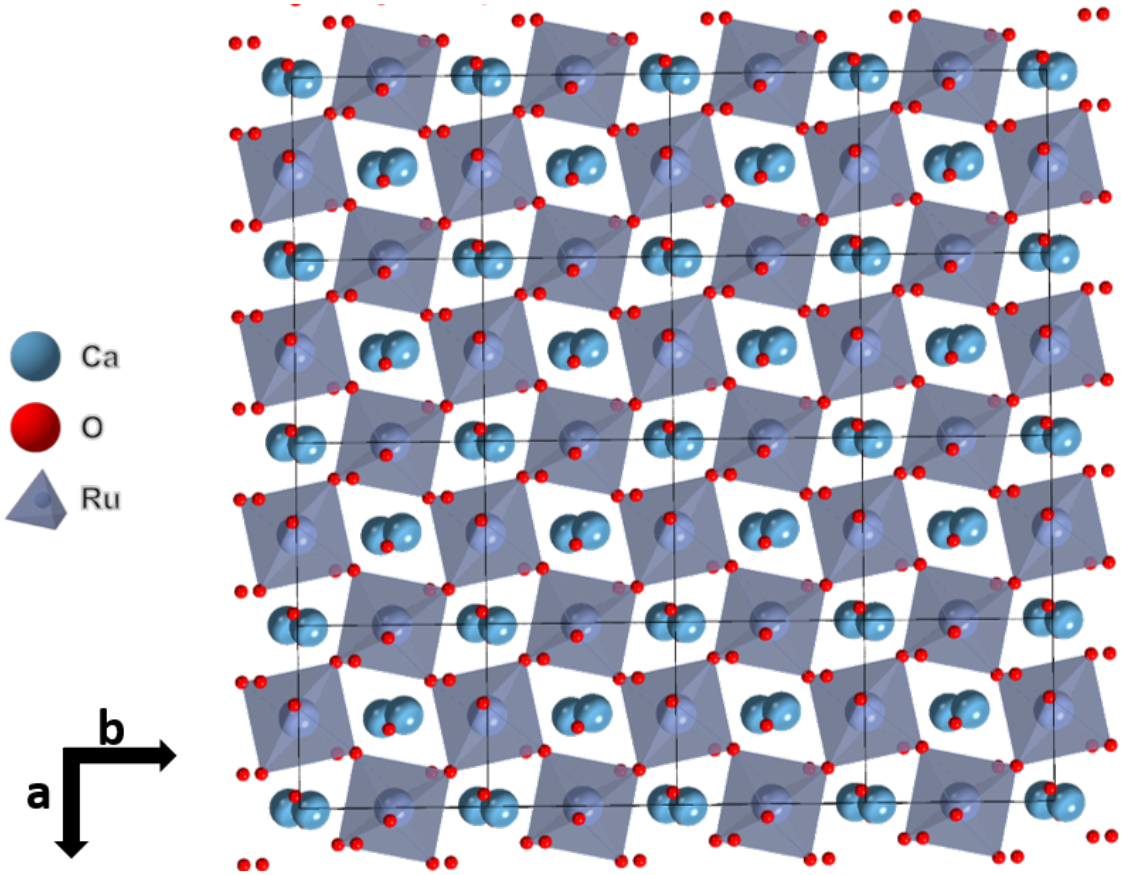

Figure 5.5: The top view of the cleved surface of the Ca_2RuO_4

To further test the quality of the crystal, resistance is measured in a variable temperature cryostat, of which the data is shown in Fig. 5.6. The abrupt drop at $T_{MI} = 357K$ marks the first order transition from an insulator to a metal. And after the crystal enters the metal phase, the resistance increases again with increasing temperature, which is expected for a metal.

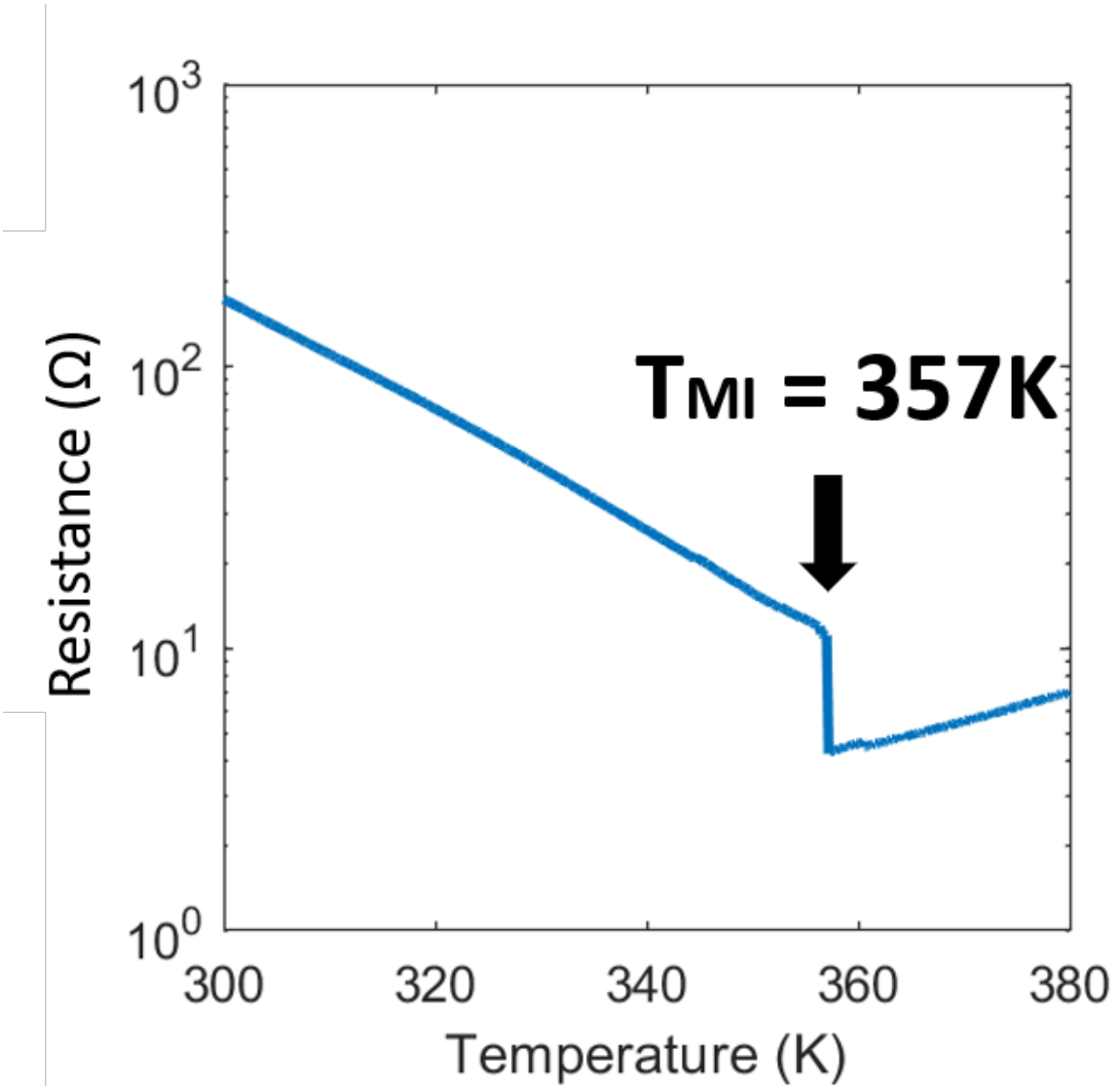

Figure 5.6: The resitance curve of Ca_2RuO_4. The metal-insulator transition happens at $T_{MI} = 357K$

5.2 Tunneling Spectra at Different Temperatures

Now we start to characterize the temperature-driven MIT through the spectral perspective. Due to potential spatial inhomogeneity on the surface, we choose to perform the STS measurement over a carefully chosen area, which is divided into a 16 x 16 matrix and the

result in each sub grid is averaged as the final output. The STS taken using this approach is shown in the right panel of Fig. 5.7. Data is shifted vertically for better visibility and the corresponding zero baselines are makred by the dashed lines. All spectra share similar asymmetry towards the valence band (negative energy side). At 302K, a gap of roughly 50meV is extracted, indicating the sample being in the Mott-insulating phase.

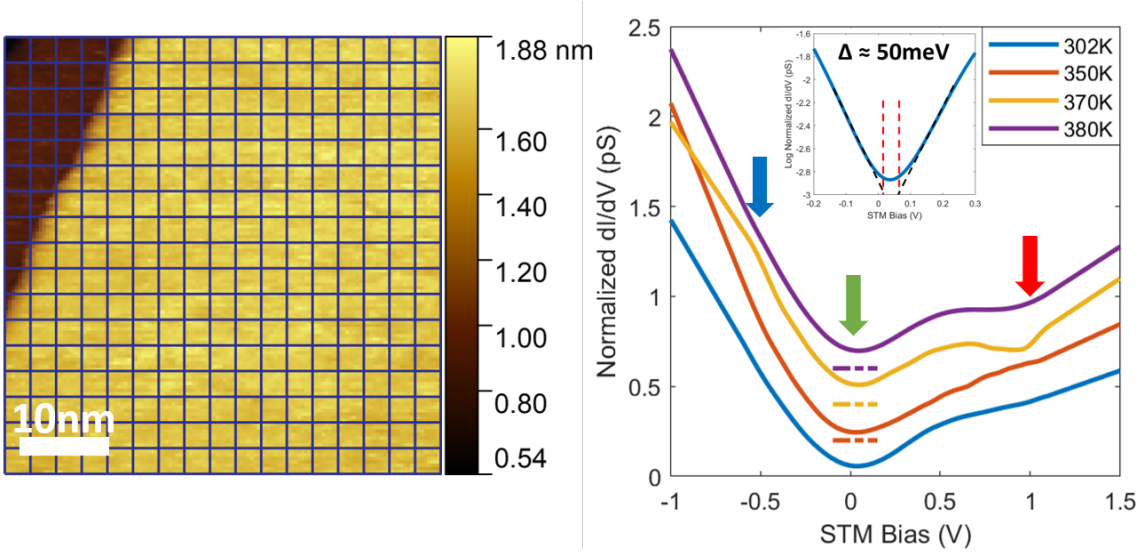

Figure 5.7: Left: a representative surface for STS measurement. The blue grid mark where the STS is performed. Right: The normalized dI/dV at various temperatures. Inset: gap extraction for 302K STS.

To visualize the evolution of the STS along temperature more clearly, we choose 3 positions marked by the arrows in Fig. 5.7 to investigate. The results are shown in Fig. 5.8. The top panel shows a sudden jump of the normalized dI/dV at 0eV once temperature is above $T_c = 357K$. This indicates the gap is closed. Since the spectra still shows a general U shape centered at the Fermi level, we believe this insulating gap is replaced by a pseudo-gap for the metallic phase. The dI/dV at 1eV shows the opposite trend as the value drops across the phase transition. Combined with the STS in Fig. 5.7, we can see there is density of states transfer from high-energy zone towards the Fermi surface during the MIT. Finally, the constant increasing in the dI/dV at -0.5eV further confirms the trend that more

and more states are pushed towards the valence band, which agrees with the picture of a gradual break-down of Mottness.

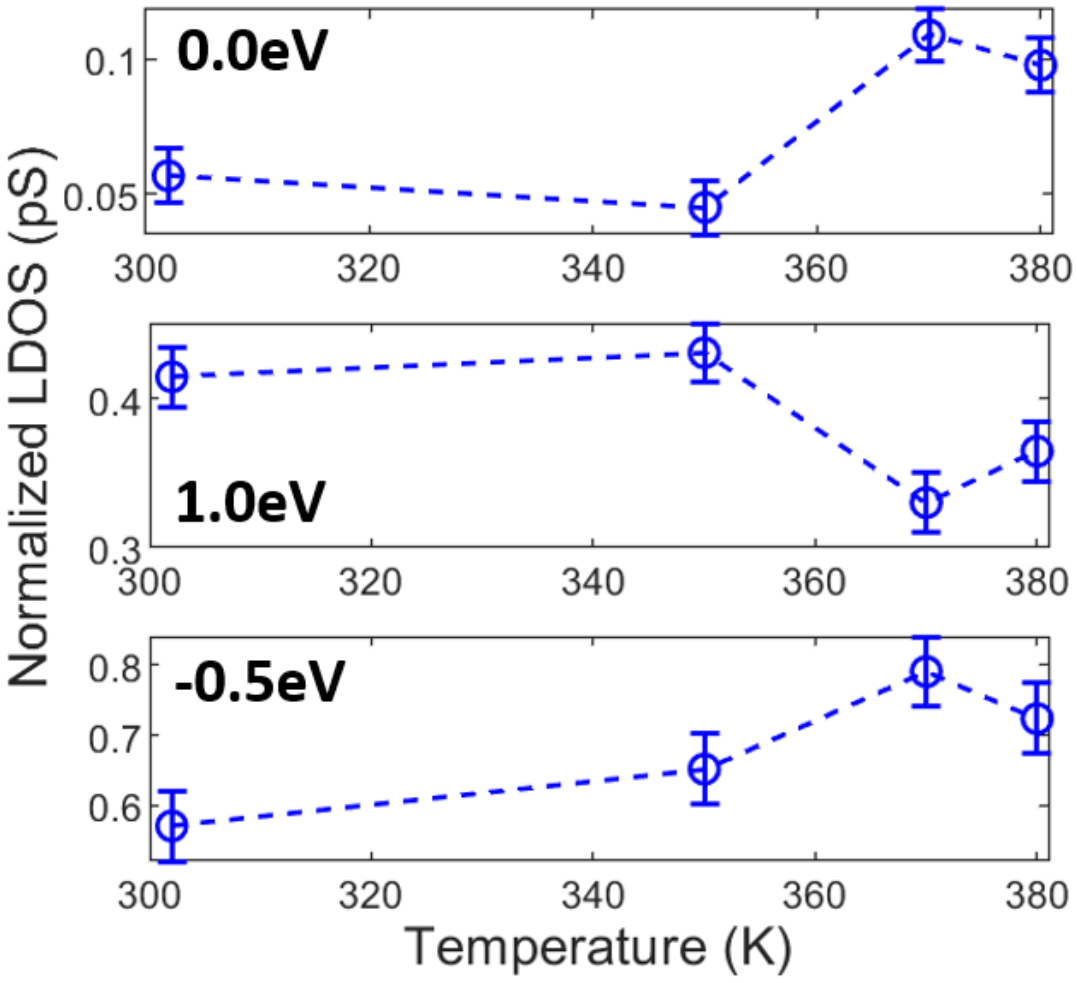

Figure 5.8: From top to bottom: the normalized dI/dV at 0eV, 1eV and 0.5 eV

5.3 Analysis of Tunneling Spectra at Different Temperatures

In order to understand the temperature-driven more comprehensively, a DMFT calculation of spectra weight is done by our colleagues, which is shown in Fig. 5.9. The DMFT is conducted for 2 different temperatures, of which the structures have been characterized

experimentally. The left panel is the total spectral weight obtained from summing up the d_{xy} , d_{xz} and d_{yz} orbitals. The 295K result shows a gap of roughly 100meV near the Fermi sufrace, which agrees with the insulating scenario. The 400K result shows no gap. In fact, it suggests the density of states should increase drastically around the Fermi surface, which though is not observed in our STS. This might be due to low sensitivity of the tunneling current to the d_{xy} orbital. The comparison between these results also shows lots of states are pushed towards to the Fermi surface, which is confirmed by our experiment. Since the DMFT calculation is based on the lattice, these result once again emphasizes the vital importance of lattice structure in the MIT of Ca_2RuO_4.

To show the evolution more clearly, the right panel of Fig. 5.9 shows the distribution of the integration of the DMFT spectral weight for every 0.5eV. This ratio is defined as the integrated spectra weight of each 0.5eV bin divided by the total weights integrated from -1eV to 1.5eV. Apparently, one could see lots of states are pushed towards the Fermi surface for the 400K case. This once again supports the states transferring picture.

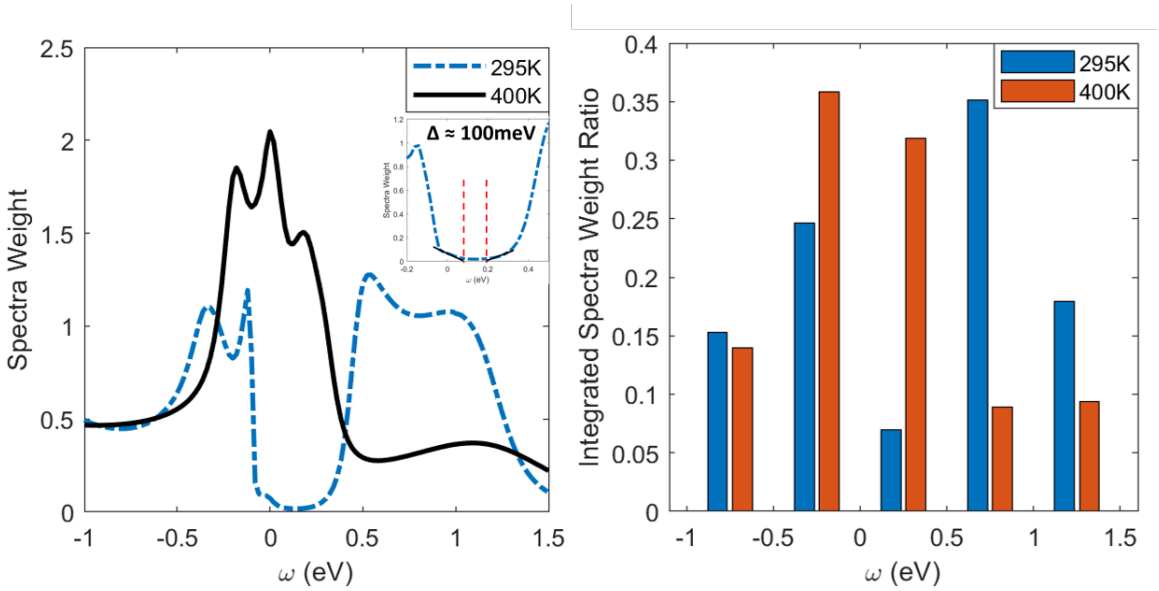

Figure 5.9: Left: the total spectral weight calculated via DMFT. The data shown here is the sum of the d_{xy} , d_{xz} and d_{yz} orbitals. Inset: the gap extraction for the 295K DMFT result. Right: The integrated spectra weight ratio of the DMFT calculation. This ratio is defined as the integrated spectra weight of each 0.5eV bin divided by the total weights integrated from -1eV to 1.5eV.

Chapter 6

Current Driven Phase Transition

One of the most sophisitcated phenomenon in Ca_2RuO_4 is it features a MIT that can be triggered with a small DC current. Though similar non-equilibrium phyiscs have also been reported in other materials, few has been discovered about the mechanism governing such transition. Here we report our findings on the STM measurement when source current is applied on Ca_2RuO_4.

6.1 Topography of Ca_2RuO_4 under Sourcing Current

The topography measurement when source current is applied is slightly different from the ordinary one, yet the fundamental part remains the same. We managed to set up a differential voltage between our tip and the local probing point on the sample surface, and set a tunneing current to get the topography scan. Details of the mesurement will be described in 6.2. One typical image obtained is shown in Fig. 6.1. The main feature of this image is the same with the case without source current. On the surface we can also steps created by the cleaving, too. Once again to deal with the potential surface inhomogeneity, we apply the same method to divide the surface into a 16 x 16 grid for STS measurement. This high-quality topography image once again verifies the qualtiy of crystals used in our experiment.

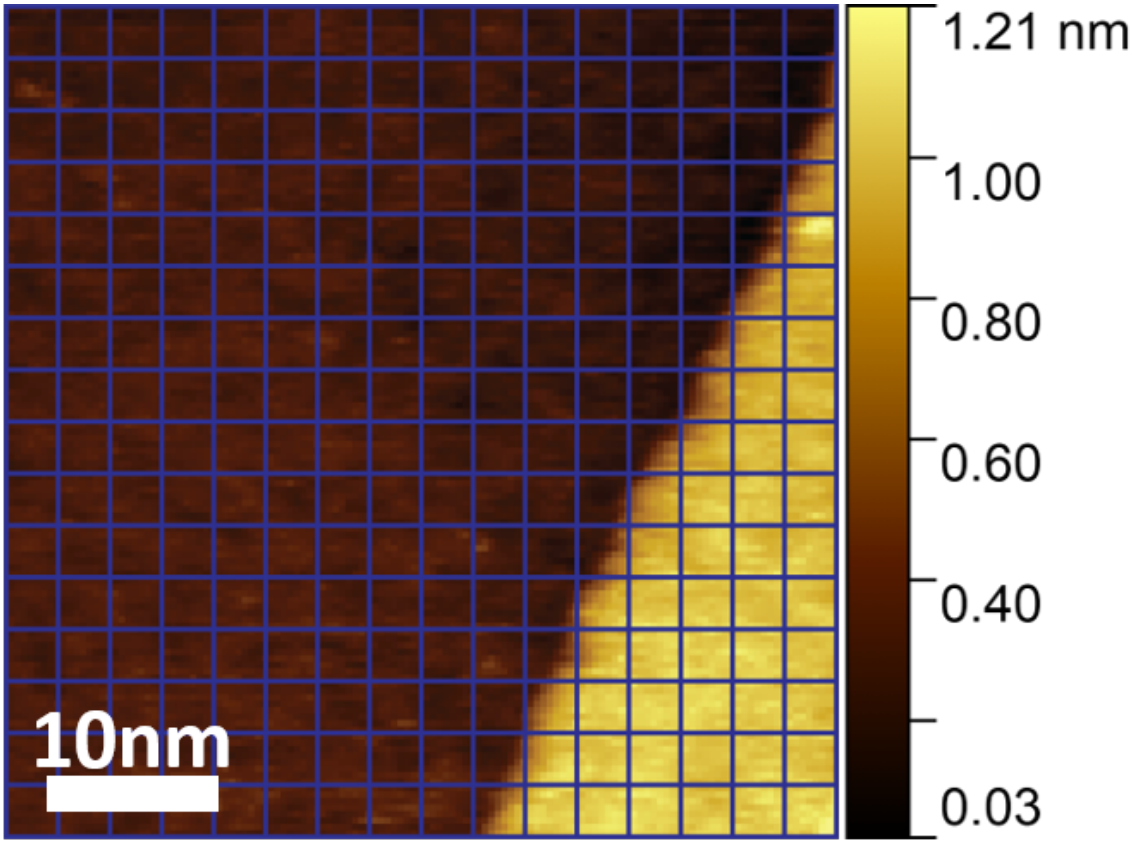

Figure 6.1: A typical topography of Ca2RuO4 under DC current. The image is taken at 1.0mA source current over a 50 nm x 50 nm area. The blue grid represents the STS measurement positions.

6.2 Tunneling Spectra at Different Source Current

6.2.1 Methodology

Before we enter the discussion about the tunneling spectra at different source current, we need to figure out how to measure such spectra under non-zero source current as there will be more than one current/voltage involved. This non-trivial problem needs to be solved properly since the tunneling current and source current might intefere with each other, though their magnitude is differed by 5-6 orders of magnitudes. In an ordinary STM experiment, there is only voltage, the STM bias voltage, and one current, the tunneling

current. Hence the whole sample (or tip depending on the STM configuration) is always at the bias voltage. When taking STS measurement, one just needs to vary the bias and record the tunneling current and conductance. This trivial measurement is not feasible when there is soruce current along the crystal, creating a potential gradient over the whole sample based on the geometry. In this case, the true bias, i.e. the potential difference between the tip and the probe position on the crystal is almost always different from the STM bias (from now on we will call this bias the nominal bias, distinguished from the true/effective bias). Even worse, this effective bias will change with the source current and the material's property should it is also dependent with the current.

To solve this wicked problem, we employ the following sample geometry as shown in Fig. 6.2. The details of the sample fabrication is described in Chapter 4. Two contacts (golden parts in the Fig. 6.2) made from room-temperature-cure silver paint is carefully put at two ends of the Ca_2RuO_4 crystal, one of which is also connected to the STM nominal bias. The source current generated from a current source is applied to these contacts. The tip in our STM is alwasy grounded, so the effective bias is equal to the voltage at the probing point with respect to the ground. Under this effective bias voltage, there will be a tunneling current flowing from the sample to the tip. Hence in order to take STM measurement, all we need to know is this effective bias.

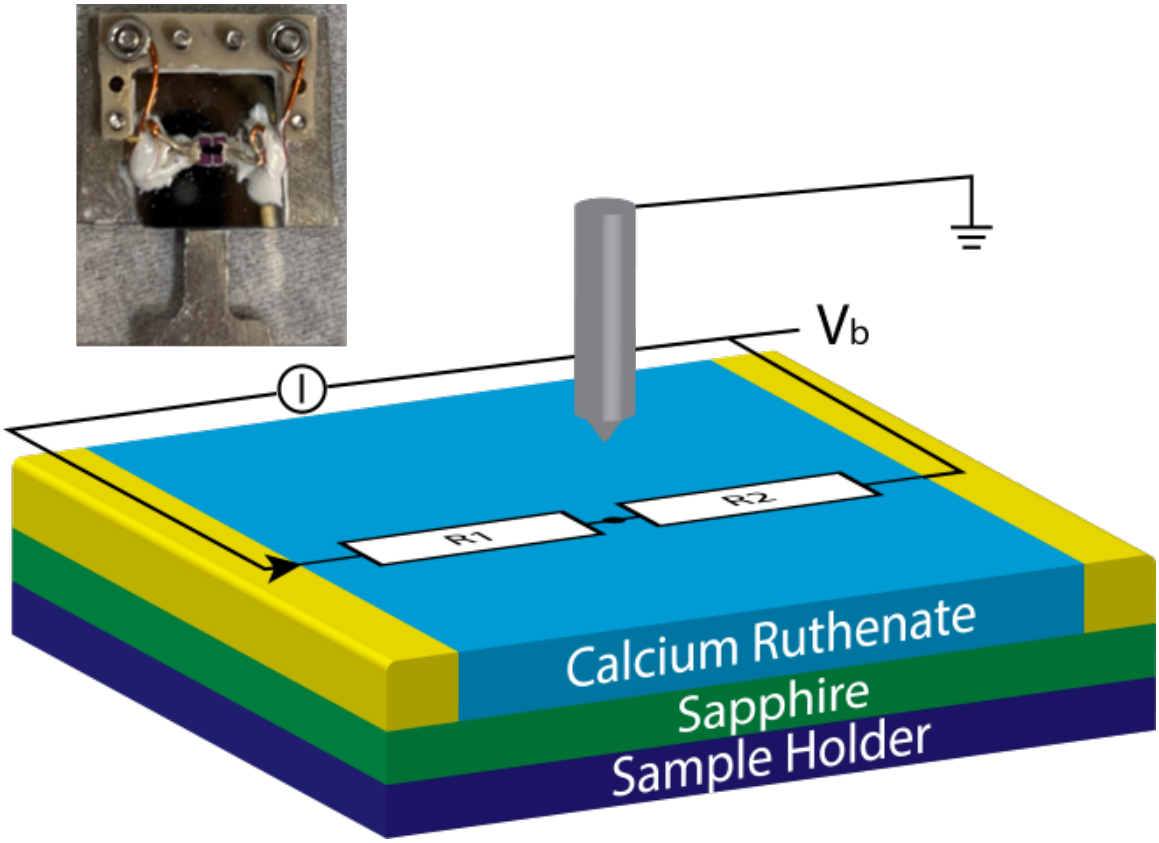

Figure 6.2: The cartoon showing the geometry of the sample used in current sourcing measurement. Inset: the photo of one actual sample

In order to figure our this effective bias, the sample is modeled into an effective circuit as shown in Fig. 6.3.The R_1 and R_2 are the effective resistance of the wire and the sample on the lerft/right side of the probing point. From this circuit diagram we can see the effective bias is:

$$\begin{aligned} V_{eb} &= V_{\text{bias}} + I_{\text{source}} \cdot R_2 \\ &= V_{\text{bias}} + V_{\text{offset}} \end{aligned} \tag{6.1}$$

where $V_{\text{offset}} = I_{\text{source}} \cdot R_2$. Therefore when the source current is not changing and the material enters a quasi-equilibrium state (meaning the property of the material is not changing druing the measurement), the offset voltage is constant. Thus once we know this offset voltage, we know the effective bias.

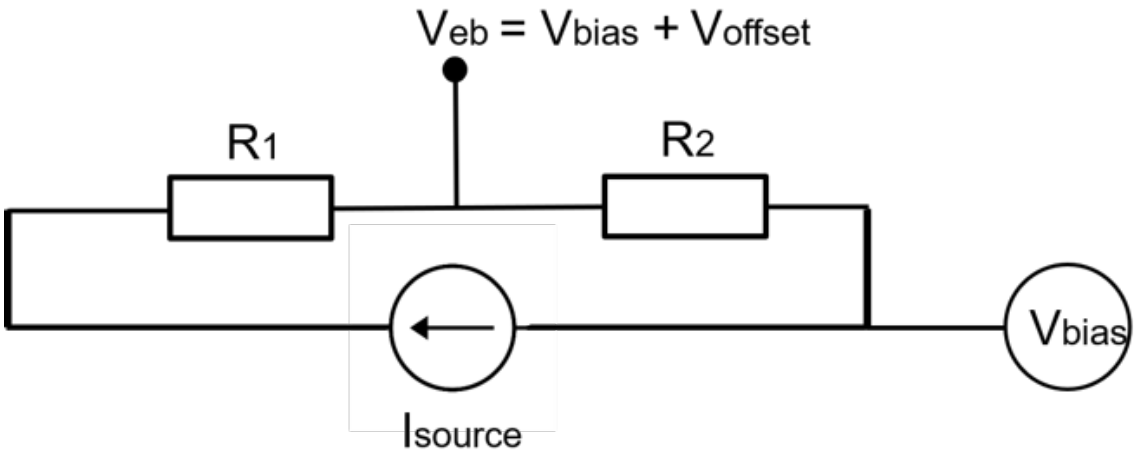

Figure 6.3: The effective circuit of the system for current sourcing experiment.

Mathematically the offset voltage cannot be obtained unless we know the effective resistance R_2, whcih practically is quite hard to estimate. However, when the effective bias is zero, which means the STM nominal bias equal the negative of the offset voltage, the tunneling current must also be zero. We can take advantage of this fact to experimentally measure this offset. First we can just take a tunneling current measurement when varying the STM nominal bias, as shown in the left panel of Fig. 6.4. By finding the zero point of the tunneling current, we can locate the corresponding nomial bias, which equals to the negative of the offset voltage as we mentioned above. Therefore we can extract the offset voltage for each spectra we take, then offset the nominal bias by this value we will get the effective bias. The rest is straightforward, one can either take the derivative of the tunneling current with respect to the effective bias or turn on the osillation and measure the conductance directly. In our experiment we apply the former method as it not only shows better stability but also makes the determination of the offset voltage more precise. Several representative spectra are shown in the right panel of Fig. 6.4

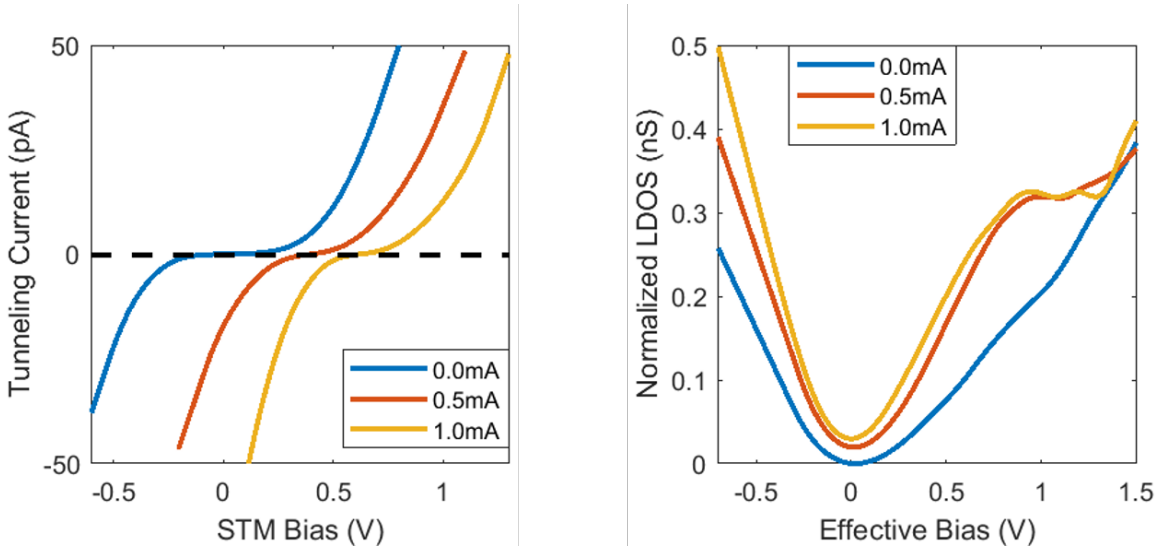

Figure 6.4: The approach to determine the effective bias voltage

It is worthy to point out this method of finding the effective bias certainly involves some extent of intrinsic error. The tunneling current is typically on the order of 100 pA, which is extremely small compared to all soruces of electrical noise in our daily life. Therefore the reading of the current is possible to be more or less inaccurate. The next potential source of error lies in the way the spectra is taken. During the spectra measurement, the nominal bias and effective bias varies in a relatively fast fashion. This fast-changing voltage can introdcue a capacitive current, which will be recorded together with the authentic tunneling current. In order to get rid of the effect of this capacitive current, before each spectra is taken, the current reading is re-zeroed so that when the fine scanner is retracted, the tunneling current will remains zero when nominal bias varies in the same range. When the tip is retracted, the distance between the tip and the surface is 100 nm, which is sufficient to suppress any tunneling current and the capacitance will not change much considering the size of the smaple and the tip wire. Finally the inevitable error comes from the property of the material. When dealing with material with gap, one can expect the tunneling current remains zero when the effective bias is in the gap. This will dramatically increase the difficulty of determining the zero point of the current and generate a large uncertainty based on the size of the gap. Unfortunately Ca_2RuO_4 is a Mott-insulator at room temperature

and in small current density range, in which we expect there is a gap. Hence to compenstate the impact made by this issue, 2 methods of data analysis are applied. The first one is to fit a normal distribution of the nominal bias corresponding to the smallest absolute value of tunneling current (in another word, the mathematical zero point) for each spectra. This comes from the assumption that the measured positions of the tunneling current zero points should follow a normal distribution, as widely employed in many physical experiments. The second one is to find the onset nominal bias voltages when tunneling current is below a predetermined threshould (say 0.2 pA), and then use the average of the 2 onset voltages as the zero-point (to some extent, this is the physical zero point if we believe the gap is symmetrical in small energy range). In most cases the positions of current zero points found via these 2 methods are quite close and we choose the average of these 2 as the finally accepted value.

6.2.2 Transport Measurement with Source Current

Before we perform any spectra measurement, it is crucial to conduct a transport measurement with source current. This will enable us to both know the quality of the used crystal and understand where we are in terms of the phase transition. Using the geometry introducted in Fig. 6.2, we perform a IV measurement for each crystal we measure. The representative result is shown in Fig. 6.5. We find the crystal shows different properties when current is varied in different directions. Such significant hysteresis is reported in other work, too[31]. With current increasing, more and more portion of the crystal turns into the metal phase, decreasing the total resistance hence creating the nonlinear behavior of the source voltage. When a sufficient portion of the crystal enters the metal phase, the source voltage will start to drop. This happens at the peak of the source voltage, which is around 2mA. (black dashed line in Fig. 6.5). This IV characterization confirms the quality of the crystal and provides us very meaningful information of where STS should be taken, which are indicated by the green stars in Fig. 6.5.

It is worthy to point out that we measure the STS along the increasing source current (blue line) as it shows a more significant change in resistance hence the magnitude of phase transition. Also our measurement is done at fairly high temperature of 250K. This is because as the temperature decreases, the voltage peak will increase rapidly so it becomes harder

and harder to trigger the transition (as higher and higher voltage needs to be applied). In our experiment the voltage limit of the current source is 30V and the crystals tend to crack easily once higher voltage is applied, which is a common problem in the study of Ca_2RuO_4[86]. Therefore we choose 250K as the experiment temeperature where we can safely go across the voltage peak and achieve the MIT. Though for lower temperatures it is harder to trigger the insulator-to-metal transition, it is still feasible to go fully into the metal phase at higher temperature and then start decreasing source current or the temperature while maintaining the same source current. Both of these measurement will be introducted in following chapters.

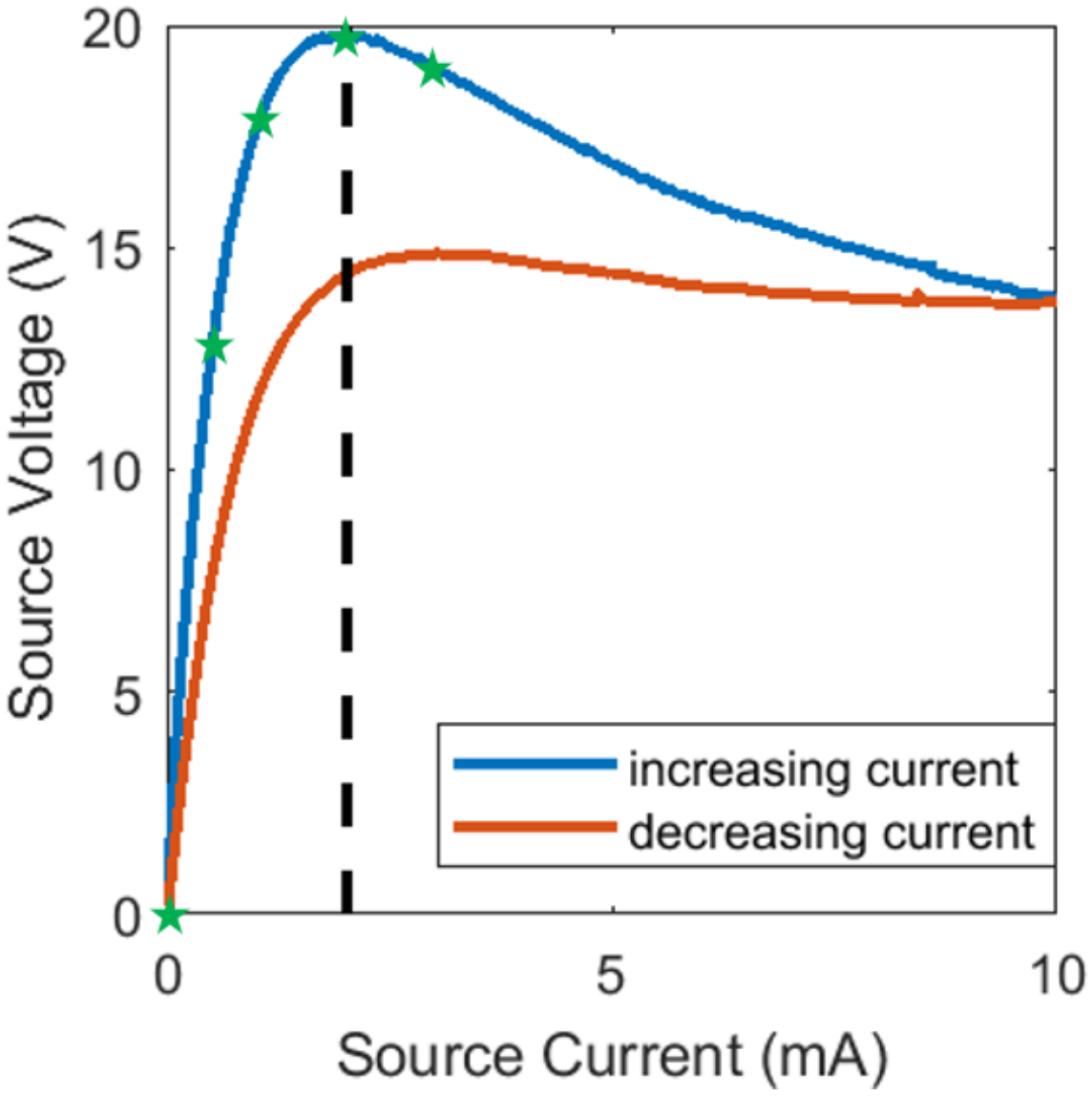

Figure 6.5: The typical IV curve of Ca_2RuO_4 under source current at 250K. The blue/red curve corresponds to the case of increasing/decreasing current. The black dashed line marks the source voltage paek and the green stars indicate where STS measurements are conducted.

6.2.3 Tunneling Spectra Evolution with Source Current

With the method introduced before, we perform STS measurement at various source currents, which covers a wide range in for phase diagram of the current-driven MIT. The result is shown in Fig. **??**. Again, data is shifted vertically for better visibility and the dashed lines are the corresponding zero baselines. The general shape of the STS is very similar with the STS taken at various higher temperatures when there is no source current. Also similar states transfer phenomenon is observed. With increasing source current, the dI/dV around 1eV (green arrow) is suppressed and the dI/dV around 0.8eV is enhanced (purple arrow). This indicates more and more states around 1eV is transferred towards the fermi surface. This similarity reflects an interesting connection between the high-temperature metallic phase and the high-current one.

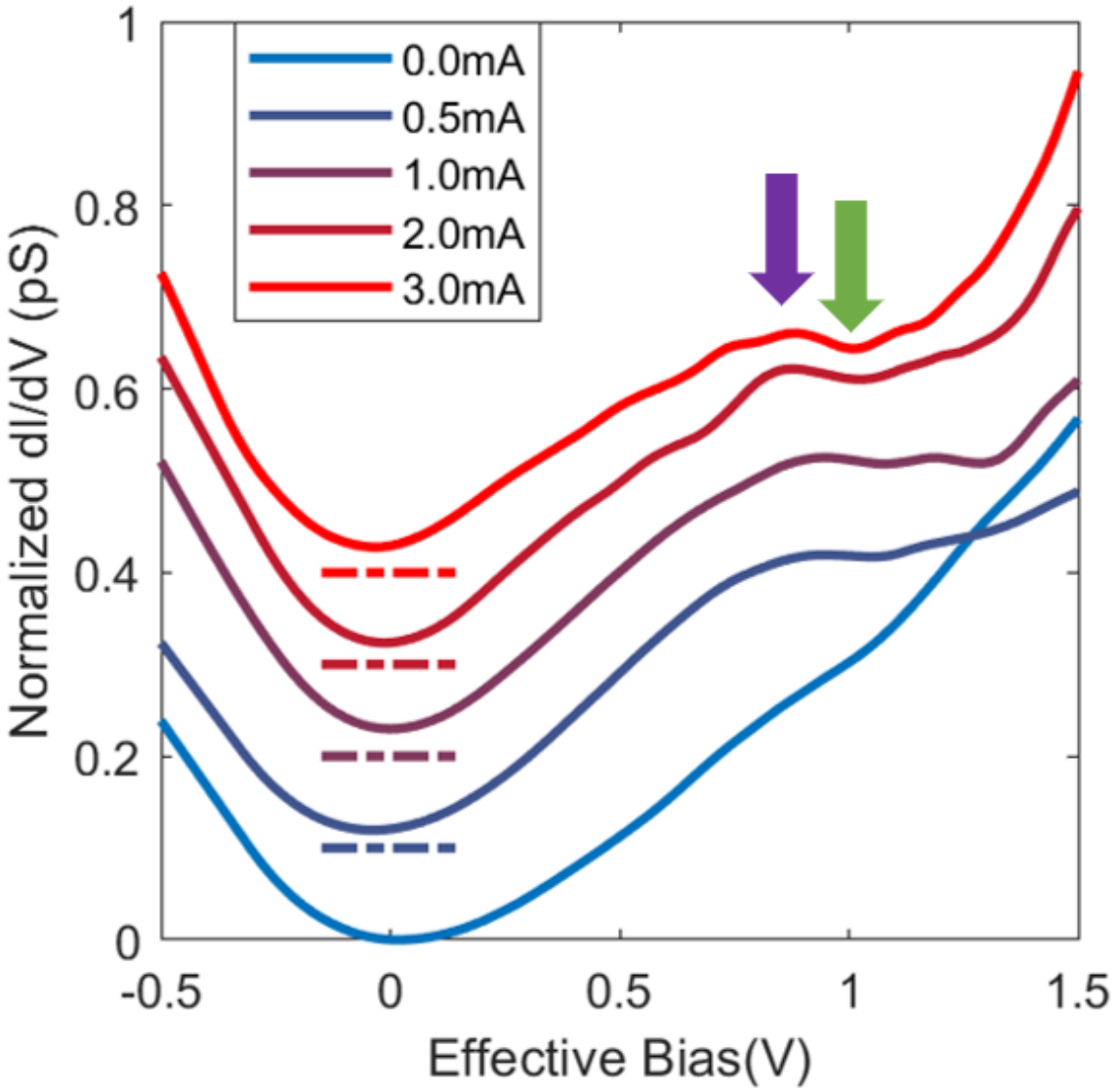

Figure 6.6: The normalized dI/dV at various source currents. Data is shifted vertically for better visibility and the dashed lines are the corresponding zero baselines. Arrows indicate where the dI/dV is taken for transfer ratio calculation.

To demonstrate the states transfer phenomenon more clearly, we introduce a metric called dI/dV Transfer Ratio, which is defined as the ratio between the dI/dV at 1eV and at 0.8eV. This transfer ratio is ploted in Fig. 6.7. With source current increasing, this ratio keeps decreasing, meaning states being pushed towards lower energy zone.

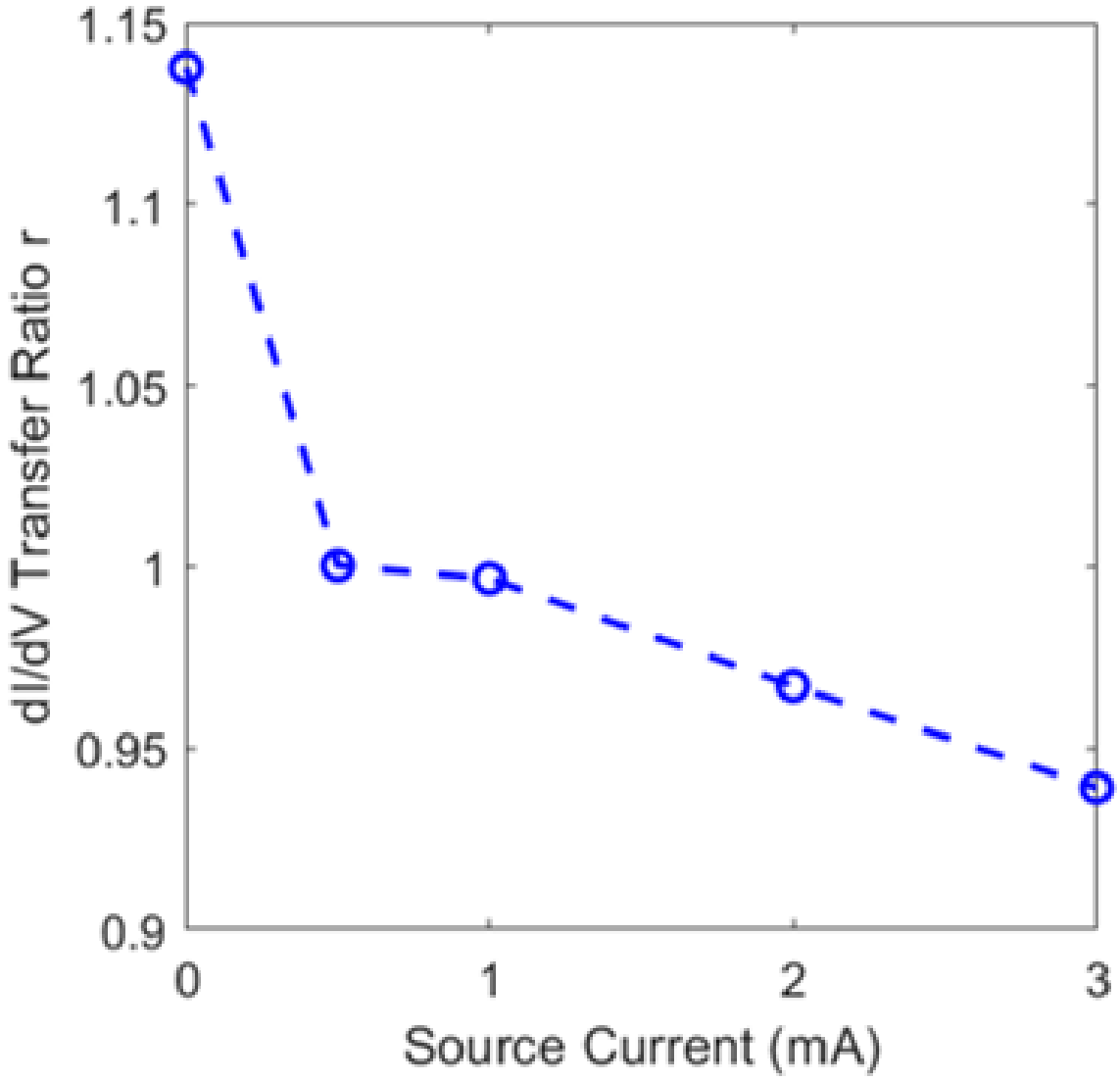

Figure 6.7: The dI/dV Transfer Ratio, which is defined as the ratio between the dI/dV at 1eV and at 0.8eV.

6.3 Analysis of Tunneling Spectra at Different Currents

The STS for current-driven MIT are taken around the voltage peak shown in Fig. 6.5. Note when the crystal are fully in the metallic state, it should have a linear IV curve with a positive slope. Therefore our IV curves show we are not fully in the metallic state,

indicating the STS taken cover the phase transition from a Mott-insulator to a potential phase mixture of an intermediate insulating state and a conducting metal state. Also due to the spatial average, our STS essentially is a weighted average of spectra of these two states. In this case, the subtle evolution of the spectra with respect to source current could be viewed as the outcome of the change in the distribution of the two states. Since we find the states are being gradually transferred from high-energy zone to low-energy zone, the metal phase might have more states near the Fermi surface. Unfortunately this cannot be directly verified as a high-resolution STS map takes way too long for the sample to be stable in this temperature and current. Theoretically cooling down could help on the stability issue (less thermal drift and noise), however the sample resistance would increase exponentially so that it becomes impossible to run sufficient source current to trigger the MIT. Nevertheless, this result provide some insight on the phase mixture picture. As we will see in the following chapter, other measurements support this hypothesis.

Now we focus on the mechanism of current-driven MIT. In order to turn a Mott-insulator into a conducting semi-metal, one must break the half-filling scenario that creates the gap of a Mott insulator. In the case of Ca_2RuO_4, this could be done either with a structural transition that leads to new orbital ordering, or with doping via chemical approach or a current. The first case is what we have observed for temperature-driven MIT, while the second might correponds to what happens for the current-driven MIT. The role of a constant DC current can be seen as doping some electrons to the conduction band, which will break the half-filling requirement and lead to a band reconstruction. In this case, the current-driven MIT has little connection with temperature, indicating once we are fully in the metallic state, we should observe spectra that has little dependence on temperature. The other case is due to the inevitable Joule heating, the local temperature, especially the electron temperature, could be much higher than the measuremed temperature. Therefore once the temperature of a local region reaches $T_c = 357K$, it will experience an ordinary temperature-phase transition. Since the current will alwasy choose the path with least resistance, once certain region turns metallic, the current will prefer to stay flowing through it and its heating will keep that area hot and metallic. In this case, the current-driven MIT is fundamentally the same with temperature-driven MIT, therefore we should see the STS

has a close relation with temperature. In summary, in order to verify which hypothesis hold in Ca_2RuO_4, one could measure the STS at the same current but different temperature. The result of such experiment is presented in the following chapter.

Chapter 7

Comparison Between the Temperature-driven and Current-driven MIT

Since the MIT in Ca_2RuO_4 can be triggered either via temperature or currents, it is natural to ask if the high-temperature metallic state is the same with high-current metallic state. Hence we compare these 2 states from the perspective of STS. As introduced in previous chapter, the non-equilibrium metallic state induced by a DC current has two potential source. One is the Joule heating caused by the current raises the local temperature above the transition temperature hence turns the local region into metallic. The other is the effective doping of the DC current breaks the half-filling scenario that is necessary for the Mott insulator. To distinguish the two cases, we perform STS measurement at a fairly high current and various temperatures. We also conduct surface roughness and autocorrelation length analysis of the surface to illustrate the potential phase-mixture when there is a current.

7.1 STS comparison of the high-temperature state and the high-current state

In order to observe the similarity and difference between the high-temperature state and the high-current state, here we present a comparison between the STS of these two states. Before we enter the comparison, it is necessary to point out due to different sample geometry, it is not feasible to measure these 2 states on the same crystal (The insulating part on the multi-contact sample holder cannot be heated hence we are unable to heat the crystal mounted on it above room temperature). So it is unwise to directly comparet the values of the STS. However, many could be found by merely checking the main feature of these STS. Fig. 7.1 shows the comparison of the STS for the two states. Despite some value difference on the positive energy side (which is fairly reasonable considering they are measured on different crystals), these 2 spectra are exceedingly similar. First of all, the all share a general U-shape and a pseudo-gap near the Ferimi surface, indicating they are indeed conducting. Also both spectra feature the same asymmetry towards the negative energy side. Most of all, they all show the states transferring feature that we have reported in previous chapters. In details, the dI/dV around 1eV are lower than the dI/dV around 0.8eV. As discussed before, this phenomenon of states transfer indicates the break-down of the Mottness. Considering all these similarities, it can be concluded that the high-temperature state and high-current state are highly alike, at least from the spectra perspective. However, it still remains unclear whether they are fundamentally different.

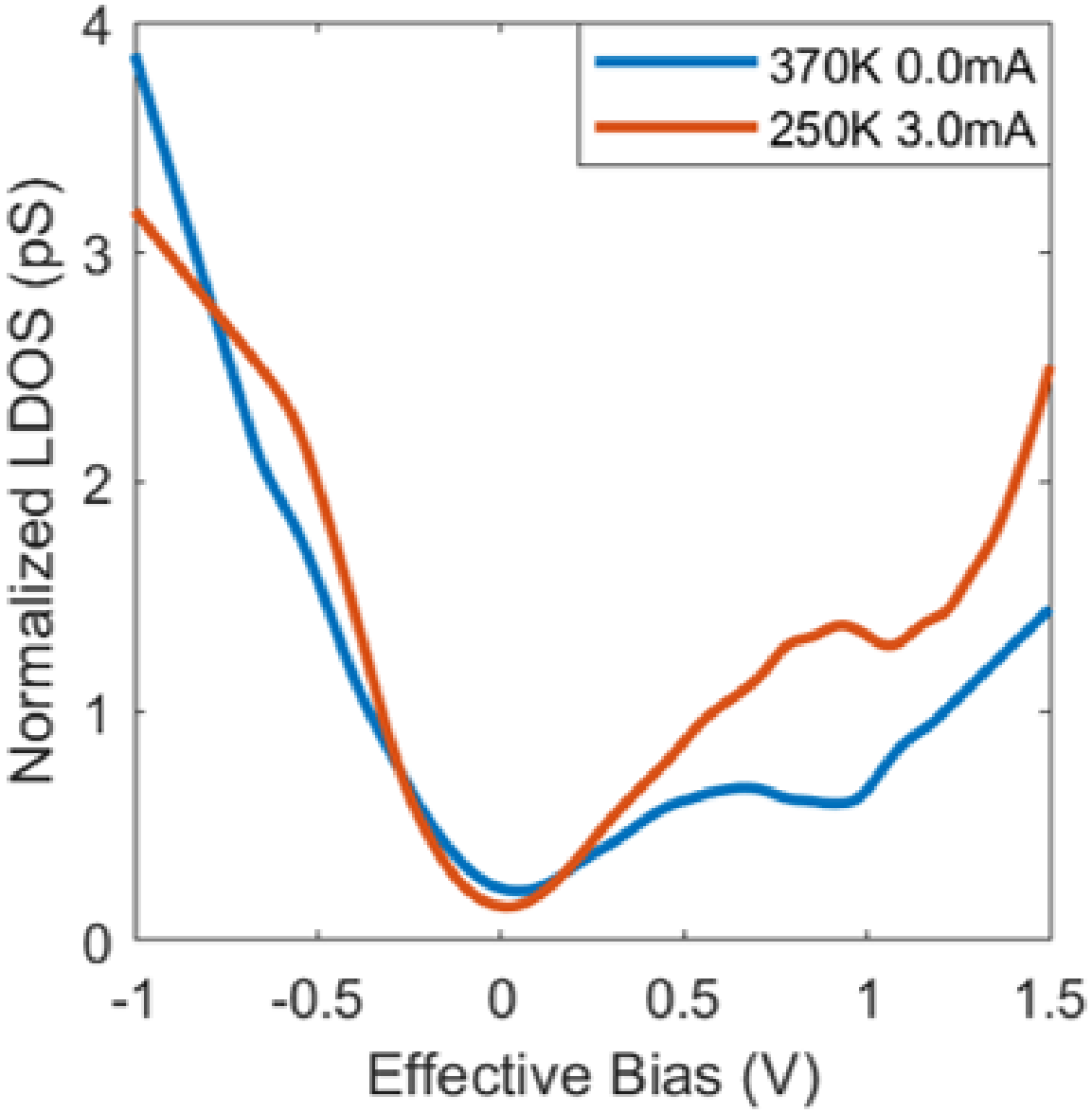

Figure 7.1: Normalized dI/dV for high-temperature metallic state and high-current metallic state

7.2 STS at same current but variouse temperatures

To investigate whether the high-temperature state is different from the high-current state, we perform a measurment of STS at a farily high current but various temperatures. For

other materials, such measurement might technically trivial. However in the case of Ca_2RuO_4, since its resistance will increase exponentially during cooling down, it will be impossible to flow a large enough current to trigger the MIT. Therefore we start with a large current of 10mA at a relatively high temperature of 210K, then we begin to take data and gradually cool down. Since at 10mA the crystal already has a large proportion of metallic state (see the IV curve in the previous Chapter), its resistance will not change such drastically with temperature so we are able to maintain the same source current.

Fig. 7.2 shows the STS measured using the same spatial average method at 10mA and various temperatures. Data is shifted As discussed in the previous chapter, if the high-current metallic state has nothing to do with the Joule heating, the STS should be independent with temperature. Clearly here the spectra show some evolution with temperature, of which the most apparent one is the dI/dV around 1eV. With temperature decreasing, the slope around 1eV gets stipper and stipper. To see this evolution more clearly, we apply the same calculatio of dI/dV transfer ratio here and get the result in Fig. 7.3. From this we can find with temperature decreasing, this ratio keeps increasing. Compared with the previous result, we can see a higher transfer ration indicates the current state is closer to the insulating state. Hence we can see with temperature decreasing, the sample tends more and more insulating. This rules out the picture that the high-current state is due to dopping and has no direct relationship with temperature.

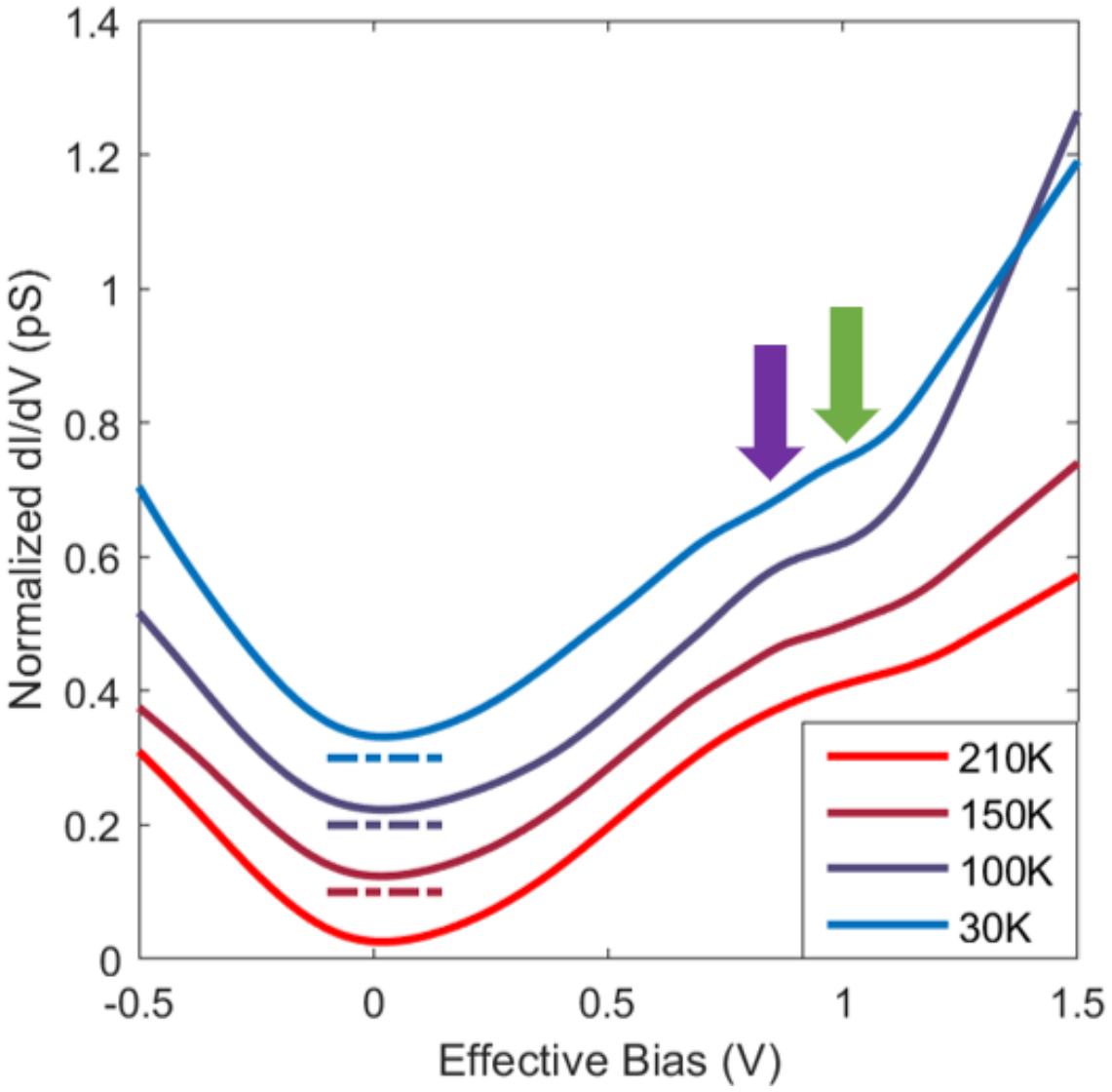

Figure 7.2: Normalized dI/dV taken at different temperatures when source current = 10mA. Data is shifted vertically for better visibility and the dashed lines are the corresponding zero baselines. Arrows indicate where the dI/dV is taken for transfer ratio calculation.

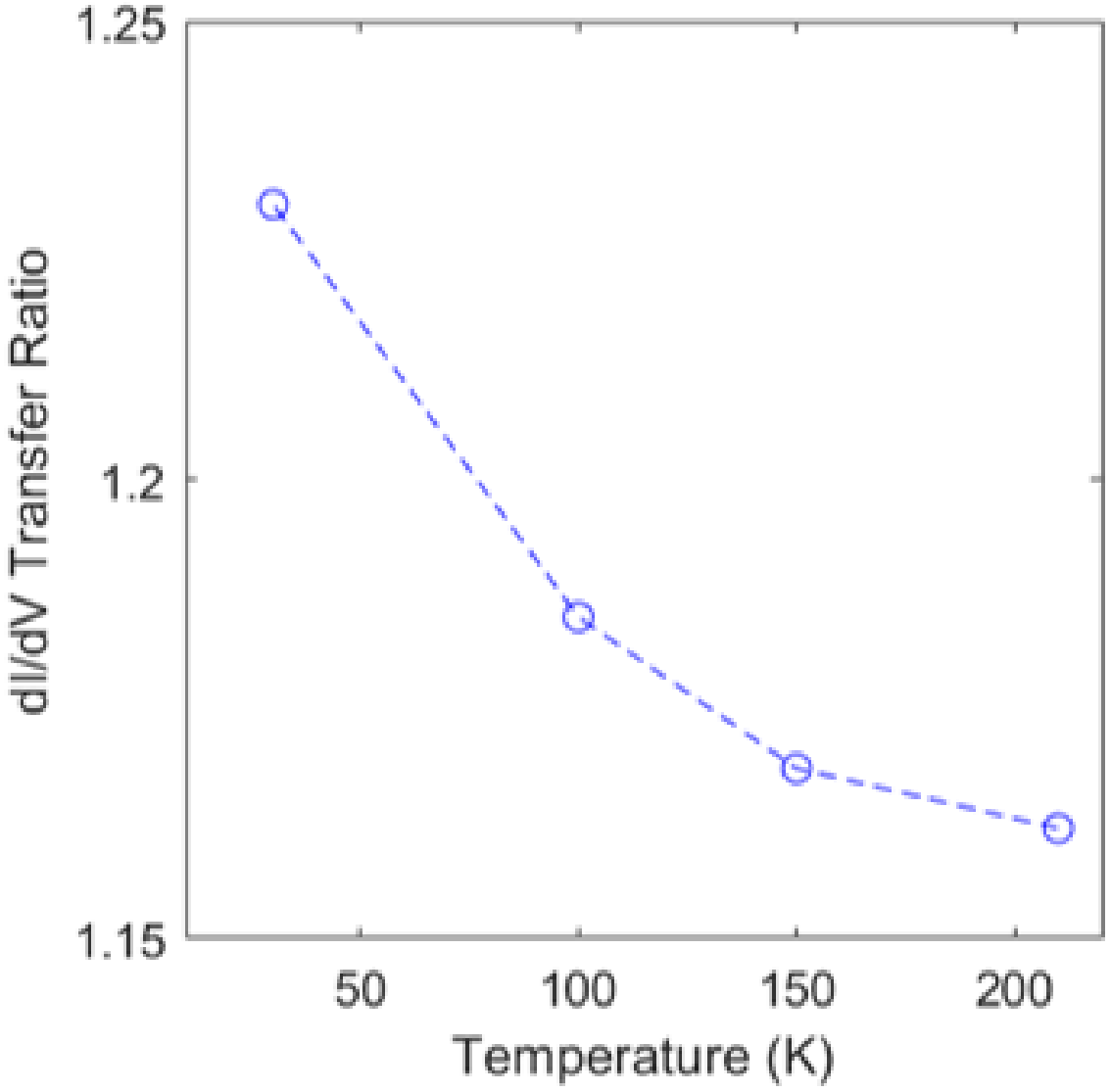

Figure 7.3: The dI/dV transfer ratio, which is defined as the ratio between the dI/dV at 1eV and at 0.8eV.

In order to understand this result more comprehensively, we consider the similar transport measurement at various temperature from other study[16]. We can see from high temperature to low temperature, the position of the voltage peak comes earlier and earlier, and the height of the voltage peak comes higher and higher. For the high temperature curve, after the peak, it becomes very flat, indicating most of the crystal are in the metallic

state. While for the low temperature ones, after the voltage peak, they drop with various speed. As discussed before, this is due to more and more proportion of the crystal turning into the metallic hence decreasing the total resistance. Therefore this droping in voltage indicates there are still a significant proportion of the crystal remains insulating. As a rule of thumb, we could use the distance to the voltage peak and the slope of voltage decreasing after the peak as a metric to determine the proportion of the metallic state, i.e. an order parameter.

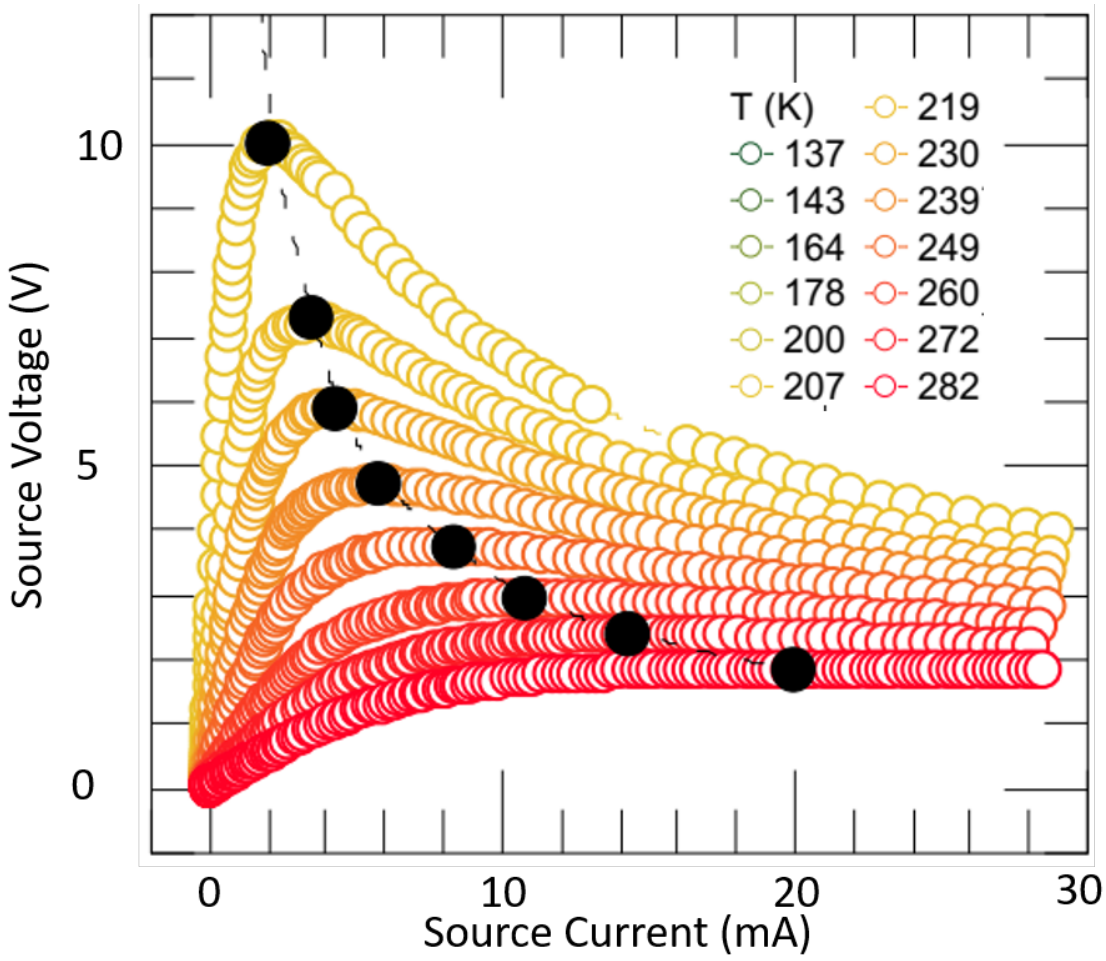

Figure 7.4: The IV curve of Ca_2RuO_4 at various temperature. The color indicates the temperature. The black circles mark the position of the voltage peak. This figure is taken from [16]

Now if we observe these IV curves at a certain current cut (for instance 10mA), we can see with temperature decreasing, we are further away from the voltage peak, and the voltage decreasing slope gets steeper. This means we are turning closer to the insulating state, which agrees with our STS results and the local temperature explaination. In fact, it is recently reported that the local temperature measured via infrared thermal imaging stays the same for both temperature-driven MIT and current-driven MIT. All of these combined, we can find the Joule heating and local temperature has vital importance in the current-driven MIT. It is very likely the Joule heating brings the local temperature above the transition temperature then turns the local region metallic. Also when measured temperature decreases, it becomes harder for the heating the rasie the temperature to transition temperature. Hence it requires more source current in this case. Finally, since our STS is a spatial average, this result probably comes from an inhomogeneous surface that evolves with local temperature, which has been reported in X-ray and neutron scattering measurements before [10]. We will discuss this part in details in the following session.

7.3 Surface Inhomogeneity Analysis

As mentioned above, since there are two states emerging under a DC current, our results might stem from an inhomogeneous surface with these two states co-existing. To verify this, we perform surface roughness and autocorrelation analysis on the topography images of the same area on the crystal at a series of source currents. Due to the same resistance issue mentioned before, we cannot start from the left side of the voltage peak. Instead, we maintain the source current at 10mA and cool the system to 100K. Then we start to decrease the source current and take topography images. We keep conducting this measurement until the source voltage reaches our current source limit (30V), at which the source current is barely below 5mA. During the measurement we stay at the same area (no movement of the sample and the tip). However, there is still some inevitable thermal/random drift during the measurement. We believe this should have minor imapct on the result.

Fig. 7.5 shows the average surface roughness of the same 50nm x 50nm area of various source current at 100K. As one could see, in general with source current decreasing, the

surface becomes more and more rough. This could be explained with as source current decreases, there are more proportion of the crystal enters the insulating phase, creating a more significant phase-coexisting surface. Considering phase coexisting reported in [10], we believe this is related with the intermediate insulating S* phase being gradually suppressed and the conducting L* phase being enhanced along increasing source current. Since the 2 phases have slightly different lattice constants, their coexisting will lead to a rougher and more inhomogeneous surface.

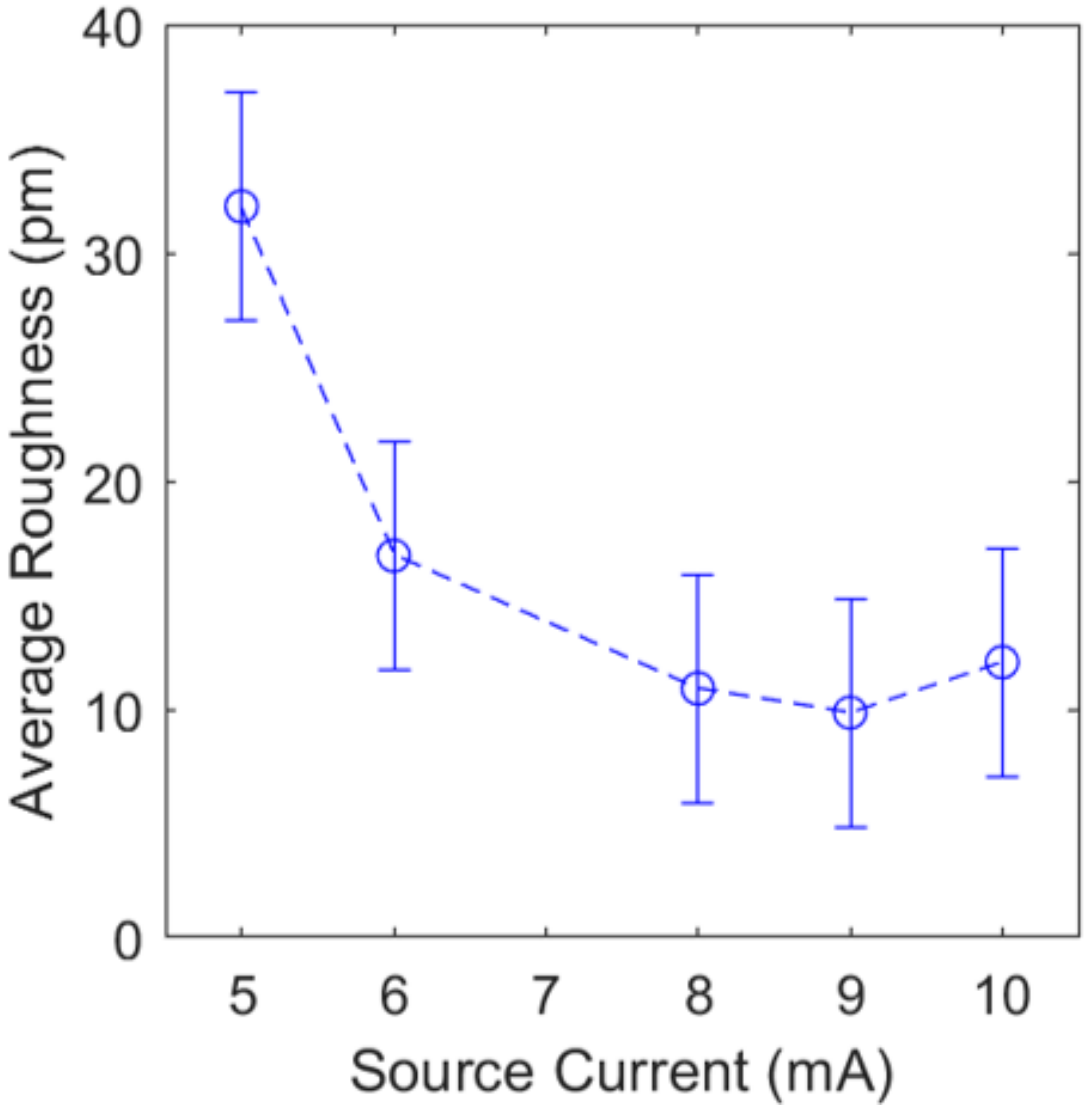

Figure 7.5: The average surface roughness extracted from the topography images of the same 50nm x 50nm area of various source currents at 100K.

To support this view, we also calculated the average autocorrelation length of the surface at variour source currents, of which the result is ploted in Fig. 7.6. It can be found that the autocorrelation decreases with source current decreasing. This agrees with picture of phase coexisting as a more inhomogeneous surface leads to shorter autocorrelation length.

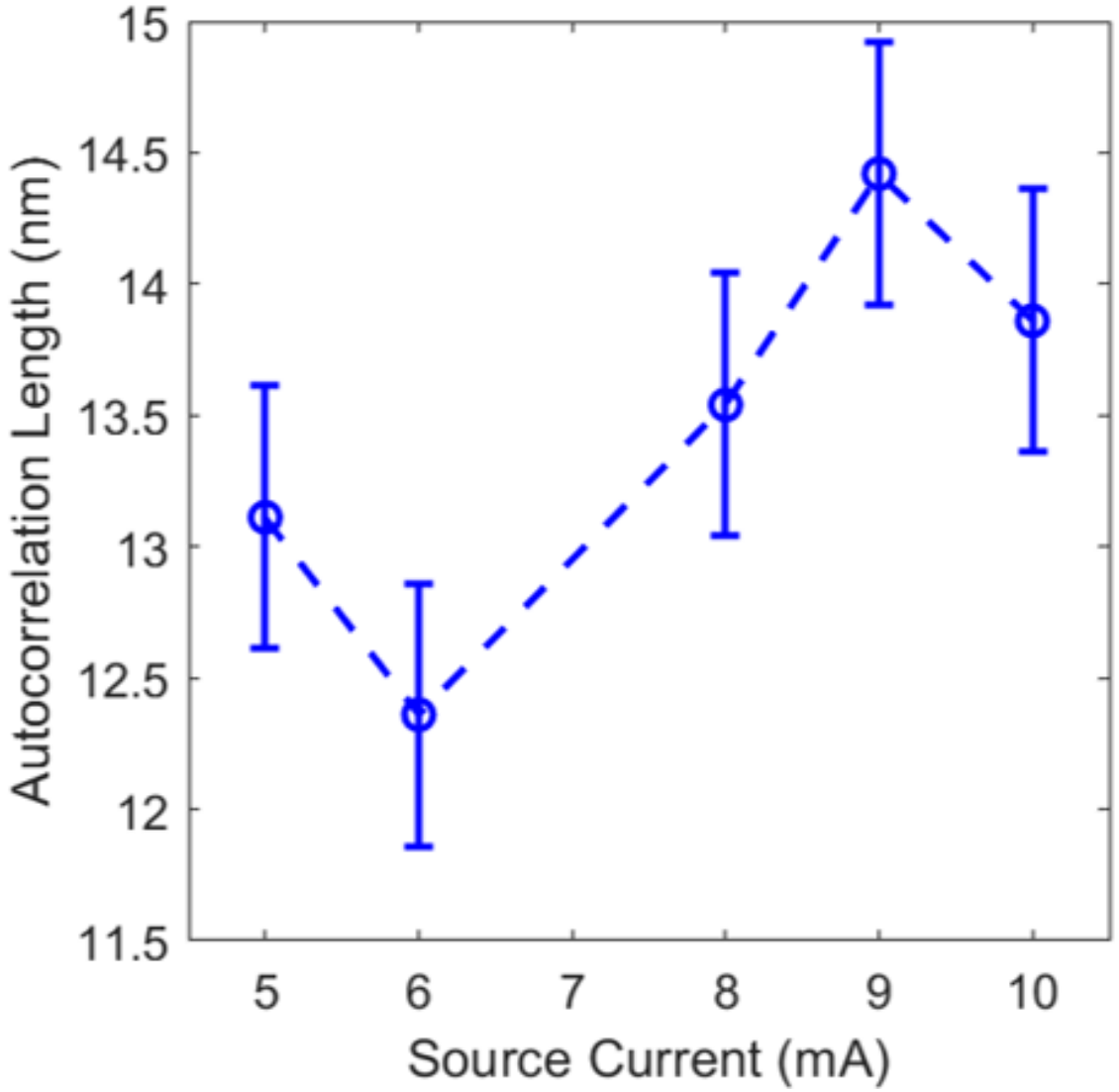

Figure 7.6: The average autocorrelation length extracted from the topography images of the same 50nm x 50nm area of various source currents at 100K.

Finally to provide a direct demontration of the surface inhomogeneity, we plot the 3D reconstruction of the surface at 5mA and 10mA in Fig. 7.7. Clearly the 10mA surface is much smoother than the 5mA one. These images show the nano-scale inhomogeneity on the surface of Ca_2RuO_4, which we believe is a key to understand the nature of this compound

and should be paid with great attention in future studies.

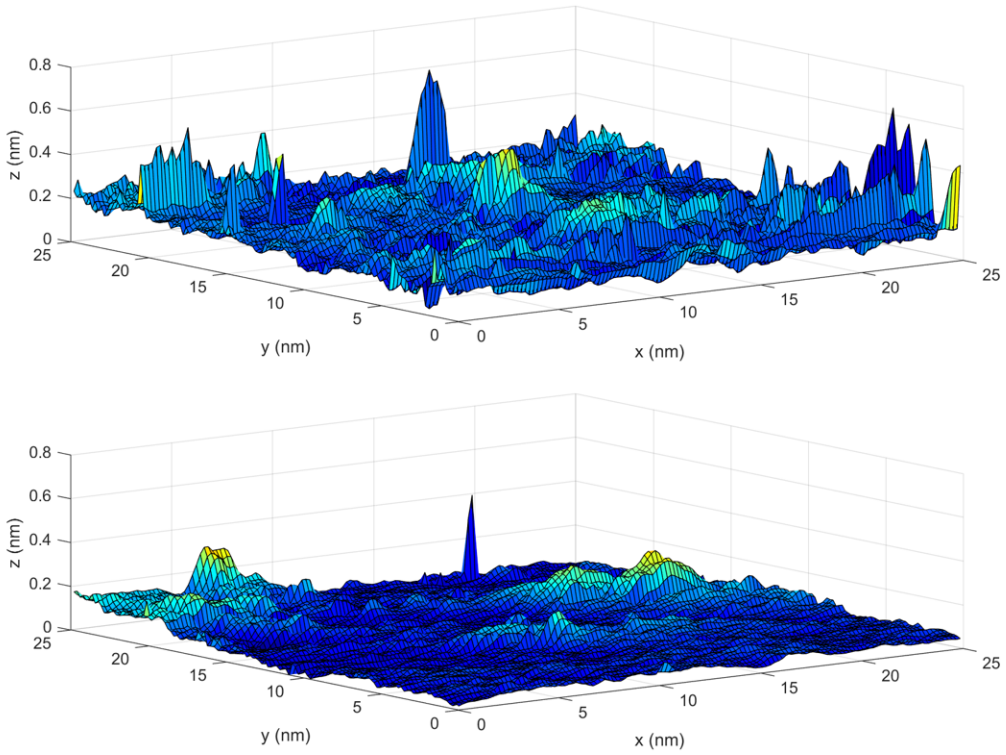

Figure 7.7: The 3D reconstruction of the topography at top: 5mA, bottom: 10mA.

Chapter 8

Conclusions

This thesis presented a first of its kind characterization via STM of the temperature-driven and current-driven MIT in Ca_2RuO_4. Topography images with atomic resolution were taken to show the lattice structure and verify the quality of the sample. STS were taken for both high-temperature metallilc state and high-current metallic state. The spectra for temperature-driven MIT show a gap of 50meV for insulating state and a phenomenon of states transfer during the transition. Compared with DMFT calculation, they also show the transition is highly related with the lattice structure. The spectra for current-driven MIT are very similar with temperature-driven ones. Further study on the spectra at 10mA and various temperatures shows a close relation between the evolution of the spectra and temperature. Combined with other studies, we believe the current-driven MIT is largely due to the Joule heating generate by the current. Finally, the surface roughness and auto-correlation length analysis supports the scenario that the intermediate insulating S* phase and the conducting L* phase coexist under current, forming a nano-sacle inhomogeneous surface.

The topography images of Ca_2RuO_4 show a series of steps created by the cleaving on the surface. When zoomed in, the atomically resolved images show the diamond lattice formed by the Calcium atoms and the stripe pattern along the b-axis due to the overlapping of Calcium atoms of 2 adjacent layers. These images prove the quality of both the crytals and the STM tips used in this study.

The STS measurement for the temperature-driven MIT shows a gap of roughly 50meV

for the insulating ground state. When temperature is above $T_c = 357K$, the gap is closed and a pseudo-gap emerges. Also the transition is accompanied by a phenomenon that some states being transferred from high-energy zone (around 1eV) to low-energy zone. Depsite of these spectra evolutions, all STS feature a significant asymmetry towards the valence band side (negative energy side). Compared with DMFT calculation, which is based on experimentally determined structure at 295K and 400K, most of the spectral features including the states transfer phenomenon are confirmed. However, DMFT predicts abundance of density of states near the Fermi surface with several signature peaks, which is not observed in our experiment. Nevertheless, these results emphasize the vital importance of lattice structure in the MIT of Ca_2RuO_4.

The STS measurement for the current-driven MIT shows great similarity with the result for the temperature-driven MIT. First of all, all spectra share the same general U-shape and asymmetry towards the valence band. A pseudo-gap can be found when a decent amount of current is applied, too. Furthermore, the similar state-transfer phenomenon is also present in the current-driven MIT. With source current increasing, more states are being pushed towards the Fermi surface. Such similarity indicates the high-current metallic state might be very similar with the high-temperature metallic state.

The STS at 10mA and various temperatures show a clear dependence on temperature, which rules out the possiblity that high-current metallic state is purely due to dopping. Combined with a wide variety of studies via transport, scattering technique and infrared thermal imaging, we can find the local temperature plays a dominating role in the MIT. It is very likely that the Joule heating generated by the current keeps the local region's temperature above the transition temperature hence turns it metallic. In this case, the surface should consist of the conducting L* phase and one insulating S* phase, of which the lattice parameters are slightly different. Through our surface roughness and autocorrelation length analysis, we find that the surface will become rougher and have shorter autocorrelation length when the crystal turns less conducting (i.e. closer to the insulating ground state in the phase diagram). This supports the hypothesis that the inhomogeneous surface comes from a nano-scale phase mixture. Therefore it is vital to characterize these local areas in future studies to reach a more comprehensive understanding on this non-equilibrium

phenomenon.

Part I

Bibliography

Bibliography

[1] Ruddlesden-popper phase. `https://en.wikipedia.org/wiki/Ruddlesden-Popper_phase#/media/File:Ruddlesden-popper_phase_1.png`. Accessed: 2019-12-10.

[2] Chanchal Sow, Shingo Yonezawa, Sota Kitamura, Takashi Oka, Kazuhiko Kuroki, Fumihiko Nakamura, and Yoshiteru Maeno. Current-induced strong diamagnetism in the mott insulator ca2ruo4. *Science*, 358(6366):1084–1087, 2017.

[3] Giordano Mattoni, Shingo Yonezawa, and Yoshiteru Maeno. Diamagnetic-like response from localised heating of a paramagnetic material. 2020.

[4] Qiang Han and Andrew Millis. Lattice energetics and correlation-driven metal-insulator transitions: The case of ca_2ruo_4. *Phys. Rev. Lett.*, 121:067601, Aug 2018.

[5] s,p,d,f orbitals. `https://socratic.org/chemistry/the-electron-configuration-of-atoms/arrangement-of-electrons-in-orbitals-spd-and-f`. Accessed: 2019-12-11.

[6] Drew Edelberg. Systems of transition metal dichalcogenides : Controlling applied strain and defect density with direct impact on material properties. 2019.

[7] Geroge Cao, C. Alexander, S. Mccall, J.E Crow, and R.P Guertin. From antiferromagnetic insulator to ferromagnetic metal: A brief review of the layered ruthenates. *Materials Science and Engineering: B*, 63:76–82, 08 1999.

[8] S. Nakatsuji and Y. Maeno. Switching of magnetic coupling by a structural symmetry change near the mott transition in $ca_{2-x}sr_xruo_4$. *Phys. Rev. B*, 62:6458–6466, Sep 2000.

[9] Hongxia Hao, Antoine Georges, Andrew J. Millis, Brenda Rubenstein, Qiang Han, and Hao Shi. Metal-insulator and magnetic phase diagram of ca_2ruo_4 from auxiliary field quantum monte carlo and dynamical mean field theory, 2019.

[10] J. Bertinshaw, N. Gurung, P. Jorba, H. Liu, M. Schmid, D. T. Mantadakis, M. Daghofer, M. Krautloher, A. Jain, G. H. Ryu, O. Fabelo, P. Hansmann, G. Khaliullin, C. Pfleiderer, B. Keimer, and B. J. Kim. Unique crystal structure of ca_2ruo_4 in the current stabilized semimetallic state. *Phys. Rev. Lett.*, 123:137204, Sep 2019.

[11] Jiawei Zhang, Alexander S. McLeod, Qiang Han, Xinzhong Chen, Hans A. Bechtel, Ziheng Yao, S. N. Gilbert Corder, Thomas Ciavatti, Tiger H. Tao, Meigan Aronson, G. L. Carr, Michael C. Martin, Chanchal Sow, Shingo Yonezawa, Fumihiko Nakamura, Ichiro Terasaki, D. N. Basov, Andrew J. Millis, Yoshiteru Maeno, and Mengkun Liu. Nano-resolved current-induced insulator-metal transition in the mott insulator ca_2ruo_4. *Phys. Rev. X*, 9:011032, Feb 2019.

[12] C. S. Snow, S. L. Cooper, G. Cao, J. E. Crow, H. Fukazawa, S. Nakatsuji, and Y. Maeno. Pressure-tuned collapse of the mott-like state in $ca_{n+1}ru_no_{3n+1}$ $(n = 1, 2)$: Raman spectroscopic studies. *Phys. Rev. Lett.*, 89:226401, Nov 2002.

[13] Gabriel Kotliar and Dieter Vollhardt. Strongly correlated materials: Insights from dynamical mean-field theory. *Physics Today*, 57(3):53–59, 2004.

[14] Masatoshi Imada, Atsushi Fujimori, and Yoshinori Tokura. Metal-insulator transitions. *Rev. Mod. Phys.*, 70:1039–1263, Oct 1998.

[15] Introduction to dmft. `https://www.theorie.physik.uni-muenchen.de/activities/schools/archiv/asc_school_17/extramaterial/parcollet_slides_1.pdf`. Accessed: 2019-12-10.

[16] C. Cirillo, V. Granata, G. Avallone, R. Fittipaldi, C. Attanasio, A. Avella, and A. Vecchione. Emergence of a metallic metastable phase induced by electrical current in ca_2ruo_4. *Phys. Rev. B*, 100:235142, Dec 2019.

[17] Bednorz J.G. and Müller K.A. Possible hightc superconductivity in the ba-la-cu-o system. *Z. Physik B - Condensed Matter*, 64:189–193, 1986.

[18] D. A. Wollman, D. J. Van Harlingen, W. C. Lee, D. M. Ginsberg, and A. J. Leggett. Experimental determination of the superconducting pairing state in ybco from the phase coherence of ybco-pb dc squids. *Phys. Rev. Lett.*, 71:2134–2137, Sep 1993.

[19] Manfred Sigrist and T. M. Rice. Unusual paramagnetic phenomena in granular high-temperature superconductors—a consequence of *d*- wave pairing? *Rev. Mod. Phys.*, 67:503–513, Apr 1995.

[20] C. C. Tsuei and J. R. Kirtley. Pairing symmetry in cuprate superconductors. *Rev. Mod. Phys.*, 72:969–1016, Oct 2000.

[21] H. Alloul, T. Ohno, and P. Mendels. ^{89}Y nmr evidence for a fermi-liquid behavior in $yba_2cu_3o_{6+x}$. *Phys. Rev. Lett.*, 63:1700–1703, Oct 1989.

[22] Konstantin N. Kudin, Gustavo E. Scuseria, and Richard L. Martin. Hybrid density-functional theory and the insulating gap of uo_2. *Phys. Rev. Lett.*, 89:266402, Dec 2002.

[23] Y. Maeno, H. Hashimoto, K. Yoshida, S. Nishizaki, T. Fujita, J. G. Bednorz, and F. Lichtenberg. Superconductivity in a layered perovskite without copper. *Nature*, 372(6506):532–534, 1994.

[24] M. Sigrist, D. Agterberg, T.M. Rice, and M.E. Zhitomirsky. Sr2ruo4 - a realization of spin triplet pairing? *Physica C: Superconductivity*, 282-287:214 – 217, 1997. Materials and Mechanisms of Superconductivity High Temperature Superconductors V.

[25] A. P. Mackenzie, R. K. W. Haselwimmer, A. W. Tyler, G. G. Lonzarich, Y. Mori, S. Nishizaki, and Y. Maeno. Extremely strong dependence of superconductivity on disorder in sr_2ruo_4. *Phys. Rev. Lett.*, 80:161–164, Jan 1998.

[26] X. N. Lin, Z. X. Zhou, V. Durairaj, P. Schlottmann, and G. Cao. Colossal magnetoresistance by avoiding a ferromagnetic state in the mott system $ca_3ru_2o_7$. *Phys. Rev. Lett.*, 95:017203, Jun 2005.

[27] G. Cao, L. Balicas, Y. Xin, J. E. Crow, and C. S. Nelson. Quantum oscillations, colossal magnetoresistance, and the magnetoelastic interaction in bilayered $ca_3ru_2o_7$. *Phys. Rev. B*, 67:184405, May 2003.

[28] R Zimmermann, P Steiner, R Claessen, F Reinert, S Hüfner, P Blaha, and P Dufek. Electronic structure of 3d-transition-metal oxides: on-site coulomb repulsion versus covalency. *Journal of Physics: Condensed Matter*, 11(7):1657–1682, jan 1999.

[29] Y. S. Lee, J. S. Lee, T. W. Noh, Douck Young Byun, Kwang Soo Yoo, K. Yamaura, and E. Takayama-Muromachi. Systematic trends in the electronic structure parameters of the 4*d* transition-metal oxides Sr*m*o_3(*m* = Zr, mo, ru, and rh). *Phys. Rev. B*, 67:113101, Mar 2003.

[30] G. Cao, L. Balicas, Y. Xin, E. Dagotto, J. E. Crow, C. S. Nelson, and J. P. Hill. Complex quantum phenomena in a bilayered calcium ruthenate, 2002.

[31] Fumihiko Nakamura, Mariko Sakaki, Yuya Yamanaka, Sho Tamaru, Takashi Suzuki, and Yoshiteru Maeno. Electric-field-induced metal maintained by current of the mott insulator ca2ruo4. *Scientific Reports*, 3(1):2536, 2013.

[32] S. N. Ruddlesden and P. Popper. The compound $Sr_3Ti_2O_7$ and its structure. *Acta Crystallographica*, 11(1):54–55, Jan 1958.

[33] C. S. Alexander, G. Cao, V. Dobrosavljevic, S. McCall, J. E. Crow, E. Lochner, and R. P. Guertin. Destruction of the mott insulating ground state of ca_2ruo_4 by a structural transition. *Phys. Rev. B*, 60:R8422–R8425, Sep 1999.

[34] M. Braden, G. André, S. Nakatsuji, and Y. Maeno. Crystal and magnetic structure of ca_2ruo_4 : magnetoelastic coupling and the metal-insulator transition. *Phys. Rev. B*, 58:847–861, Jul 1998.

[35] O. Friedt, M. Braden, G. André, P. Adelmann, S. Nakatsuji, and Y. Maeno. Structural and magnetic aspects of the metal-insulator transition in $ca_{2-x}sr_xruo_4$. *Phys. Rev. B*, 63:174432, Apr 2001.

[36] G. BINNIG and H. ROHRER. Scanning tunneling microscopy. *Journal of Instrumentation*, 12(03):P03011, 2017.

[37] C. Julian Chen. Introduction to scanning tunneling microscopy. page 25, 1997.

[38] Cryo positioning stage – high resonance (cpshr). Accessed: 2019-12-29.

[39] J. P. Ibe, P. P. Bey, S. L. Brandow, R. A. Brizzolara, N. A. Burnham, D. P. DiLella, K. P. Lee, C. R. K. Marrian, and R. J. Colton. On the electrochemical etching of tips for scanning tunneling microscopy. *Journal of Vacuum Science & Technology A*, 8(4):3570–3575, 1990.

[40] Stm tip making. Accessed: 2019-12-29.

[41] Using wire cutter to make stm tips. Accessed: 2019-12-29.

[42] Stefan Ernst. Optimisation of the preparation processfor tips used in scanning tunneling microscopy. 2006.

[43] R. A. Millikan and C. C. Lauritsen. Relations of field-currents to thermionic-currents. *Proceedings of the National Academy of Sciences*, 14(1):45–49, 1928.

[44] Michael J. Heben, Moris M. Dovek, Nathan S. Lewis, Reginald M. Penner, and Calvin F. Quate. Preparation of stm tips for in-situ characterization of electrode surfaces. *Journal of Microscopy*, 152(3):651–661, 1988.

[45] W. Chen, V. Madhavan, T. Jamneala, and M. F. Crommie. Scanning tunneling microscopy observation of an electronic superlattice at the surface of clean gold. *Phys. Rev. Lett.*, 80:1469–1472, Feb 1998.

[46] S. Nakatsuji and Y. Maeno. Quasi-two-dimensional mott transition system $ca_{2-x}sr_xruo_4$. *Phys. Rev. Lett.*, 84:2666–2669, Mar 2000.

[47] Z. Fang and K. Terakura. Magnetic phase diagram of $ca_{2-x}sr_xruo_4$ governed by structural distortions. *Phys. Rev. B*, 64:020509, Jun 2001.

[48] Fumihiko Nakamura. Pressure-induced mott transition and related novel quantum phenomena in ca2ruo4. *Journal of the Physical Society of Japan*, 76(Suppl.A):96–99, 2007.

[49] M. Braden, G. André, S. Nakatsuji, and Y. Maeno. Crystal and magnetic structure of ca_2ruo_4 : magnetoelastic coupling and the metal-insulator transition. *Phys. Rev. B*, 58:847–861, Jul 1998.

[50] O. Friedt, M. Braden, G. André, P. Adelmann, S. Nakatsuji, and Y. Maeno. Structural and magnetic aspects of the metal-insulator transition in $ca_{2-x}sr_xruo_4$. *Phys. Rev. B*, 63:174432, Apr 2001.

[51] Jiawei Zhang, Alexander S. McLeod, Qiang Han, Xinzhong Chen, Hans A. Bechtel, Ziheng Yao, S. N. Gilbert Corder, Thomas Ciavatti, Tiger H. Tao, Meigan Aronson, G. L. Carr, Michael C. Martin, Chanchal Sow, Shingo Yonezawa, Fumihiko Nakamura, Ichiro Terasaki, D. N. Basov, Andrew J. Millis, Yoshiteru Maeno, and Mengkun Liu. Supplemental material : Nano-resolved current-induced insulator-metal transition in the mott insulator ca_2ruo_4. *Phys. Rev. X*, 9:011032, Feb 2019.

[52] Hengdi Zhao, Bing Hu, Feng Ye, Christina Hoffmann, Itamar Kimchi, and Gang Cao. Nonequilibrium orbital transitions via applied electrical current in calcium ruthenate. 2019.

[53] J. S. WOOD. Ligand field theory. *Nature*, 226(5250):1067–1068, 1970.

[54] Mario Cuoco, Filomena Forte, and Canio Noce. Probing spin-orbital-lattice correlations in $4d^4$ systems. *Phys. Rev. B*, 73:094428, Mar 2006.

[55] S. Fratini, D. Feinberg, and M. Grilli. Jahn-teller, charge and magnetic ordering in half-doped manganese oxides. *The European Physical Journal B: Condensed Matter and Complex Systems*, 22(2):157–165, 2001.

[56] Takashi Hotta and Elbio Dagotto. Orbital ordering in manganites and ruthenates. *Physica B-condensed Matter - PHYSICA B*, 312:700–702, 03 2002.

[57] Takashi Hotta, Andre Luiz Malvezzi, and Elbio Dagotto. Charge-orbital ordering and phase separation in the two-orbital model for manganites: Roles of jahn-teller phononic and coulombic interactions. *Phys. Rev. B*, 62:9432–9452, Oct 2000.

[58] Louis Felix Feiner and Andrzej M. Oleś. Electronic origin of magnetic and orbital ordering in insulating $lamno_3$. *Phys. Rev. B*, 59:3295–3298, Feb 1999.

[59] Takashi Hotta and Elbio Dagotto. Prediction of orbital ordering in single-layered ruthenates. *Phys. Rev. Lett.*, 88:017201, Dec 2001.

[60] R. O. Jones and O. Gunnarsson. The density functional formalism, its applications and prospects. *Rev. Mod. Phys.*, 61:689–746, Jul 1989.

[61] Born-oppenheimer approach: Diabatization and topological matrix. pages 26–57, 2006.

[62] J. Hubbard and Brian Hilton Flowers. Electron correlations in narrow energy bands. *Proceedings of the Royal Society of London. Series A. Mathematical and Physical Sciences*, 276(1365):238–257, 1963.

[63] J H de Boer and E J W Verwey. Semi-conductors with partially and with completely filled3d-lattice bands. *Proceedings of the Physical Society*, 49(4S):59–71, aug 1937.

[64] N F Mott and R Peierls. Discussion of the paper by de boer and verwey. *Proceedings of the Physical Society*, 49(4S):72–73, aug 1937.

[65] S. Acheche, A. Reymbaut, M. Charlebois, D. Sénéchal, and A.-M. S. Tremblay. Mott transition and magnetism on the anisotropic triangular lattice. *Phys. Rev. B*, 94:245133, Dec 2016.

[66] Albert J W Reitsma, Louis Felix Feiner, and Andrzej M Oleś. Orbital and spin physics in LiNiO2and NaNiO2. *New Journal of Physics*, 7:121–121, may 2005.

[67] E. Ohmichi, Y. Yoshida, S. I. Ikeda, N. Shirakawa, and T. Osada. Colossal magnetoresistance accompanying a structural transition in a highly two-dimensional metallic state of $ca_3ru_2o_7$. *Phys. Rev. B*, 70:104414, Sep 2004.

[68] G. Cao, L. Balicas, X. N. Lin, S. Chikara, E. Elhami, V. Duairaj, J. W. Brill, R. C. Rai, and J. E. Crow. Destruction of an orbitally ordered and spin-polarized state: Colossal magnetoresistance in ca3ru2o7. *Journal of Electronic Materials*, 33(11):1303–1307, 2004.

[69] Emil J Rozbicki, James F Annett, Jean-René Souquet, and Andrew P Mackenzie. Spin–orbit coupling andk-dependent zeeman splitting in strontium ruthenate. *Journal of Physics: Condensed Matter*, 23(9):094201, feb 2011.

[70] Alexander Ruh and Valerij G. Kiselev. Calculation of larmor precession frequency in magnetically heterogeneous media. *Concepts in Magnetic Resonance Part A*, 47A(1):e21472, 2018.

[71] J. E. Hirsch. Spin hall effect. *Phys. Rev. Lett.*, 83:1834–1837, Aug 1999.

[72] C. S. Nelson, H. Mo, B. Bohnenbuck, J. Strempfer, N. Kikugawa, S. I. Ikeda, and Y. Yoshida. Spin-charge-lattice coupling near the metal-insulator transition in $ca_3ru_2o_7$. *Phys. Rev. B*, 75:212403, Jun 2007.

[73] T. Böske, K. Maiti, O. Knauff, K. Ruck, M. S. Golden, G. Krabbes, J. Fink, T. Osafune, N. Motoyama, H. Eisaki, and S. Uchida. Cu-o network-dependent core-hole screening in low-dimensional cuprate systems: A high-resolution x-ray photoemission study. *Phys. Rev. B*, 57:138–141, Jan 1998.

[74] J. Zaanen, G. A. Sawatzky, and J. W. Allen. Band gaps and electronic structure of transition-metal compounds. *Phys. Rev. Lett.*, 55:418–421, Jul 1985.

[75] T. Matsumoto and T. Kawai. In-gap density of states in hole- and electron-doped cuo2 planes probed by scanning tunneling spectroscopy. *Applied Physics A*, 68(6):687–690, 1999.

[76] P. Hohenberg and W. Kohn. Inhomogeneous electron gas. *Phys. Rev.*, 136:B864–B871, Nov 1964.

[77] Axel D. Becke. Perspective: Fifty years of density-functional theory in chemical physics. *The Journal of Chemical Physics*, 140(18):18A301, 2014.

[78] Walter Metzner and Dieter Vollhardt. Correlated lattice fermions in $d = \infty$ dimensions. *Phys. Rev. Lett.*, 62:324–327, Jan 1989.

[79] Antoine Georges and Gabriel Kotliar. Hubbard model in infinite dimensions. *Phys. Rev. B*, 45:6479–6483, Mar 1992.

[80] M. Jarrell. Hubbard model in infinite dimensions: A quantum monte carlo study. *Phys. Rev. Lett.*, 69:168–171, Jul 1992.

[81] Kenneth G. Wilson. The renormalization group: Critical phenomena and the kondo problem. *Rev. Mod. Phys.*, 47:773–840, Oct 1975.

[82] J. E. Hirsch and R. M. Fye. Monte carlo method for magnetic impurities in metals. *Phys. Rev. Lett.*, 56:2521–2524, Jun 1986.

[83] D. Vollhardt. Dynamical mean-field theory for correlated electrons. *Annalen der Physik*, 524(1):1–19, 2012.

[84] Antoine Georges. Strongly correlated electron materials: Dynamical mean-field theory and electronic structure. *AIP Conference Proceedings*, 715(1):3–74, 2004.

[85] Pid. Accessed: 2019-12-20.

[86] Giordano Mattoni, Shingo Yonezawa, Fumihiko Nakamura, and Yoshiteru Maeno. Role of local temperature in the current-driven metal-insulator transition of ca2ruo4, 2020.

Part II

Appendices

Appendix A

Gold (111) Surface Preparation

As mentioned in Chapter 2, a good Au (111) surface is vitally important for the success for STM experiments. Here we present our systematic way for gold preparation.

A.1 Mounting Gold on Sample Holder

Our gold cystal, which is a 1.0cm diameter, 1mm thick round single crystal, is purchased from Accumet Material. The surface has already been cleaved and polished with care by the vendor. Due to the fact that gold will make alloy with iron at high temperature, the gold crystal cannot be mounted as an ordinary sample. In our experiment, to protect the clean surface of gold, a special gold sample holder is designed, as shown Fig. A.1 (c). The central round slot is designed to hold the gold cyrstal with its surface being higher than the rest of the sample holder. Four molybdenum screws are pushing down 4 ceramic washers, securing the gold crystal. With this design, the gold surface will not be contaminated by the sample holder and the whole sample will not get damaged by the high temperature in the annealing process, as shown in Fig A.1 (b).

A.2 Gold Preparation Procedure

After installing the gold on the gold sample holder, the whole sample is placed at the load-lock of the system to be prepared. The load-lock is a relatively small chamber with many

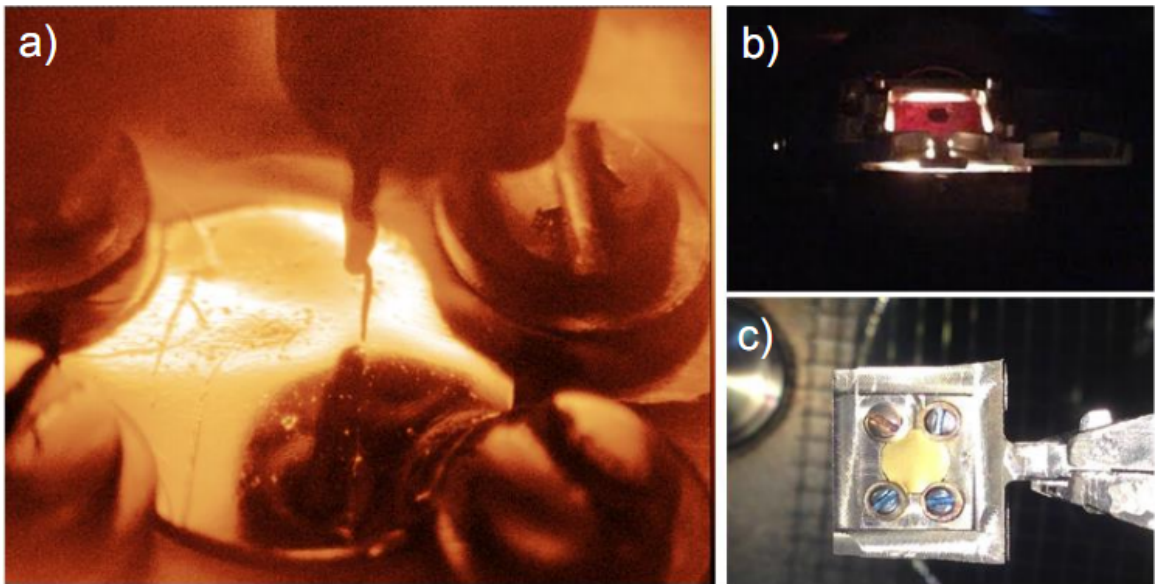

Figure A.1: (a) tip approaching the prepared gold surface (b) the gold in preparation process (c) the gold sample in the UHV chamber [6]

ports connected with different instruments, including the ion sputter gun, the residual gas analyzer (RGA), the tubo and rough pump, and the transfer arm with the annealer installed at its end. Before the gold preparation sequence starts, the load-lock is pumped to a high vaccum with base pressure below 1×10^{-7} Torr. This is to make sure no residual gas will influence the quality of the ion beam later used in the sputtering process. When the base pressure is reached, the annealer is turned on with the power around 10W for a couple of hours. This is to degas the system as they will out gas a lot when heating to a high temperature. After degasing, ultra-purified airgon is vented to the load-lock through a leak valve on the ion sputter gun. With proper adjustment on that valve, an airgon pressure of $4.2 - 4.6 \times 10^{-6}$ Torr is reached, which is the pressure the sputter gun requires. Then the annealer is turned on with a total power of 80-90W, bring up the temperature of the gold crystal to around 700°C. The annealer is kept on for the rest of the preparation process. And the ion sputter gun enters a on-off cycle, with being on for 20 minutes and off for the next 20 minutes. This cycle is run for a total 48 hours, during which the gold surface is cleaned by sputtered ion and then reconstructs under annealing. After all these cycles, the

leak valve is shut and the pressure inside the load-lock will repidly decrease to $\tilde{\times}10^{-8}$ Torr. At this condition a final annealing for 30 minutes is conducted. Then the annealer is also shut down and the gold is left in the load-lock to cool down. Roughly in one hour the gold sample is cooled to room temperature and ready to be used.

Appendix B

Matlab Codes to Control Devices

As mentioned in Chapter 4, the source current/voltage is controlled/read automatically through Matlab programs. Here is a summary of the source code that might be helpful for similar researches.

The Keithley 2400 sourcemeter and the YOKOGAWA GS 200 are used in our experiment. They are connected to the lab PC through GPIB and USB connectors via the VISA protocol. In Matlab there is a package called “tmtools” that is able to write/query information to all equipment connected to the PC. In order to control and read information from these equipment, several Matlab scripts were written as the following.

1. To control current through YOKOGAWA

```
function [ OUT ] = CurrentSET(END,TIME,varargin)
%UNTITLED2 Summary of this function goes here
%   Detailed explanation goes here
%YOKOGAWA Code for communicating with an instrument.

% Find a VISA-USB object.
obj1 = instrfind('Type', 'visa-usb', 'RsrcName', 'USB0::0x0B21::0x0039::91L843952::0::INSTR', 'Tag', '');
% connect to the device, details need to be changed based on each device

% Create the VISA-USB object if it does not exist
% otherwise use the object that was found.
if isempty(obj1)
   obj1 = visa('TEK', 'USB0::0x0B21::0x0039::91L843952::0::INSTR');
else
   fclose(obj1);
   obj1 = obj1(1);
end

% Connect to instrument object, obj1.
fopen(obj1);
set(obj1, 'Timeout', 1.0);
```

```
% Communicating with instrument object, obj1.
fprintf(obj1, ':SOUR:FUNC CURR');
if(length(varargin)>= 1)
   OFF = 1;
   fprintf(obj1, ':OUTP 0');
   VAL = 'OUTP OFF'
   return
end



fprintf(obj1, ':OUTP 1');
LEV = query(obj1, ':SOUR:LEV?'); % set to source current
[m , n] = size(LEV);
val = 0;
power = 0;
for idx = 3:n
   if LEV(idx) == 'E'
      val = str2double(LEV(1:idx-1));
      power = str2double(LEV(idx+1:n));
      break
   end
end
VAL = val*(10^power);

%VAL = str2double(LEV(1:6))*10^(str2double(LEV(8:10)));
for (i = VAL:sign(END-VAL)*(1E-6):END)
   SEND = strcat([':SOUR:LEV ',num2str(i)]);
   fprintf(obj1, SEND);
   pause(TIME);
```

```
end
%fprintf(obj1, ':SOUR:LEV .000002');

% Disconnect all objects.
fclose(obj1);

% Clean up all objects.
delete(obj1);
end
```

2. Read voltage from Keithley

```
function out = GetVoltageKeithley()
% Find a VISA-GPIB object.
obj1 = instrfind('Type', 'visa-gpib', 'RsrcName', 'GPIB0::24::0::INSTR', 'Tag', '');
if isempty(obj1)
   obj1 = visa('TEK', 'GPIB0::24::0::INSTR');
else
   fclose(obj1);
   obj1 = obj1(1);
end
% Connect to instrument object, obj1.
fopen(obj1);
set(obj1, 'Timeout', 1.0);
fprintf(obj1, ':OUTP 1');

I = query(obj1, ':FORM:ELEM VOLT');
[m , n] = size(I);
   val = 0;
   power = 0;
   for idx = 1:n
      if I(idx) == 'E'
         val = str2double(I(1:idx-1));
         power = str2double(I(idx+1:n));
         break
      end
   end
   out = val*(10^power);
end
```

3. Transport Measurement via Keitheley

```
function  OUT   = IV_safe_Keithley( START, END, f_name , varargin)
if(length(varargin)>= 1)
   step = varargin{1};
else
   if END >= START
      step = 0.001;
   else
      step = -0.001;
   end
end

curr = START;
transport = [];

while curr ~= END
   prev = curr;
   curr = curr + step;
   if END >= START
      curr = min(curr ,END);
   else
      curr = max(curr , END);
   end
   transport = [transport; IV_Keithley(prev , curr - 0.000001 , f_name)];
   save(f_name , 'transport');
end

OUT = transport;
End
```

Other codes were also used to realize some minor functions. Due to space limitations they are not included in this thesis